8-9-2022

Flow and thermal transport in additively manufactured metal lattices based on novel unit-cell topologies

Inderjot Kaur

Mississippi Sate University, ik154@msstate.edu

Recommended Citation

Kaur, Inderjot, "Flow and thermal transport in additively manufactured metal lattices based on novel unit-cell topologies" (2022). *Theses and Dissertations*. 5587.
https://scholarsjunction.msstate.edu/td/5587

Flow and thermal transport in additively manufactured metal lattices based on novel unit-cell topologies

By

Inderjot Kaur

Approved by:

Prashant Singh (Major Professor)
HeeJin Cho
Shanti Bhushan
Hongjoo Rhee
Tonya Stone (Graduate Coordinator)
Jason M. Keith (Dean, Bagley College of Engineering)

A Dissertation
Submitted to the Faculty of
Mississippi State University
in Partial Fulfillment of the Requirements
for the Degree of Doctor of Philosophy
in Mechanical Engineering
in the Bagley College of Engineering.

Mississippi State, Mississippi

August 2022

Name: Inderjot Kaur

Date of Degree: August 9, 2022

Institution: Mississippi State University

Major Field: Mechanical Engineering

Major Professor: Prashant Singh

Title of Study: Flow and thermal transport in additively manufactured metal lattices based on novel unit-cell topologies

Pages in Study: 194

Candidate for Degree of Doctor of Philosophy

The emergence of metal Additive Manufacturing *(AM)* over the last two decades has opened venues to mitigate the challenges associated with stochastic open-cell metal foams manufactured through the traditional *foaming* process. Regular lattices with user-defined unit cell topologies have been reported to exhibit better mechanical properties in comparison to metal foams which extend their applicability to multifunctional heat exchangers subjected to both thermal and mechanical loads. The current study aims at investigating the thermal-hydraulic characteristics of promising novel unit cell topologies realizable through *AM* technologies.

Experimental investigation was conducted on four different topologies, viz (a) Octet, (b) Face-diagonal (FD) cube, (c) Tetrakaidecahedron, and (d) Cube, printed in single-cell thick sandwich type configuration in 420 stainless steel via *Binder Jetting* technology at same intended porosity. The effective thermal conductivity of the samples was found to be strongly dependent on the lattice porosity, however, no significant dependence on the unit-cell topology was demonstrated. Face-diagonal cube lattice exhibited the highest heat transfer coefficient and pressure drop, and consequently provided the lowest thermal-hydraulic performance.

A procedure to incorporate the manufacturing-induced random roughness effects in the samples during numerical modelling is introduced. The numerical simulations were conducted on samples exhibiting the roughness profiles having statistically same mean roughness as the additively manufactured coupons and the results were compared to that obtained from the intended smooth-profiled CAD models that were fed into the printing machines. The analysis showed that inclusion of roughness effects in computational models can significantly improve the thermal performance predictions.

Through this study, we demonstrate that additively manufactured ordered lattices exhibit superior thermal transport characteristics and future developmental efforts would require extensive experimentations to characterize their thermal and flow performance as well as local surface quality and AM-induced defect recognition. Experimental findings would also need to be supported by computational efforts where configurations which closely mimic the real AM parts could be modeled. A combined experimental-numerical framework is recommended for advancements in metal additive manufacturing-enabled enhanced heat transfer concepts.

DEDICATION

I dedicate this work to my parents.

ACKNOWLEDGEMENTS

I would like to express sincere gratitude to my advisor Dr. Prashant Singh for his guidance and support throughout my Ph.D. journey. His dedication, professional ethics, discipline, and constant pursuit of achieving academic excellence will remain an inspiration for the rest of my life. I am also thankful to my committee members - Dr. HeeJin Cho, Dr. Shanti Bhushan, and Dr. Hongjoo Rhee, for their encouragement and insightful discussions during my research period.

I would like to thank Mechanical Engineering department head Dr. Haitham El Kadiri and graduate coordinator Dr. Tonya Stone for their frequent support. Many thanks to the department staff, especially Ms. Delia Nuckolls and Ms. Meredith Betts, who have patiently answered all my queries regarding requirements to fulfill a degree. I also acknowledge the fruitful time that I spent with my lab-mates, Youssef Aider and Junaid Khan.

Last but not the least, a heartfelt thanks to my parents and brother who have been an unwavering support throughout all the endeavors of my life.

TABLE OF CONTENTS

CHAPTER

LIST OF TABLES

LIST OF FIGURES

CHAPTER I

INTRODUCTION

Fiber-based regular lattices have recently emerged as an attractive thermal management concept in several engineering applications such as electronics packaging and high-pressure stage gas turbine blades. The progress in metal additive manufacturing (AM) technology has made it possible to realize the lattices made from user-defined unit-cell topologies. These architectured unit cells can be reticulated in three-dimensional space to obtain thick lattice blocks, however, a single-cell thick sandwich type configuration has gained significant traction recently due to its improved utilization of the metal volume in thermal exchange under stringent mass and volume control environment. Most of the existing studies dedicated to analyzing flow and thermal exchange in regular lattices are numerical investigations conducted on smooth CAD models. This study uniquely addresses the two key research gaps pertaining to heat transfer analysis of the regular lattices: (1) reporting the experimental data obtained from tests conducted on additively manufactured coupons of unique unit-cell topologies that have been known to exhibit excellent mechanical properties in the past. The prior numerical investigation on the selected topologies also validate their candidacy for the experimental heat transfer investigations, and (2) incorporating the effects of surface roughness profiles realized during manufacturing process in computational models.

Chapter 2 herein provides a very comprehensive review of the prior investigations conducted on additively manufactured lattices and the research-gap with respect to viability of regular lattices as heat exchange augmentation concept is thoroughly discussed. Chapter 3 and 4 discusses the results from numerical investigations conducted on smooth unit cell topologies as proof of concept to analyze and rank their thermal-hydraulic behavior. Experimental investigation conducted on additively manufactured lattices to obtain the relative thermal and pressure drop trends is discussed in Chapter 5. The CT-scan images of the two selected topologies are presented along with the discussion on the observed defects and surface roughness profiles. Finally, a methodology to incorporate these anomalies in computational models is discussed in Chapter 6.

CHAPTER II

CRITICAL EVALUATION OF ADDITIVELY MANUFACTURED METAL LATTICES FOR VIABILITY IN ADVANCED HEAT EXCHANGERS[1]

Abstract

The advantages offered by the stochastic metal foams when used in high-performance compact heat exchangers is evident in the open literature. Recently, there has been a surge in investigations on regular metal lattices which can be manufactured additively, because of their "potential" to provide multifunctional and tunable characteristics to heat exchangers. These lattices are also reported to lend superior mechanical properties as well. The literature, however, lacks in the critical assessment of these additively manufactured regular lattices in terms of the quality of printed parts (defects, surface roughness, etc.), their compatibility in compact heat exchangers, flow and thermal transport characteristics, and whether or not they are viable alternatives to the commercial metal foams conventionally manufactured. This paper reports different manufacturing routes for the fabrication of conventional stochastic and regular lattices and additively manufactured regular lattices, and how these technologies have evolved over the years. The additively manufactured lattices different from the commercial TKD may result in significantly higher interstitial heat transfer coefficient. Further, the design freedom allows different porosities

---

[1] Kaur, I. and Singh, P., 2021. Critical evaluation of additively manufactured metal lattices for viability in advanced heat exchangers. International Journal of Heat and Mass Transfer, 168, p.120858. doi: 10.1016/j.ijheatmasstransfer.2020.120858

through which higher effective thermal conductivity can be achieved. The usage of regular lattices in tube-heat exchangers, as wicks in heat pipes, heat transfer enhancement features in boiling heat transfer and transpiration cooling mechanisms of turbine blades as an alternative to conventional technologies is promising. The role of inherent surface roughness in dictating the thermal and flow transport in additively manufactured lattices, especially for multi-phase flow applications, should be studied in more detail.

2.1 Introduction

Porous materials feature solid matrix containing isolated or interconnected void spaces, usually referred to as *pores* which can be saturated with air, liquid, or phase change materials (in solid or liquid state). Liu and Chen [1] stated "not everything that contains pores can be considered as *porous material*". The occurrence of unwanted cavities in any manufactured product are *defects* which tend to deteriorate the expected performance of the material, on the other hand, the embedded pores in the architecture of the 'porous materials', are expected to enhance the overall structural and desired functional properties of the material. Due to their multifunctional nature, porous media applications can be found in chemical, civil, mechanical, food and nuclear industries, etc., e.g. in catalytic reactors, porous radiant burners, absorption and filtration devices, [2–5], electronic cooling [6–12], solar reactors [13–15], nuclear reactors [16][17], thermal regulation of buildings [18,19], heat exchangers [20–22], thermal storage systems involving phase change materials (PCM) [23,24], acoustic damping applications [25], food science and technology [26–28].

Most of the porous media studies between 1960-1980 were performed in the areas of geothermal, geophysical and petroleum extraction methods [29–34]. The movement of water/nutrients into or out of soil, extraction of oil via. oil-displacement method by injecting water or foams into deep oil reservoirs, evaluation of rate at which energy could be extracted from the earth, were some of the practical problems which were mathematically modelled by considering sand, gravel, rock, and marble grains as porous medium. The flow circulation and wave attenuation in vegetated zones such as wetlands has been investigated through porous media models [35,36]. Cooling of a stack of parallel plates in free-stream and finned tube bundles in condenser has also been approached through porous media modelling [37,38]. For these examples, the solid matrix through which the transport occurs is not necessarily considered a material, at least not an artificial (manmade) porous structure, but the modeling of physical domain as "porous" has been proven to yield satisfactory results.

Post 1980, investigations by Whitaker et al. [39–42], Bejan et al. [43][44], Kaviany [45] and Vafai et al. [46–50] improved the understanding of the flow physics and thermal transport through porous media. During this period, more sophisticated models of flow and thermal transport including the effects of non-Darcian flow, thermal dispersion, local thermal equilibrium (LTE) and local-thermal non-equilibrium (LTNE), variable-porosity were successfully developed. While most of the previous studies aimed at packed beds, spherical beads and granular media as porous domain, extensive body of experimental research related to 'metal foams', a sub-class of porous media, emerged during 1990's, which is discussed later.

The porous materials can be classified in many ways based on their applications, properties, morphological parameters, materials, manufacturing routes, etc. Here, we base our discussion using the classification provided by Liu and Chen [1] and Ashby [51] (Fig. 2.1). Based on their nature of occurrence, the porous materials can be natural [52,53] (e.g. lava rocks, wood) or artificial (manmade structures). These artificial porous materials are further divided based on the class of materials used for their manufacturing such as, a) porous metals, b) porous ceramics, c) and polymer foams. Ashby [51] provided a similar categorization but used the term ‘cellular solids’ or ‘lattice-structured materials’ for porous materials and referred to foams as subset of lattice-structured materials. These artificial porous materials can be further classified based on porosity such as, a) low, b) medium, and c) high porosity materials. High porosity materials are then further divided into four classes based on the pore and solid matrix morphology, viz. a) honeycomb and lotus-type materials [54,55], b) open-cell foams [56,57], c) closed-cell foams [58], d) half open-cell foams [1].

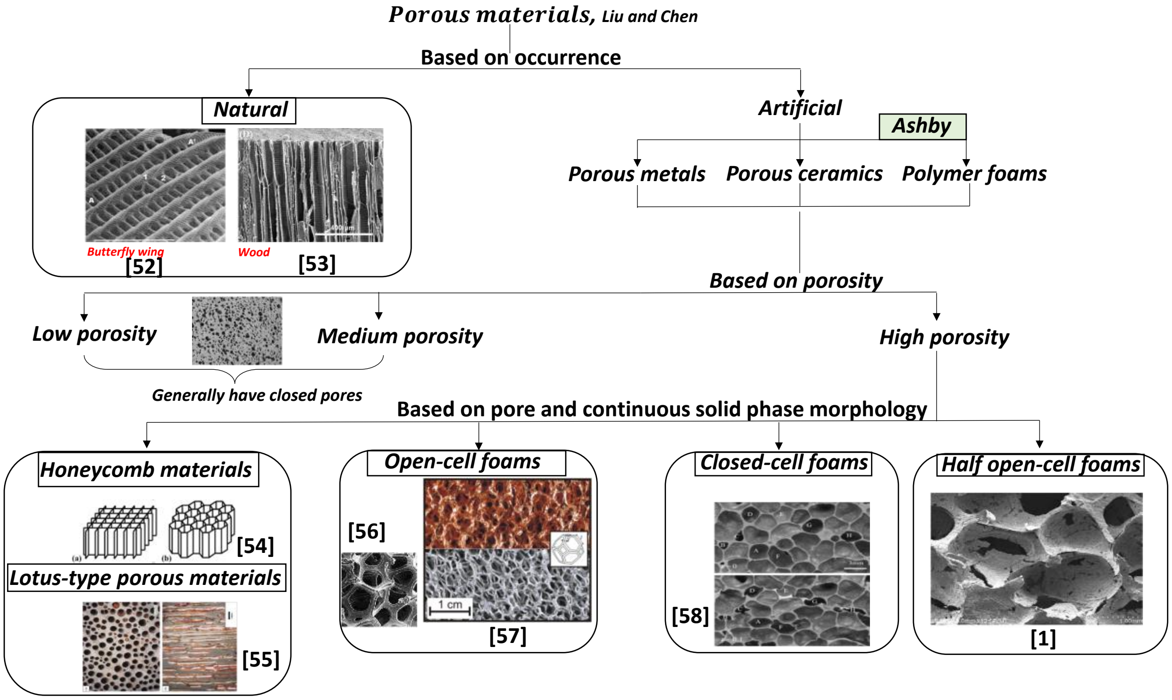

Figure 2.1 Classification of porous materials as per Liu and Chen [1] and Ashby [51]

Honeycomb materials [54,59] are two-dimensional arrays of polygons having long columnar type pores which are generally of the shape of a triangle, quadrangle or hexagon. Lotus-type porous materials derive their name from the roots of lotus-plant due to the structural similarity.

The lotus-type porous materials [55,60], also have unidirectional columnar type pores similar to that of honeycomb materials. The elongated pores formed by the release of gas while unidirectional solidification of molten metal results in circular or elliptical-shaped pores which are generally irregular and may not run through the entire length of the foam. Open-cell metal foams are formed by reticulated three-dimensionally interconnected fiber/strut network [56,57,61]. Three-dimensional porous materials having fully closed pores or cell faces separating the adjacent cells are called closed-cell foams [58,62]. The solid-fluid matrix in which both the open and closed pores are present, constitute the half open-cell foam category [1].

Vast literature pertaining to different types of porous media discussed above exist in open literature. The present study is focused primarily on high porosity open-cell metal foams. Although the open-cell metal foams are multifunctional, the paper is aimed towards their application in advanced heat exchangers. Post 1980, many experimental, analytical, and computational studies on high porosity open-cell metal foams were reported. These foams are lightweight materials which exhibit excellent mechanical properties (strength and stiffness), have higher permeability, high effective thermal conductivity, and offer large specific area for convective transport. The complex interconnected web-like network of struts enhances fluid mixing and hence, results in high heat dissipation, due to the tortuosity provided to the fluid path. The literature survey on open-cell metal foams reveals that a comprehensive understanding of flow and thermal transport phenomenon in metal foams exists at present. This includes the pressure drop characteristics, volume-averaged interfacial heat transfer coefficient, analytical expressions and experimental data on effective thermal conductivity, identification of various flow regimes and corresponding transition Reynolds numbers from laminar to turbulent, relevance of different characteristic lengths for parameter normalization, representative unit cell deductions, macro- and pore-scale simulations, etc. Thorough discussion and summary on different aspects of open-cell metal foams can be found in some excellent review articles, e.g. [22,63–65]. Open-cell metal foams investigated in the studies mentioned above are essentially an irregular arrangement of their so called "representative unit cells" which are uniquely identified by pore density (PPI), porosity (ε) and solid-phase material. The conventional manufacturing routes, which are discussed in the forthcoming sections, provide limited control over the morphological parameters, strut shape, fiber connections and metal accumulation on the strut junction (with decreasing porosity). Moreover, the metal foams were generally, either brazed or attached to test surfaces via. thermal pastes, thus imposing added thermal resistance at the substrate-strut interface.

There have also been many studies on lattices comprising of user-defined unit cell topologies or strut connections orderly patterned in three-dimensional space to characterize the mechanical and thermal-hydraulic properties of sandwich type lattice-frame configurations where the struts are arranged between two parallel plates [66]. Such lattices exhibit good load-bearing capabilities and have high thermal-hydraulic performance as well, with appropriate choice of solid-phase material. The fabrication techniques used for these lattices poses restriction on the minimum achievable dimensions and truss connection complexity.

The limitations in the traditionally procured open cell metal foams and structured lattices obtained by conventional techniques could possibly be eliminated by the advancements in the recent additive manufacturing (AM) technologies. Regular metal-lattices manufactured using additive manufacturing is an ordered arrangement of representative unit cell topologies built using a CAD model and patterned in three-dimensional space. The user has more control on the strut size, strut orientation and strut shape. The lattice network can be fabricated directly on the substrate surface, thus, eliminating the additional contact resistance as well. Additively manufactured heat exchanger development has gained significant traction lately, where efforts are focused towards achieving complex shapes with smaller length scale features with high-accuracy and reduced surface roughness.

In this review, we are presenting a case study on the AM efforts pertaining to the printing of lattice materials, which have strong potential to be used in many heat exchanger applications mentioned above. The present study is divided in three major sections to answer some critical questions pertaining to these lattices. The following Section 2.2 provides a brief description on processes for manufacturing stochastic metal foams and regular metal lattices. An account of different studies pertaining to the flow and thermal transport behavior of regular lattices is also provided. Section 2.5 presents popular additive manufacturing technologies which have been used for printing lattices of complex unit cell topologies where we provide insight into the freedom of material choice and minimum achievable morphological dimensions/sizes. The heat transfer, pressure drop data and applications of these lattices is presented in detail. The above analysis is conducted to answer the following questions in conclusion (section 2.6). (1) What are the advantages and limitations of the regular (ordered) lattices with respect to extensively investigated stochastic metal foams? (2) minimum lengths-scales of features that could be achieved through AM route in reference to the commercial foams? (3) can ordered lattices made via. conventional routes and through AM replace the stochastic metal foams in heat exchanger applications? This review article is aimed to provide an account of the progress made in the metal AM sector pertaining to the lattice printing, from the perspective of heat exchanger development.

2.2 Manufacturing processes of commercial open-cell metal foams and lattices

2.2.1 Open-cell metal foams

The manufacturing routes of metal-foams are described in detail by several authors [1,67,68]. One of the most common ways is the *foaming* process in which a molten metal is foamed by generating gas-bubbles by either, a) passing the gas into a melt from external source, b) production of gas in the molten melt by mixing it with gas-releasing blowing agent, or c) precipitation of gas already dissolved in the liquid metal. The formed metal-gas bubble mixture rises above the dense liquid metal, which then solidifies into dry metal foam after acquiring a stable equilibrium configuration with minimum surface-area energy. The formation of foams is generally stabilized by addition of stabilizing agents which also controls the viscosity of the liquid melt. These manufacturing techniques generally produce closed-cell or half-open cell foams.

Open-cell metal foams are more desirable for heat transfer applications since they offer relatively higher permeability for flow through them and are lightweight. Describing all the manufacturing techniques of open-cell metal foams is not the scope of this paper and only a selected few of them are briefly presented here in the interest of brevity.

2.2.1.1 Investment Casting method

Figure 2.2a shows the schematic of a typical investment casting process used to produce high porosity open-cell metal foams. In this process, an open-cell polymeric foam template made by *foaming* process is filled with slurry of heat resistant material. The slurry is left to dry, following which the polymer is removed by thermal treatment. Removal of the polymer foam leaves behind an empty mold of open-cell foam template, which is then filled with metal. Post metal solidification, the dried slurry mold is removed, e.g. by pressurized water [68], yielding the final open-cell metal foam structure. The foam manufactured through this process have almost same purity as that of the parent material and the process has been found to be repeatable. The quality of the final product depends on complete filling of the polymer foam cavity, control on the directional solidification and damage to the struts while removing mould.

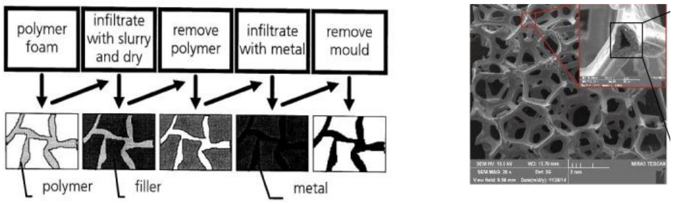

(a) (b)

Figure 2.2 a) Schematic of the investment casting process [68], b) Hollow struts of the metal foam [69]

2.2.1.2 Vacuum Vapor deposition

A precursor open-cell polymer base is required for this procedure as well. The metal is heated and vaporized in a vacuum environment by electron beam, electronic arc, etc. and subsequently deposited on the polymer foam template. When the layers of metal on the struts solidify, the base polymer is then removed in reductive environment of hydrogen gas (H_2)and is further sintered to obtain the final open cell metal foam. The vapor density and deposition time controls the thickness of the deposited metal layer.

2.2.1.3 Electrodeposition

Similar to the above two procedures, this process also requires a polymer foam template where the polymer base is dipped in an electrolytic solution containing metal ions which deposit on the polymer struts. The polymer foam is finally removed to obtain the open-cell metal foams.

The pretreatment of the polymer base is required to ensure the surface is clean and electrically conducive to support metal ion deposition.

These processes allow the usage of aluminum (Al), copper (Cu), zinc (Zn), nickel (Ni), silver (Ag), gold (Au), iron (Fe), magnesium (Mg), etc. for fabricating metal foams. Amongst these metals, aluminum alloys and copper are of interest to heat transfer community because of their higher thermal conductivities. Further, aluminum foams offer an added advantage of being lightweight as well. Although a similar polymer base structure could be used for producing metal foams in the above three methods, one striking difference in the final metal foam is that the struts produced by investment casting are solid in nature while the ones produced by metal deposition and sintering routes are hollow, as shown in Fig. 2.2b. In heat dissipation, the composition of the struts plays a significant role. Moon et al.[69] demonstrated that copper foams with hollow struts (ratio of hollow to total area of strut cross-section of 0.79) provided 40% less heat transfer enhancement than the solid struts. The hollow struts are more suitable in chemical reactions such as nickel foams in batteries or catalytic reactions where surface area availability for reaction is a priority over the heat transfer. Although, the thermal properties of deposition process-made metal foams are also investigated, the convective heat transfer is mostly investigated for solid struts, with aluminum and copper alloys as solid-phase materials.

Table 2.1 provides details of the morphological parameters of test samples from selected experimental studies. Typical pore diameter ranged from 1.7 mm to 6.9 mm and strut diameter ranged from 0.08 mm to 0.66 mm. The porosities for these samples was greater than 0.85 in general, except for the one investigated by Hwang et al. [70]. The convective heat transfer and pressure drop studies typically involved test samples with porosities greater than 0.9 and surface area to volume area ratio range of 790 m^2/m^3 to 2740 m^2/m^3.

Table 2.1 Open-cell metal foam properties of the samples used in the experimental studies

Reference	**Year**	**Pore diameter, d_p (m)**	**Strut diameter, d_f (m)**	**Pore density, PPI**	**Porosity, ε**	**Specific area, $a_{sf}(m^2/m^3)$**	**Overall block dimensions(mm)**	**Material of solid matrix**	**Special comments**
Calmidi and Mahajan [71]	2000	0.00402 0.00380 0.00313 0.00270 0.00258 0.00202 0.00180	0.00050 0.00055 0.00040 0.00030 0.00035 0.00025 0.00025	5 5 10 20 20 40 40	0.9726 0.9118 0.9486 0.9546 0.9005 0.9272 0.9132	--	63 x 45 x 196	Aluminum alloy (T-6201)	• Metal foam was brazed to 9.5 mm thick Aluminum sheets for heat transfer measurements • Air was the working fluid
Kim et al. [72]	2001	--	--	10 20 40	0.92	790 1720 2740	90 x 9 x 188	Aluminum alloy (6101)	• C-shaped clamps were used to compress the channel walls bounding metal foam against each other. The compression was increased until heat transfer rate reached an asymptotic value • Air was the working fluid
Boomsma and Poulikakos [73]	2002	0.0069 0.0036 0.0023	--	10 20 40	0.921 0.920 0.928	820 1700 2700	12 x 38 x 80	Aluminum alloy (6101)	• Only hydraulic-characteristics were determined • Water was the working fluid
Hwang et al. [70]	2002	0.00184 0.00192 0.00203	0.00036 0.00036 0.00036	-- -- 10	0.70 0.80 0.95	--	60 x 25.4 x 60	Aluminum alloy (6101-T6)	• High-conductivity epoxy used to create thermal contact between foam and copper base plates • Air was the working fluid • 0.70 and 0.80 were obtained by compressing 0.95 sample • The dimensions in pore diameter column are the mean cell diameter values
Giani et al. [74]	2005	0.0043 0.0047 0.0022 0.0020 0.0017	0.00066 0.00082 0.00037 0.00033 0.00028	5.9 5.4 11.5 12.8 15.0	0.945 0.927 0.938 0.937 0.932	333 352 696 767 942	Foams were placed in 9mm inner diameter tubular reactor	FeCr alloy (73% iron, 20% chromium, 5% aluminum, 2% yttrium)	• Mass-transfer properties of metal foams were investigated for catalyst support applications
Mancin et al. [75]	2010	0.00508 0.00254 0.00254 0.00254 0.00127 0.000635	0.000540 0.000529 0.000450 0.000445 0.000367 0.000324	5 10 10 10 20 40	0.921 0.903 0.934 0.956 0.932 0.930	339 839 692 537 1156 1679	100 x 40 x 100 100 x 40 x 100 100 x 40 x 100 100 x 40 x 100 100 x 40 x 100 100 x 40 x 100	Aluminum alloy (6001)	• Foams were brazed between 10 mm thick aluminum plates • Air was the working fluid
Mancin et al.[57]	2013	--	0.000495 0.000432 0.000320 0.000244	5 10 20 40	0.935 0.934 0.935 0.936	292 692 1134 1611	100 x 40 x 100	Copper	• Foam core was brazed between 10 mm thick plates Air was the working fluid

Table 2.1 (continued)

Wulf et al. [76]	2014	0.0005-0.001 0.0006-0.0014 0.0008-0.003 0.0003-0.0007 0.0009-0.0024	--		0.85 0.87 0.88 0.89 0.90	--	--	FeCrAl alloy	• Study focused on the effective thermal conductivity of metal foams
Kaya and Fleck[77]	2014	0.00178 0.00107	0.00012 0.00008	30 45	--	--	20 x 20 x 20	Stainless steel 316L	• The aim of the study was the measurement of deformation of metal foams • The dimensions in pore diameter column are the mean cell diameter values
Oun and Kennedy [78]	2015	0.000214	--	--	0.880	--	25 mm diameter samples with 20 mm thickness	Inconel 625 alloy	• Only hydraulic-characteristics were determined • Air was the working fluid

Different block shapes such as rectangular block of varying aspect ratio and cylindrical block for tubular heat exchangers have been extensively studied, demonstrating the machinability of fabricated metal foams for their usage in complex geometries.

2.2.2 Regular lattices

The stochastic metal foams are by definition random, and users do not have much control on the morphological parameters. The attachment of such metal foams to the substrate from which the heat is to be dissipated is also challenging. Regular lattices formed by arranging a given unit cell periodically have the potential to overcome above limitations. Generally, the investigation of such lattices are of interest in the field of mechanical design, materials, and civil engineering, therefore, a broad range of work focused on finding the load-bearing capabilities and failure modes of these structures exist in open literature. Although the stagnant thermal properties such as effective thermal conductivity is explored extensively for these structures, only recently there have been some experimental and numerical investigations on the convective heat transfer and pressure drop on these lattices. These regular lattices can be manufactured in the form of sandwich panels, where single-layer of strut-based unit cells join the two opposite plates, or a block formed by several layers of representative unit cells. The different manufacturing methods and the resulting topologies of regular lattices provided in the studies [79–82] is presented in Fig. 2.3. The regular lattices, based on fabrication techniques, can be classified as the ones obtained from, a) metal-wire approach, b) investment casting, c) sheet-metal bending, d) additive manufacturing. Description of the manufacturing technologies and flow and thermal transport studies of hence obtained lattices is presented below.

2.2.2.1 Metal-wire approach

Metal-wire approach yields lattices by weaving or braiding the metal wires. Since these are obtained by weaving, they are commonly referred to as *textile cores*. Both sandwich-panel type configuration, where a single layer of weaved metal wire is sandwiched between two parallel plates, and multilayered wire-woven metal block can be produced via. this approach. Topologies such as simple 0/90º and ±45º weave, Kagomes, circular and hexagonal Kagomes, wire-woven bulk Kagomes (WWBK), etc. are common examples of lattices fabricated through this method. The limitation of this process is that it could be used for only those metals which can be drawn into wires and the automated weaving of complex topologies is still not fully advanced. Kang [82] provided a detailed description of different types of wire-woven metal lattices and recent advances in the automated technologies used for weaving metal wires. The bonding at the intersection of the wires plays a critical role in determining the heat transfer properties of weaved lattices. Different techniques such as resistance welding, soldering or brazing and transient liquid phase (TLP) [83] are employed, the choice of which is primarily dependent on the parent material.

From thermal and flow transport perspective, some studies have explored the effects of pore shape (square and diamond), flow orientation (axial or bifurcated), surface area density, porosity and solid-to-fluid thermal conductivity ratio on the heat transfer and pressure drop characteristics [84–87] of woven textiles made from copper and stainless steel. For a fixed surface area density, optimal porosity of ~0.75 provided the maximum heat dissipation for copper textiles. Analogous fin-model approach was developed to predict the heat transfer of textile lattices. With water as the working fluid, the model predictions were in good agreement with the experimental data only when thermal dispersion effects were included. Joo et al. [88,89] investigated the friction factor and heat transfer characteristics of multilayered wire-woven bulk Kagome (WWBK) made of aluminum helix wires for different flow orientations. It was observed that the flow was primarily dominated by skin friction in the laminar regime and form dominated at high Reynolds number where transition to turbulent flow regime occurred.

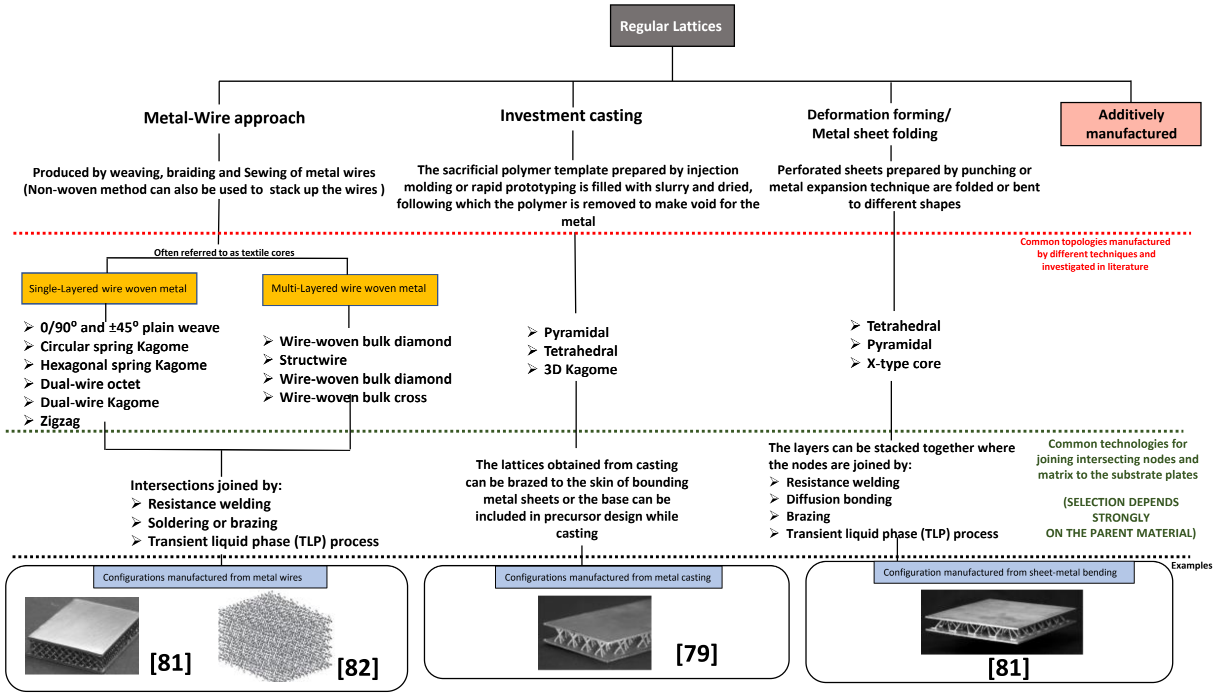

Figure 2.3 Categorization of regular lattices according to manufacturing techniques, note: additive manufacturing segment is expanded in a later section

Analytical and numerical work has been conducted to model the effective thermal conductivity of textile core lattices [90–93]. The effect of the anisotropy, stacking pattern, and brazing at the intersections on the overall effective thermal conductivity was investigated. Xu and Wirtz [92] determined the effective thermal conductivity of copper plain-weave screen laminates to be 23% (isotropic) and 78% (anisotropic) of the parent metal, much higher than that provided by metal foams. Few studies such as that published by Yang et al. [94] reported the natural convection characteristics of the WWBK where the heat transfer enhancement provided by the WWBK was ~62% higher than the traditional metal foams. The convective heat transfer, natural heat transfer and stagnant thermal properties (e.g. effective thermal conductivity) are mostly explored for the 0/90º and ±45º plain weave (which generally results in square and diamond shaped-pores), simple anisotropic Kagome, multilayered WWBK and wire-screen laminates.

Several studies have focused on the augmentation of thermal performance of solar absorbers, solar heaters and tube heat exchangers using wire-mesh structures [95-99]. The wire screen meshes performed either comparable or better than the contemporary metal foam heat exchanger assemblies and that too at lower cost (almost one fourth of the metal foams). With wire mesh as the packing material, Prasad et al. [96] showed that enhancement of efficiency of meshed heater relative to baseline conventional heater was a strong function of mass flow rate and porosity of wire-mesh. For the range of porosities investigated, enhancement values of 89.5% (at minimum flow rate) to 76.9% (at maximum flow rate) could be achieved. Sayed et al. [100] studied the performance enhancement of pipe heat exchangers by employing the copper alloy wire mesh and compared its performance to the finned heat exchanger. The Nusselt number enhancement provided by the wire-mesh heat exchanger was about 2.3 times higher than that without mesh while incurring maximum pressure drop value of ~598 Pa. At fixed pressure drop conditions, the wire-mesh covered pipe heat exchanger provided similar heat transfer coefficient to the finned tubes but lower than that wrapped by metal foam. In another study, Kurian et al. [98] showed that wire-meshed pipe heat exchanger could yield about ~ 28% higher Nusselt number values than the metal foam heat exchanger. The overall thermal-hydraulic performance of wire-mesh was therefore, 40-50% higher than the foam heat exchangers and that too at much lesser cost. Similar conclusions of mesh with respect to metal foam heat exchangers were reported in [101].

There exist many configurations such as spring Kagomes, dual wire octet, dual wire Kagome, etc. which are yet not investigated for the thermal transport characteristics. The experimental work to determine the effective thermal conductivity, natural convection heat transfer and pore-scale simulation for flow visualization is still scarce relative to the conventional foams. Since the plain weaves and basic Kagome structures have different topologies than the spring and dual wire Kagomes, the generalization and applicability of existing models to these structures cannot be extended with confidence. The literature suggests that the textile cores have comparable thermal performance to that of stochastic metal foams and relatively cheaper to manufacture. Investigation of the aforementioned areas can provide more comprehensive understanding of flow and thermal transport of these textile-core lattices as they are suggested to be the potential alternatives to stochastic metal foams.

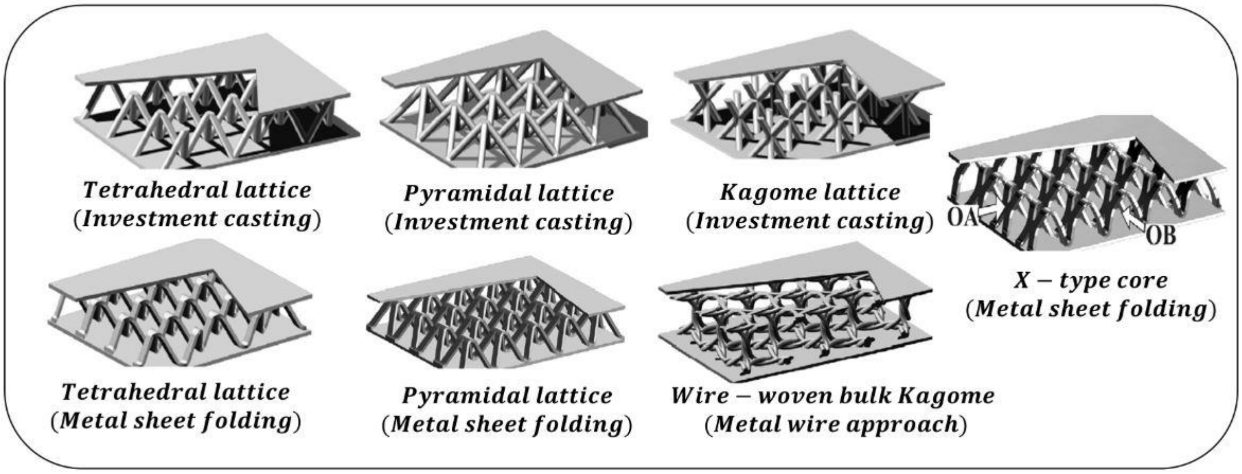

Figure 2.4 Similar topologies obtained from different manufacturing routes [102]

2.2.2.2 Investment casting

Investment casting method is already explained in the Section 2.2.1.1. The only difference is that *foaming* process is used to make sacrificial polymer template for stochastic metal foams, whereas injection molding or rapid prototyping is used for regular lattices. This method is widely used to produce sandwich panel lattices with tetrahedral, pyramidal and Kagome unit cell topologies as shown in Fig. 2.4. Tetrahedral and pyramidal topologies are alternately manufactured by metal-sheet folding technique as well. Therefore, the flow and heat transfer properties of these structures are discussed together later.

2.2.2.3 Metal-sheet folding

Figure 2.5 shows the schematic of the metal-sheet folding/bending technique. A perforated sheet is punched on a die to bend the sheet at the nodes. Hexagonal and diamond shaped perforations result in tetrahedral and pyramidal truss core lattices, respectively. Recently, the flow and thermal transport mechanisms of X-shaped core, manufactured by metal-sheet folding, is being investigated extensively, an account of which is provided below.

2.2.2.4 Additive manufacturing

Additive manufacturing is a computer-controlled process in which a three-dimensional object is created by layer-upon-layer addition of base material. The process details and the synthesis of metal-based complex unit cell topologies manufactured via. this technique that has been employed in heat transfer enhancement applications are discussed in the next section.

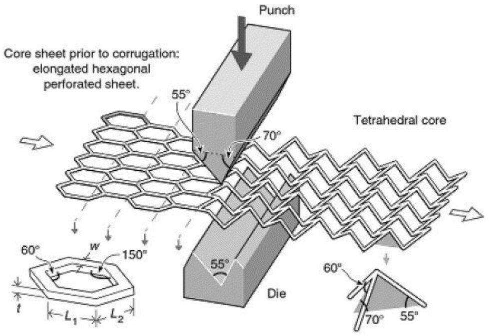

Figure 2.5 Schematic of the metal-sheet folding procedure of sheet with hexagonal pores to produce tetrahedral truss core [79]

2.3 Applications of lattices in thermal management

Some of the potential areas of applications of metal foams have already been highlighted in the beginning of Section 2.1. Catalytic reactors, filtration, solar absorbers, and micro-electronic cooling are common venues for employment of metal foams due to their high surface area-to-volume ratio and heat transfer capability. Simple weaved meshes are also sought after technologies for these applications [103–106]. Thin layer of porous materials is very beneficial in enhancing the performance of devices working on principles of multi-phase flow physics. For e.g. thin layer of honeycomb provided about 2.5 times higher critical heat flux values (CHF) in saturated pool boiling relative to the plain surface in a study by Mori et al. [107]. Microchannels with a layer of diffusion-bonded woven copper mesh laminate [108], stochastic metal foams with uniform and graded porosity [109–111], metal foams in the form of V-shaped grooves [112] and micro-fins with wire mesh [113,114] have all been the subject of investigation as pool boiling surface enhancements. Recently, additively manufactured lattices are being considered as potential surface enhancement features for improving the pool boiling performance. Zhang et al. [115] was successful in achieving three times CHF relative to plain surface by using a grid structure made via Selective Laser Melting technique. Additively manufactured Octet unit cell lattice was investigated by Wong et al. [116] who reported heat transfer coefficient enhancement of about ~2.81 times in comparison to plain surface. Sustained liquid replenishment, delayed CHF, required capillary suction effect and availability of numerous active nucleation sites are key features of these porous structures in defining the pool boiling performance.

In recent times, the ability of additive manufacturing technologies is being exploited to design and manufacture cooling mechanisms for turbine technology. Film cooling [117] and transpiration cooling are important cooling mechanisms to keep the temperature of turbine blades within permissible limits. In transpiration cooling, the coolant is discharged through a porous material and then forms an insulating layer between the incoming hot gases and blade surface. Heat dissipation due to large surface-area to volume ratio and uniform layer formation of coolant due to high pore density at the surface are the unique characteristics of transpiration cooling mechanisms. Sintered structures, woven wire-meshes and metal foams were considered appropriate choice as porous material for transpiration cooling, but these structures were not able to provide required mechanical strength, homogeneous pore distribution, high porosity, flexibility in design and shape at the same time. The difficulty in realizing a porous structure with desired qualities for the transpiration cooling from thermal-mechanical and manufacturing perspective limited the use of this technology. However, revived interest in investigating the transpiration cooling is observed due to some recent studies reporting transpiration cooling performance of additively manufactured customized, homogeneous, and high strength structures[118,119].

Heat pipes are another passive two-phase technology which use sintered or woven material as wicks to assist the flow of condensate from the condenser to the evaporator section by the assistance of capillary forces. Recently, oscillating heat pipes, and wicks composed of octahedral unit cells manufactured via additive manufacturing have been investigated by several authors such as Ibrahim et al. [120] and Jafari et al. [121].

This section provides an insight into the broad range of lattice applications and the instances where the additive manufacturing technology is being considered an alternative to create structures for mitigating the disadvantages that lattices from conventional technologies have.

2.4 Flow and thermal transport in conventional lattices

Figure 2.4 shows common topologies which are employed in the fabrication of multifunctional lightweight heat exchangers prepared by metal-wire approach, investment casting and metal-sheet folding [102]. Kim et al. [66,122,123] and Son et al. [124] investigated the tetrahedral truss core lattice-frames with circular strut cross-section. Circular struts could be produced by metal investment casting or additive manufacturing techniques. Tetrahedral unit cells are anisotropic in nature as shown in Fig 2.6a as two flow orientations are possible, OA and OB. The effect of anisotropy on the flow pattern, local endwall heat transfer distribution via. TLC (Fig 2.6b and 2.6c) and steady state experiments, vortex formation and flow separation through PIV techniques, effect of solid thermal conductivity on the overall heat transfer by comparing strut core made from aluminum alloy to that from polycarbonate sheet, relative heat transfer contribution from the strut surface and the endwall surface were studied in detail by the authors over a wide range of Reynolds number. Son et al. [124] reported the transition to occur at Reynolds number based on channel hydraulic diameter ($D_h = 4\epsilon V/A_s$) equal to 1,000 for porosities ranging from ($0.75 < \epsilon < 0.98$). Kim et al. [66] observed transition for Reynolds number (based on unit cell length) 2,000<Re_{d_p}<3,000 at porosity ~0.94. Pressure drop encountered for orientation OA was higher than OB because of higher blockage ratio of the configuration but the overall mean thermal values were similar for both the configurations.

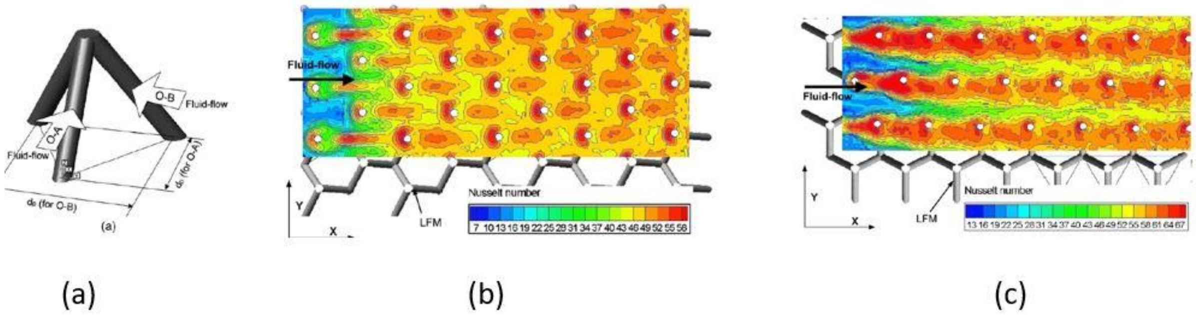

(a) (b) (c)

Figure 2.6 (a) Different flow orientations for tetrahedral truss core, (b) Nusselt number distribution on the endwall for orientation OA, (c) Nusselt number distribution on the endwall for orientation OB [66]

Zhang et al. [125] numerically compared the thermal and hydraulic performance of tetrahedral truss core sandwich panels manufactured from casting (circular struts) and metal-sheet folding (rectangular strut cross-section). At a fixed porosity, the struts that were manufactured by cost-effective metal-sheet folding method provided 13-16% higher overall heat transfer than casted sample while encountering 1.6 to 1.7 times more pressure drop due to more intensified vortex formation at the wider and sharp vertex nodes.

Yan et al. [126,127] introduced X-type lattices cores recently which could be manufactured by cost-effective sheet folding method (unit cell shown in Fig. 2.7a). Pyramidal and X-lattice cores could be manufactured from the same sheet mold by punching at different locations as shown by Jin et al. [128]. Figure 2.7b shows different types of unit cell topologies which can result from punching location shift. The punching location shift has significant impact on the final topology and consequently on the flow and thermal behavior of the lattice. Yan et al. [127] established that for a fixed pumping power, X-type cores provided higher heat transfer and thermal efficiency as compared to tetrahedral truss cores and Kagome structures whereas Jin et al. [129] demonstrated that X-lattice cores could outperform the pyramidal lattice cores. From these recent studies, X-lattice cores seem to provide the better thermal performance than the conventional tetrahedral, pyramidal and Kagome structures at same porosity and power consumption.

Very often a combination of the existing cooling technologies for heat transfer enhancement is studied to achieve higher thermal-hydraulic performance. Many such studies exist in literature where dimple-pin fin, rib-dimple, winglet-dimple, dimple-protrusion, etc. combination pairs were explored. Two types of heat transport mechanisms exist in the sandwich type panels: a) convective heat transfer from the endwalls, and b) convective transfer of the heat which is conducted through the struts via. conduction from the heated substrate. The endwall heat transfer can be in significant proportion for high porosity structures, which could be further enhanced by employment of turbulence-inducing features on the wall such as dimples, pins, and profiled-protrusions. Ma et al. [130,131], Li et al. [132] and Yan et al. [133] compared the hydraulic and thermal performance of the X-type core and pyramidal core in combination with rectangular honeycomb structure, pin fins, dimples, and protrusions (Fig 7c). The combination configurations in all these studies thermally outperformed their parent single-feature type configurations at fixed pumping power conditions. However, the heat transfer enhancement for the investigated range of Reynolds number by Li et al. [132] with pin-fin configurations was just ~5% higher than the X-lattice whereas the pin-fin combination configuration investigated by Ma et al. [130] yielded Nusselt numbers of about ~9% higher than the parent pyramidal structure at fixed pumping power conditions. The combination configuration studies are limited, mostly numerical in nature and have the potential to be explored for different parent lattices and various turbulence-enhancing feature parameters.

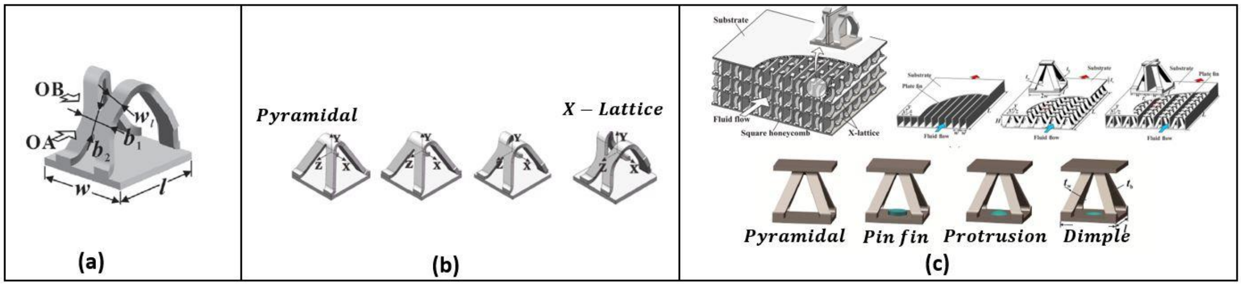

Figure 2.7 (a) Unit cell of X-type core [127], (b) Different topologies generated by different punching locations [128], (c) Combination configurations of X-type/pyramidal truss cores with honeycomb, pin-fin, dimple, and protrusion [130,131,133]

Normalized heat transfer coefficient (Nu), friction factor (f) and efficiency index ($Nu/f^{1/3}$) for different porous media as presented by Tian et al. [84] is shown in Fig. 2.8. The configurational and operational parameters from selected studies is presented in Table 2.2. The characteristic length chosen for normalization is generally the channel height or unit cell length for these configurations. For consistency, the non-dimensional parameters in Table 2.2 are normalized with the channel height. The wire screens/textile cores have higher or similar heat transfer performance to the conventional stochastic metal foams with an added advantage of comparable pressure drop penalties. However, the data presented here for wire-screens is at the porosity range of ~0.7-0.8 but the open-cell Al foam porosity is ~0.9.

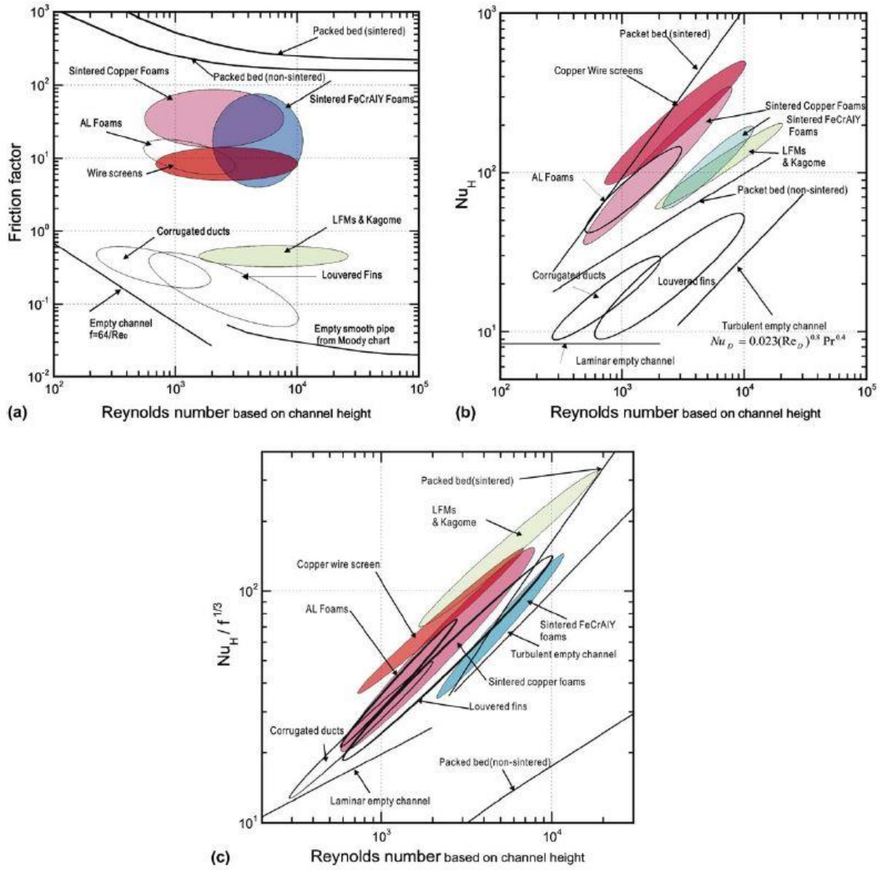

Figure 2.8 (a) Friction factor, (b) Nusselt number, and (c) Efficiency index, of different heat transfer enhancement media [84]

Table 2.2 Configurational, operating and resulting flow/thermal information from selective studies (air as working fluid)

Reference	**Configuration**	**Expt.**	**Comp.**	**Material**	**SSA** (m^2/m^3)	**Porosity**	**Overall dimensions W X H X L (all in mm)**	**Strut diameter (mm)**	**Flow-conditions**		**Thermal characteristics**		**Flow-characteristics**
									Re	**Velocity (m/s)**	**h** (W/m^2K)	**Nu**	**f**
[84]	Wire-weaved mesh with square and diamond pores	✓		Copper	1496	0.68	40 x 10 x 60	0.8	700-10000	1.0-10	336-957	128-365	17-22.5
[88]	Wire-woven Kagome	✓		Aluminum	123	0.962	150 x 25 x 150	1	1167-11667	1.1-8.0	74-453	71-435	0.2-0.83
[66]	Tetrahedral truss	✓		Aluminum	123.68	0.94	127 x 12 x 127	2	1228-4724	1.6-6.17	107.7-226	50-104	Almost constant in turbulent regime, ~ 0.58
[127]	X-type core	✓	✓	Stainless-steel	205	0.932	132 x 9.66 x 60	0.91	1400-7500	2.7-12.6	193-396	71.7-147	Almost constant ~ 2.58

Expt. – experimental, Comp. - computational

The surface area densities of these textile cores have similar order of magnitude to the metal foams (Table 2.2). Wire weaved copper mesh has surface area density of 1,496 m^2/m^3 at porosity of 0.68 (Table 2.2) whereas similar range of surface area densities are easily achievable for stochastic open-cell metal foams at porosity values greater than 0.9. A study by Boomsma et al. [12] showed that with a compressed foam, surface area density of 10,000 m^2/m^3 could be achieved. When compared to conventional heat exchangers, the compressed foam decreased the thermal resistance by half at the same operating conditions. A thickness of about ~2 mm could be realized for these foams which can also make the heat exchanger lightweight and compact. Whereas there exist applications where a single layer of wire-mesh structures or even matrix is much more convenient to employ because of its lower cost and ease in fabrication.

The heat transfer enhancement provided by tetrahedral, pyramidal and X-lattices are relatively lower than the wire woven textiles, due to lower surface area density, but also incur lower flow losses. These structures are desirable where heat transfer and mechanical properties are both important. The selection of a particular technology is dependent on the application and geometrical and operational constraints because a thermally optimized geometry might not be the optimal option for mechanical applications [134].

From the discussion presented in this section, it can be concluded that the stochastic metal foams are expected to stay in the commercial market for the near future and continuous improvements in the conventional processes is necessary. Continuous effort to develop techniques for better bonding to the heated substrate is imperative.

2.5 Additive manufacturing (AM) of regular lattices

Additive manufacturing is a technology that builds a 3D object by layer-upon-layer addition of the material. The current additive manufacturing technologies provide freedom of building the regular lattices for a wide range of morphological parameters, unit cell topologies and different materials such as ceramics, metals, and resins. This section is focused on the extent of the freedom that these technologies provide to manufacture metal based regular lattices for heat exchangers.

Figure 2.9 provides a classification of AM technologies into seven categories as per "ASTM F42-Additive Manufacturing". The seven classes are described below:

(1) VAT Photopolymerization – In this technology, the photopolymer resin is exposed to the light of a specific wavelength which undergoes chemical reaction to solidify post exposure. The 3D part is printed by solidifying one layer at a time. Only resins could be processed in this technology.

(2) Material Jetting – Material is jetted from nozzles of the printhead onto build platform in the form of layer which is cured and solidified by the UV light. The next layer is then built on the solidified layer. This process requires the generation of supports which are removed in post-processing. Polyjet, Nanoparticle Jetting (*NPJ*) and Drop-On demand (*DOD*) technologies work on this principle. While NPJ could process stainless steel, this technology is primarily employed on polymers and waxes only.

(3) Binder Jetting – This technology typically employs two types of materials, viz. powder-based material and adhesive binding agent (usually in liquid phase). The printhead moves over the powdered bed depositing the binder material to map the layer. The bed is lowered and coated with powder material again to apply another layer of binding agent. The alternate layers of base material and binding material are generated to produce the final product. Often times, the loose material in the job box provides support to the building structure without requiring the formation of additional supports. Ceramics (silicon carbide, alumina), sand material (silica) and metals (stainless steel, cobalt-chrome, tungsten, inconel) could be used as the base powder material. These parts are

infiltrated (metals are infiltrated with bronze) to improve the mechanical properties. Due to binding agent, the parts manufactured by this technology are not always recommended for structural purpose. Also, the necessary post processing adds additional time to the process.

(4) *Material Extrusion* –In this technique, the filament shaped material is pushed through a heated nozzle under constant pressure and in continuous manner where it melts and is deposited in pre-coded path. The nozzle moves continuously over the bed depositing the layers which fuses together because they are in molten state and are eventually solidified. The parts require support structures during the fabrication process. This technology can process only polymers (acrylonitrile butadiene styrene (ABS), nylon, polycarbonate (PC)).

(5) *Powder Bed Fusion* –A layer of powdered material is spread over the bed which is then fused together at specific locations by laser or electron beam. Another coating of powdered material is spread over the previous layer which is again fused. This process continues until the entire part is formed. The loose powder behaves as a support structure, but sometimes additional supports can be created to avoid warpage due to residual stresses. Selective laser sintering (*SLS*), Direct metal laser sintering (*DMLS*), Electron beam melting (*EBM*), Multijet fusion (*MJF*), and Selective laser melting (*SLM*) are common technologies based on this principle. Amongst these, *SLM, DMLS* and *EBM* are metal based technologies which could process aluminum, titanium, stainless steel, nickel alloys and cobalt-chrome.

(6) *Sheet Lamination*–A sheet is placed on the cutting bed and another layer/sheet is bonded to the previous layer by adhesive and then cut into desired shape by a laser or knife. The next layer is then added, and the process is repeated until the whole part is printed. The second step could be reversed where a sheet can be first cut and then positioned and bonded to the previous layer. This method is limited to materials which could be formed into thin sheets.

(7) <u>Directed Energy Deposition</u> –A nozzle mounted on a multi-axis arm deposits material onto the surface in the form of powder or wire, which is melted on the deposition by laser, electron beam or plasma arc. The layer is then deposited, melted, solidified, and then covered with another layer until the parts is completed. Electron beam-based methods can process metals such as cobalt-chrome and titanium.

Regular lattices built by AM technologies have received considerable attention from the researchers in biomedical field and civil engineering [135,136]. Many prior studies have focused on the understanding of their mechanical response, flow permeability and fluid induced wall shear stresses. Figure 2.10 shows various unit cell topologies the mechanical properties of which were reviewed by Hanks et al.[135].

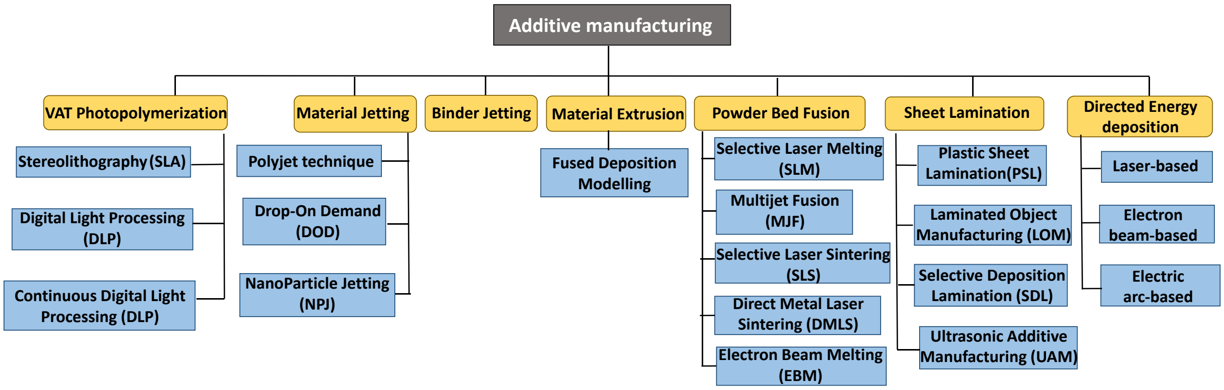

Figure 2.9 Classification of AM processes

2.5.1 Flow and thermal transport in additively manufactured regular lattices

Dedicated studies on flow and thermal transport in lattices are relatively scarce. Wong et al. [137] investigated five different types of heat sinks manufactured by *SLM* using Aluminum 6061, where fins of circular, rectangular, and elliptical shapes were studied (Fig. 2.11a). The round pin-fin and lattice heat sink had the lowest performance at fixed mass flow rate conditions whereas elliptical was the highest followed by rectangular. At mass flow rate of 4.3 x 10^3 kg/s, the lattice heat sink was able to dissipate only 54% of that dissipated by rectangular fins. The weak performance of the lattice structure, despite having the largest surface area to volume ratio, was attributed to presence of large temperature gradient in thin struts which reduced the fin-efficiency and the orientation of lattice channels along the length of flow direction which minimized the flow interaction with fibers. This finding provides an interesting perspective on lattices printed additively. A very complex structure can possess good mechanical properties but still have limited capabilities promoting convective transport, despite having large participating area in heat dissipation. Unit cell topology, orientation of the fluid flow in case of structural anisotropy, and morphological parameters such as fiber thickness and unit cell length are all specific areas of interest to the research community.

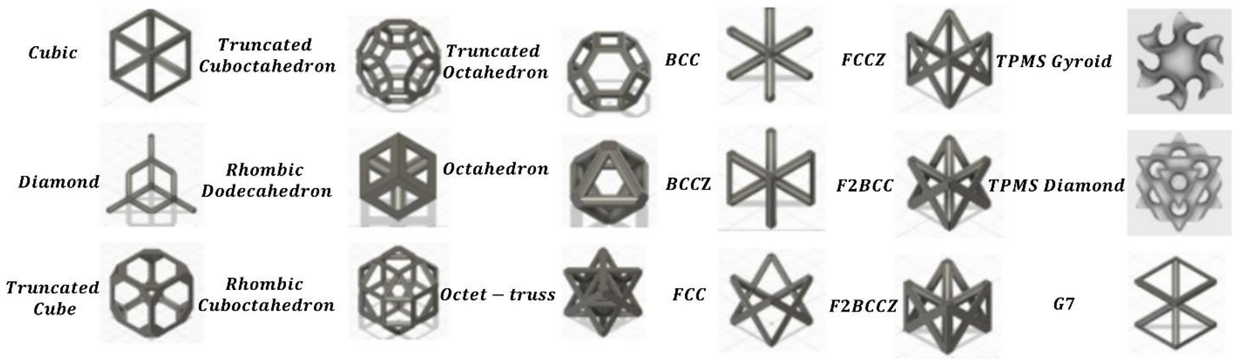

Figure 2.10 Unit cells of regular lattices[135]

Roughness control in *SLM* process remains a challenge [137]. Wong and Leong [116] studied pool boiling heat transfer of saturated FC-72 for octet-truss lattice structures having different unit cell lengths and same porosity. The samples (Fig. 2.11b) with three different unit cell sizes and heights were fabricated through SLM in AlSi10Mg alloy and the characterization test revealed that the surface roughness was similar in different unit cell length structures, therefore the overall trend of surface area-to-volume ratio was not impacted. Figure 2.11b shows the zoomed-in-view of the struts of lattice for different unit cells having roughness due to homogeneous distribution of partially-sintered powder, a characteristic which is typical of parts manufactured by SLM. This partially sintered powder was expected to serve as nucleation sites for bubble formation. The comparison with some existing studies using other surface modifications such as foams, finned surface, coated-nanoparticles, deposited sintered copper particles, and sprayed graphene oxide showed that octet lattice structures not only have the potential to enhance the heat transfer coefficient better but also delayed the critical heat flux (CHF) value. The CHF for the compared conventional features was typically obtained at 20-50 W/cm^2 whereas the range of 71-107 W/cm^2 was achieved for the investigated octet structures. Additively manufactured square-cell shaped porous fixture was reported to improve the boiling heat transfer coefficient from a plain surface by ~80% at low heat flux values ($10W/cm^2$) in a study by Elkholy et al. [138] without having significant impact on the critical heat flux. In this case, the porous lattice was manufactured in polymer via Fused Filament Fabrication (FFF).

Ho et al. [139] studied novel air-cooled heat exchangers with rhombi-octet unit cell lattice manufactured through SLM in AlSi10Mg (Fig. 2.11c). The improved fluid mixing by the presence of lattice structure resulted in enhanced heat transfer coefficient for porous heat exchanger as compared to conventional fin-tube heat exchangers. At same mass flow rate, the air-side heat transfer coefficient of lattice was more than twice the fin-tube heat exchanger and about ~45% higher when compared for same pumping power per unit depth (W/H). The lattices provided similar heat transfer coefficient relative to fin heat exchangers for lower pressure drop per unit width ($\Delta P/H$) but completely surpassed at higher values. It was therefore, recommended that in order to benefit from the lattices structure the heat exchanger should be operated at $\Delta P/H > 0.0275\ kPa/mm$. To estimate the competitiveness of lattice structures in terms of compactness relative to conventional fin-tube heat exchanger, it was observed that lattice structure could dissipate about 72.1 kW/m^3 volumetric heat flux at mass flow rate of 0.27 $kg\ /s$ which was about 60% higher than fin- tube heat exchangers due to higher packing density of rhombi-octet unit cells. Therefore, a significant amount of volume reduction can be achieved to obtain similar heat transfer as that of conventional heat exchangers when lattices are employed. Several other studies by Ho et al. [140,141] on lattices structure composed of rhombi-octet unit cell topology in rectangular block as well as circular insert configuration showed that these lattices provide significantly higher thermal performance as compared to open-cell metal foams, conventional pin-fin heat sinks and helical inserts. The effective thermal conductivity values for rhombi-octet unit cells having porosity of ~0.84-0.85 was measured to be about 5.5 times higher than stochastic aluminum metal foams samples having similar strut diameter – although this finding needs to be substantiated by some other studies (a caution to the readers). The thermal fluid-structure analysis was conducted on a lattice channel containing face-centered cubic unit cell with vertical struts (FCCZ) topology manufactured via. Binder Jetting from 17-4 PH material [142]. Figure 2.11d shows the test set-up used for experiments. Octet-truss lattices with different porosities manufactured through *DMLS* in AlSi10Mg were investigated by Chaudhari et al. [143]. Thorough characterization of samples was not conducted but deviation of ~3% in dimensions was reported between CAD models and printed samples. The transition of Darcy to non-Darcy regime was reported to occur at Reynold number (based on permeability) Re_K~7, but this value was obtained from the extrapolation method. The experimental studies were conducted for Re_K>40, the obtained values from which were extrapolated below to lower Reynolds number values. Numerical results for Re_K<40 was compared to these extrapolated values to obtain the transition Reynolds number. Such information of transition values for other lattices is still limited in literature and more comprehensive studies on identification of transitional limits through direct numerical simulations is required at this stage.

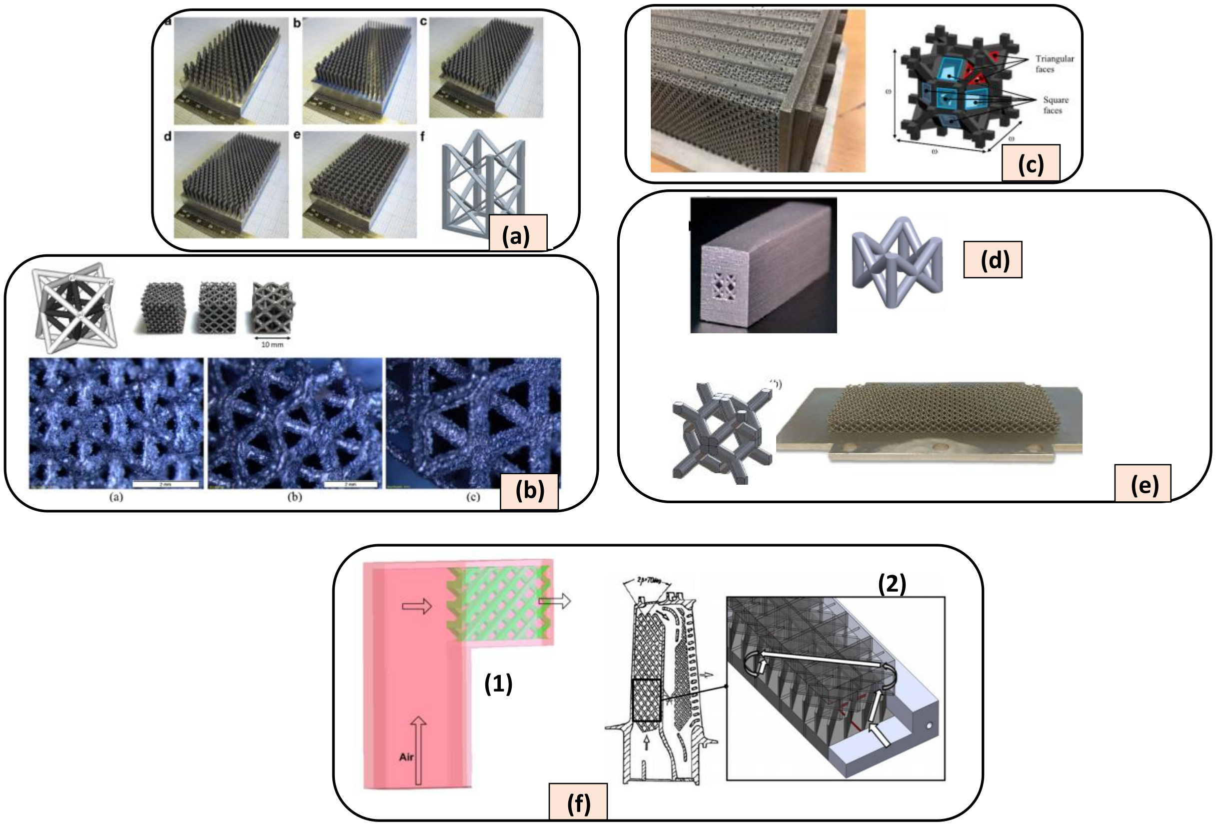

Figure 2.11 Lattice structures investigated for heat transfer experiments (a) heat sinks made by *SLM*[137], (b) octet lattices [116], (c) rhombi-octet heat exchanger[139], (d) FCCZ topology [142], (e) rhombic-dodecahedron [144], (f) lattice configurations for cooling turbine blades [145,146]

Broughton and Joshi [144] compared the performance of additively manufactured lattice of 0.865 porosity via *DMLS* from AlSi10Mg (Fig. 2.11e). The regular lattice provided 60% higher heat transfer coefficient at the cost of ~66% higher pressure drop penalty as compared to the stochastic metal foams. Liang et al. [147] investigated the effect of different strut shapes, viz. circular, rectangular and elliptical strut shapes of the face-centered cubic lattices of same porosity ~0.92 made from epoxy by *SLA* process, on endwall heat transfer and pressure drop. The circular strut shape was reported to have the lowest heat transfer and pressure drop, but highest thermal-hydraulic performance. The endwall heat transfer of single-cell thick configuration was three times the plane channel when FCC lattices were employed. Elliptical and rectangular strut yielded about ~27-31% and 25-26% higher heat transfer than the circular FCC due to better flow mixing and acceleration. Therefore, optimization of strut shapes of similar unit cell topologies can also improve the performance of the lattice heat exchangers.

Saha et al.[145] numerically investigated heat transfer and thermo-hydraulic performance (THP) of trailing edge featuring 2-inlet and 4-inlet channel lattice as shown in Fig. 2.11f(1). Heat transfer enhancement of 24% to 55% higher as compared to pin-fin configuration was provided by 2-inlet channel lattice. The THP of 2-inlet channel was comparable or higher than the pin-fins for the investigated Reynolds number. Lattice formed by crossed 45 degree rib-type structures (Fig. 2.11f(2)) was experimentally investigated by Carcasci et al.[146] for heat transfer distribution and pressure drop characteristics, where the lattice spanned from mid-chord region to the trailing edge. Higher heat transfer by employing Kagome as compared to the pin-fins in the trailing edge cooling configuration was also reported by Shen et al.[148]. These lattices are claimed to be potential alternatives to the conventional pin-fin and rib-turbulator configurations because the lattices can provide higher heat transfer, comparable THP and better structural integrity. Complex lattice topologies manufactured via additive manufacturing can be investigated for usage in turbine cooling mechanisms.

Jafari et al. [121] investigated the phase change heat transfer characteristics of additively manufactured wick structure composed of octahedral unit cells in stainless steel via *SLM* for a flat heat pipe. When compared to some conventional wicks (grooved, sintered and screen meshes), the additively manufactured wick structure yielded the best thermal-performance enhancement which was attributed to increased evaporating meniscus density due to attached sintered powder material, high permeability due to large pores, and improved thermal contact between the wick and the heat pipe wall because the wall and wick were manufactured as an integrated structure in monolithic build. An additively manufactured titanium alloy oscillating heat pipe having four inter-connected layers of mini-channels was manufactured and investigated by Ibrahim et al. [120] for various orientations and working fluids. The partially sintered attached particles to the finished surfaces were expected to improve the capillary pumping ability of heat pipe and promote boiling heat transfer during start-up which led to the reduction in start-up power requirements. It is interesting to note that the surface roughness, which is inherent to surface finish of products made by the metal additive manufacturing technologies, has significant influence on the thermal-hydraulic characteristics of the structures. In two-phase flows, their role becomes even more critical where they can act as nucleation sites (boiling) or determine the capillary forces by secondary wicking behavior (heat pipes).

From the review of the above studies, it is clear that the regular lattices have the potential of better thermal performance as compared to the stochastic metal foams but the achievable morphological parameters such as porosity and unit cell length are still very limited due to AM process constraints and the resultant defects. *DMLS, SLM, EBM* and Binder Jetting techniques are mostly used for manufacturing the metal lattices, with *DMLS* and *SLM* being the most common. *DMLS* and *SLM* could process AlSi10Mg alloy material which is good from the perspective of heat exchange as it exhibits higher solid-phase thermal conductivity. Binder Jetting, on the other hand, employs stainless steel and cobalt-chrome which have lower thermal conductivity and higher mass as compared to aluminum of the same volume. While copper is the material which has much higher thermal conductivity than aluminum, the manufacturing and investigation of copper lattices is still relatively unexplored[149]. The processing of copper alloys by *SLM* encounters difficulty because of low laser absorption rate and high thermal conductivity [150]. Commercially available technologies for production of metal lattices are few and the choice for printing metal material is also narrow currently.

2.5.2 Flow-field visualization and heat transfer mechanisms

This section describes the flow dynamics and heat transfer mechanisms in some of the common lattice structures mentioned in the previous sections. In single unit cell thick sandwich type configurations, the endwall characteristics are predominantly determined by the near-wall flow dynamics. In strut-based topologies, the flow undergoes modifications either around the struts, junctions (where the struts meet), or at the vertices (contact point of struts with the endwall).

The formation of horseshoe vortices around the vertices and arch-shaped vortices in the wake leading to separation and recirculation followed by flow reattachment were dominant flow features in the tetrahedral unit cell configurations reported by Kim et al. [66,122], also shown in Fig. 2.12a. The net conjugate convective heat transfer from the struts could be up to 50% of the total heat if the high conductivity material like aluminum was used. The formation of transverse vortices near the vertices of X-type core lattices were reported by Yan et al. [102], with flow direction OB shown in Fig. 2.7a, which entrained the fluid from the upstream vertex to impinge onto the downstream vertex and produced longitudinal vortices (Fig. 2.12b). The shearing of these vortex structures yielded high heat transfer. The detailed mechanism of secondary vortices for flow direction OA was revealed in further work [127] where complex primary spiral flow was observed along with secondary tangential flows on the periphery of X-cores and counter-rotating vortex pairs climbing up the downstream strut faces (Fig. 2.12c). In strut-based lattices, the upstream strut faces are generally characterized by higher heat transfer coefficient values as compared to the downstream faces where the flow separation is encountered. Horseshoe formation at the vertices and counter-rotating pair vortex structure formation behind the vertices were also observed by Liang et al. [147] for FCC topology. The formation and location of the vortices is critical in determining the local heat transfer of sandwich panels.

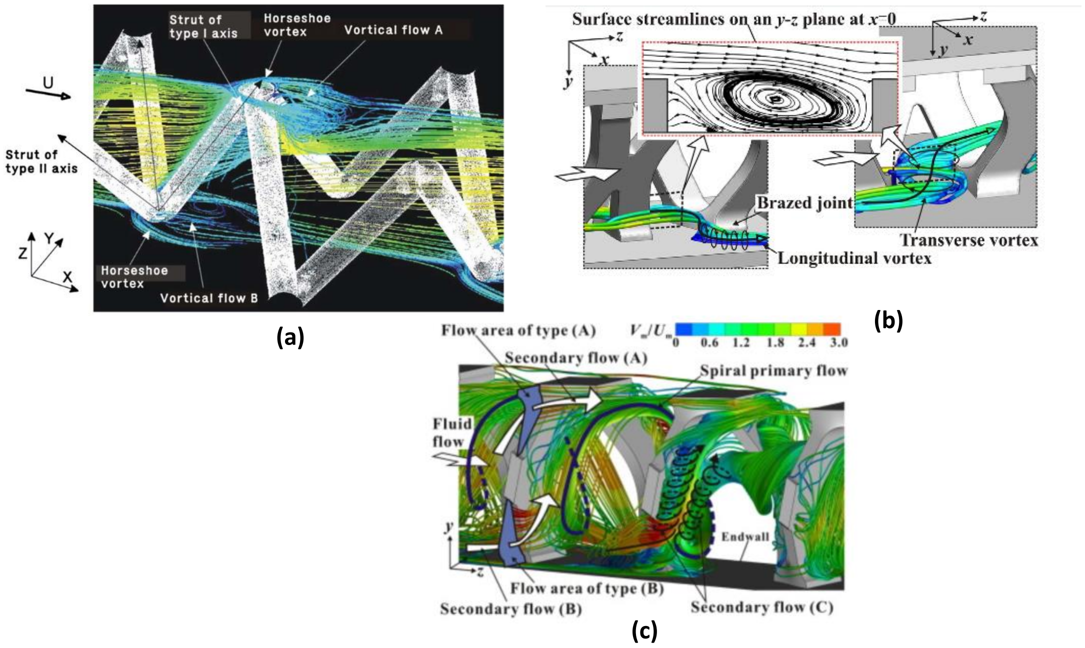

(a)

(b)

(c)

Figure 2.12 Flow dynamics in (a) tetrahedral unit cell[122], (b) X-type lattice (flow direction OB)[102], (c) X-type lattice (flow direction OA) [127]

The heat transfer in bulk porous media such as metal foams or regular periodic lattices has major contribution from the interfacial convective heat transfer. In these studies, the consideration of local thermal equilibrium (LTE) or local thermal non-equilibrium (LTNE) validity is important for accuracy of thermal transport solutions. The LTNE assumption provides better solution when large differences in solid- and fluid- thermal conductivities exist [71]. Therefore, a major mechanism for heat transfer in bulk porous structures are interfacial convective heat transport guided by the local thermal non-equilibrium boundary conditions. Thermal dispersion, too, can be very significant in cases where the solid- and liquid- conductivity difference is not very high and at very high velocities. Broughton and Joshi [144] compared the transport in stochastic metal foams and rhombi-dodecahedron and observed the flow to be relatively more organized. The difference in obtained Nusselt number for stochastic and regular foam was diminishing at higher velocity values which was attributed to improved thermal dispersion in stochastic metal foams. Larger recirculation zones were observed downstream of the ligaments, a typical phenomenon observed in several other topologies. Impingement effect of the incoming flow on the struts is instrumental in determining the local heat transfer distribution on the struts, especially when the number of repeating units in the streamwise direction are small [151]. Apart from the heat transfer coefficient value enhancement mechanisms, the total surface area-to-volume ratio also plays significant role in determining the net heat dissipation from bulk foams.

The underlying mechanisms for heat pipes and pool boiling with mounted lattice features has already been elaborated in existing literature. An important characteristic that the additive manufacturing lend to these lattices is the surface roughness. While the role of surface roughness is reported to be positive on phase-change heat transfer in the limited pertinent literature, still a thorough investigation of its role is needed.

2.5.3 Defects in additively manufactured lattices

One of the most common defects observed in metal lattices manufactured by *SLM* processes is the surface roughness due to presence of partially sintered metal on the struts as shown in Fig. 2.11b. The un-sintered material generally results from lack of fusion in laser power bed processes. In a recent study, Dressler et al. [152] showed the deviations of truss geometry manufactured through *DMLS* (stainless steel alloy) technique from the idealized CAD model as shown in Fig. 2.13. The manufactured lattice had non-circular and heterogenous struts with extra material in some locations and reduced material in other locations. The orientation of struts with respect to printing bed was found to be critical for product quality where the defects tend to increase with decreasing inclination of the strut with respect to the printing bed. The horizontal struts in the study by Dressler and group were of inferior quality with weak mechanical properties. Moreover, the loose powder is generally the support structure for lattices printed through DMLS which could cause the defects like dripping from above-lying horizontal struts. The sticking of non-sintered material to the struts in continuous form may even lead to tunneling porosity (Fig. 2.13b).

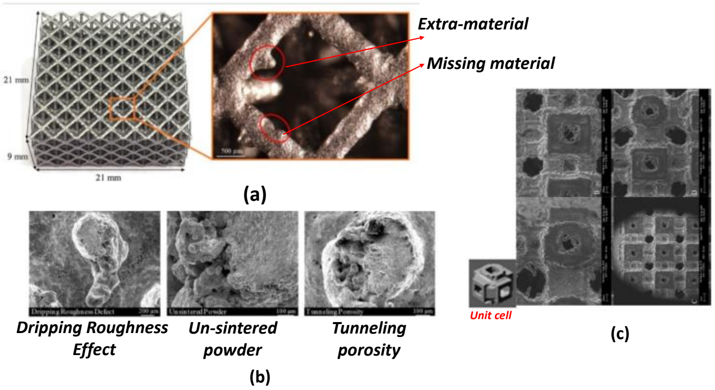

Figure 2.13 Defects in additively manufactured lattices [152,153]

While these defects are reported to have significantly impacted the mechanical behavior of lattices, the heat transfer is also expected to be influenced as a result – a topic not much explored for lattices. The surface area densities get impacted with such roughness length scales as well. The addition and subtraction of unwanted material alters the final porosity values. From the perspective of enhanced heat transfer, surface roughness is usually a desired quality. However, the roughness length scales when compared to the fiber- and pore-diameters may sometimes be comparable, which can essentially result in pore blockage or increase in flow resistance, leading to reduction in the thermal hydraulic performance. Figure 2.13c shows the microstructure of pores of lattice manufactured via *SLM* (titanium alloy) [153]. The fabricated lattice has significant surface protrusions in the pores causing the blockage. The manufactured pore size was ~0.7 mm as opposed to ~1 mm of the CAD design. Figure 2.14 shows the CT scan of the reconstructed image of tetrahedron unit cell manufactured through *SLM* with Ti6AlV4 as the solid-phase material [154]. The accumulation of unwanted material around the struts and nodes is apparent. The defects become more pronounced for decreasing unit cell size. The wall thickness deviation from the CAD model are presented in Fig. 2.14c. While there is an effort to study the influence of these deviations on the mechanical properties, there effect on the flow and thermal transport is a subject of study too. The products manufactured by Binder Jetting also suffer from the challenges of producing fully dense parts, especially without infiltrations. For a detailed review on the surface, geometrical and porosity defects in different additive manufacturing processes, the readers are referred to [155]. State-of-the-art AM technologies employed for fabricating metal foams need significant advancement to achieve smaller fiber and pore diameters, with improved surface finish and reduced defects.

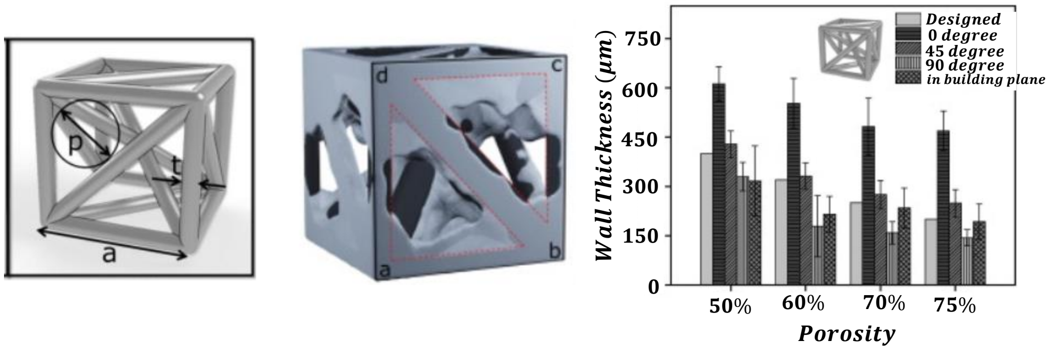

(a) (b) (c)

Figure 2.14 (a) Tetrahedron unit cell topology, (b) Reconstructed CT image at porosity 0.75, (c) Deviation of manufactured wall thickness to original CAD design for different porosities[154]

2.5.4 Morphological parameters of additively manufactured lattices

Table 2.3 provides the statistics of unit cell size, strut diameter and porosity values of different AM lattice topologies. The unit cell sizes of ~2 to 27 mm is presented here. Real benefits in heat transfer are realized at smaller length scales. Low unit cell sizes with high porosities offering high surface area to volume ratio while incurring permissible pressure drops is desirable, as in the case of stochastic metal foams. Although the unit cell size as low as 2 mm with strut diameter of 0.31mm can be printed with fair accuracy but the associated defects are also apparent (Fig.2. 11b). Manufacturing defect-free lattices at such length scales or with more control on the surface finish is still a challenge. Moreover, the porosity corresponding to the above-mentioned dimensions for octet topology was ~0.7. Achieving higher porosity lattices with the same unit cell size and minimal defects is difficult at this stage. The manufacturing of complex trusses like that of octet by Binder Jetting process from stainless steel (with bronze infiltration) requires a minimum strut dimension of 0.8 mm for successful building and satisfactory quality, based on the recommendations of users with M-Flex AM printer. There is a restriction on the corresponding permissible unit cell size as well which limits attainment of high porosity samples. Moreover, the circular struts appear to be completely heterogeneous and non-circular after printing in Fig. 2.13 and 2.14b, due to which the freedom to successfully make struts of different cross-sections with desired quality becomes questionable too.

Table 2.3 Process, material, and unit cell properties of different topologies for SLM and DMLS processes

Reference	**Material**	**Process**	**Topology**	**Unit cell size (mm)**	**Strut Diameter (mm)**	**Porosity**
[116]	AlSi10Mg	SLM	Octet	2,3,5	0.31 – 0.85	0.7
[139]	AlSi10Mg	SLM	Rhombi-octet	7, 14	--	0.85
[143]	AlSi10Mg	DMLS	Octet	14-27	--	0.70-0.91
[144]	AlSi10Mg	DMLS	Rhombic-dodecahedron	4.65	0.548	0.865

2.5.5 Recent progress and current state-of-the-art in lattice AM

The previous section highlights the geometrical inhibitions in the realization of small dimensions for manufacturing highly porous lattice structures for compact and efficient heat exchangers. However, there is continuous effort to develop different materials and test the manufacturability of smaller length scales. Micro-lattices with unit cell size of as small as ~1.25 mm and fiber diameter of ~0.2 mm with *BCC* topology was manufactured via. *SLM* in stainless steel by Gümrük et al. [156]. *SLM* technology was successfully used by Tsopanos et al. [157] to fabricate micro-lattices with unit cell size of ~2.5 mm and strut diameter of ~0.2 mm. Yu et al.[158] investigated micro-lattices with strut diameter of ~0.4 mm with six different unit cells manufactured by *SLM* in AlSi10Mg. Unit cell dimensions of 1- 4 mm and strut diameter of 0.2-0.5 mm are realizable for metal lattices via. *SLM*. However, most of these lattices are subjected to mechanical testing and process parameter effect investigations. Comprehensive convective flow and thermal transport studies are relatively scarce. Plessis et al. [159] successfully produced diamond topology lattice with unit cell size of 0.6-1.2 mm and corresponding strut diameter of 0.1-0.15 mm in Ti6Al4V via laser-based powder bed fusion (*LPBF*) system. Severe irregularities such as strut roughness was observed in μCT scan of lattices. The measured porosity was ~0.63 and ~0.90 for the smallest (0.6 mm) and largest (1.2 mm) unit cell size, respectively, as compared to the designed CAD model porosity of ~0.80. Ma et al. [150] recently fabricated the Cu-Cr-Zr copper alloy lattice successfully for the first time through *SLM*. The sample showed deviation of ±300 μm from the CAD model and *SLM* was claimed to be capable of processing the tested alloy material. The accumulation of non-sintered metal accumulation on the struts and nodes was observed to be stronger than that on titanium and aluminum alloys because of better thermal conductivity of copper. Kenel et al. [160] developed a non-beam approach to additively manufacture micro-lattice from CoCrFeNi with ~99.6% relative density and strut diameter of as low as ~0.1 m. Octet unit cell topology nano-lattice having unit cell size of ~ 2µm and strut diameter of ~300-400 nm was fabricated from hybrid organic-inorganic nickel containing materials via lithography-based process by Vyatskikh et al. [161]. The fabricated unit cell is shown in Fig. 2.15. The possibilities of additively manufacturing the rare earth metal (neodymium) alloys such as NdFeB is also being explored [162,163].

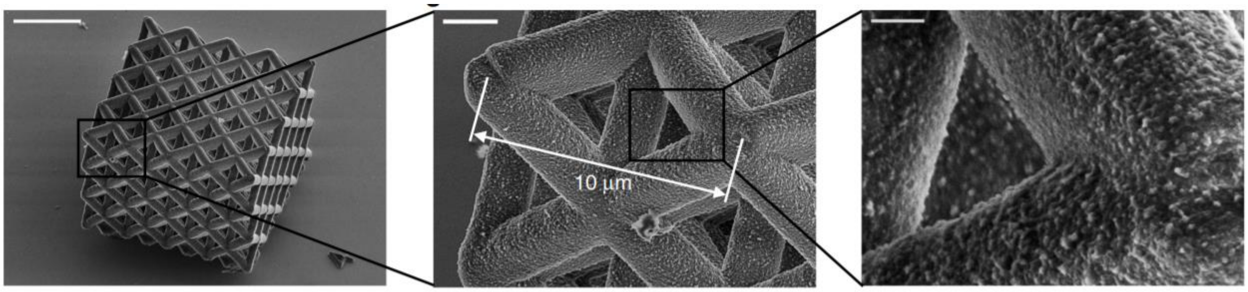

Figure 2.15 Nanolattices with octet unit cell topology [161]

With increasing emphasis on the development of metal-based *AM* technologies and their demand in the thermal management sector, a significant surge in the fundamental studies on *AM* process, application-based studies of employing additively manufactured lattices in micro-scale cooling segment, is expected.

2.6 Conclusions

A comprehensive review on the state-of-the-art metal-based additive manufacturing technologies used in lattice printing is presented. The conventional and recent additively manufacturing technologies are discussed thoroughly along with the flow and thermal characteristics of lattices fabricated via. these techniques. This review is aimed towards addressing some current pressing issues in AM technology for metal lattice printing from the perspective of a heat exchanger designer, and the promise of AM in future advancements of heat exchangers. The review attempts to answer following current issues on this topic, and a summary is provided below.

(1) *What are the advantages and limitations of the regular lattices with respect to extensively investigated traditional metal foams?*

Copper wire meshes at optimal porosity of ~0.75 are shown to have better thermal performance as compared to stochastic metal foams having porosity around ~0.9. Very high surface area densities for lattices obtained from metal-wire approach could be obtained but similar values are easily achievable for stochastic metal foams too and at much higher porosities. The cost effectiveness and relative ease in fabrication with more control on the morphological parameters still make the wire meshes very desirable in variety of thermal applications such as solar heaters, surface enhancements in boiling heat transfer, wick structures in heat pipes, etc.

Additively manufactured regular lattices are shown to have better thermal characteristics than stochastic foams. At similar porosities, customized complex unit-cell topologies can provide significant heat transfer enhancement relative to stochastic metal foams. The flow losses in additively manufactured lattices are dependent on the unit cell topology, which at times could be significantly higher than the stochastic metal foams. The major limitation of regular lattice printing is in realizing complex topologies having dimensions comparable to traditional stochastic metal foams with high thermally conducting material while ensuring minimal deviation from the original intended geometry.

(2) *Unit-cell and fiber- length-scales achieved through AM in contrast with traditional stochastic open-cell metal foams?*

The unit cell sizes of ~1.5 mm, comparable to conventional open-cell metal foams, have been achieved with strut dimensions as low as ~0.2 mm, but with non-ignorable defects. There is an ongoing effort to manufacture much smaller length scales. Conventional heat transfer studies in lattices having morphological parameters between 1-5 mm are promising but are relatively few in number. With the development of new technologies achieving lower dimensional scales and new printing materials, it is still an open question if these can qualify for efficient heat exchangers as yet because most of these studies are dedicated to investigating the mechanical/structural properties of lattices. The maximum porosities of AM lattices (typically at maximum of < 0.90) is lower than the conventional foams (~0.97). Further, the achievable length depends on the unit cell topology and the material as well.

(3) *Can additively manufactured lattices replace the traditional stochastic metal foams in compact heat exchangers in foreseeable future*?

Regular lattices printed additively have the potential to substitute the traditional metal foams, as found through experiments and some numerical simulations. The additively manufactured lattices may result in significantly higher interstitial heat transfer coefficient as compared to stochastic metal foams. Further, the design freedom allows different porosities through which higher effective thermal conductivity can be achieved. More research can be carried out in the development of novel unit cell topologies which have multi-functional properties in terms of higher effective thermal conductivity, interstitial heat transfer coefficient and load bearing capabilities.

Due to higher packaging density of customized unit cell topologies, about 60% higher heat transfer for lattice-based tube heat exchanger has already been reported relative to fin-tube heat exchangers having same volume at mass flow rate of ~0.27 kg/s . Thus, a more compact heat exchanger can be designed with lattices if the heat dissipation values, and mass flow rates are the constraints.

Phase change heat transfer can also leverage the benefits of additive manufacturing. The freedom of designing customized shapes can help us obtain lattice structures which could delay the CHF of pool boiling as compared to already existing conventional surface enhancements. Moreover homogeneous, mechanically strong, and structures with desirable permeability can be used as wicks in heat pipes as well as in transpiration cooling concepts. An important aspect that still requires a systematic investigation is the role of inherent surface roughness, which is generated while manufacturing, on the thermal and hydraulic performance.

The open-cell metal foams are lightweight, manufactured in highly conducting materials such as Copper and Aluminum and could be as thin as ~2 mm while having surface area density of ~10,000 m^2/m^3, which is ideal for compact heat exchangers. Regular lattices still need to prove their efficacy when printed at such small length scales, while still offering a controlled topology and inherent roughness, with high structural integrity and high thermal conductivity solid phase. The flow and thermal transport research on regular lattices, although scarce, shows promise and indicates that with the rapidly evolving AM technology, the design and development of lattice-assisted heat exchangers would also change significantly, resulting in many concepts with superior thermal hydraulic performance.

REFERENCES

[1] P.S. Liu, G.F. Chen, Porous Materials: Processing and Applications, 2014. https://doi.org/10.1016/C2012-0-03669-1.

[2] A.A.M. Oliveira, M. Kaviany, Nonequilibrium in the transport of heat and reactants in combustion in porous media, Prog. Energy Combust. Sci. (2001). https://doi.org/10.1016/S0360-1285(00)00030-7.

[3] M. Bazmi, S.H. Hashemabadi, M. Bayat, Extrudate Trilobe Catalysts and Loading Effects on Pressure Drop and Dynamic Liquid Holdup in Porous Media of Trickle Bed Reactors, Transp. Porous Media. (2013). https://doi.org/10.1007/s11242-013-0199-x.

[4] D.P. Jaisi, N.B. Saleh, R.E. Blake, M. Elimelech, Transport of single-walled carbon nanotubes in porous media: Filtration mechanisms and reversibility, Environ. Sci. Technol. (2008). https://doi.org/10.1021/es801641v.

[5] T.K. Sen, K.C. Khilar, Review on subsurface colloids and colloid-associated contaminant transport in saturated porous media, Adv. Colloid Interface Sci. (2006). https://doi.org/10.1016/j.cis.2005.09.001.

[6] A.M. Bayomy, M.Z. Saghir, T. Yousefi, Electronic cooling using water flow in aluminum metal foam heat sink: Experimental and numerical approach, Int. J. Therm. Sci. (2016). https://doi.org/10.1016/j.ijthermalsci.2016.06.007.

[7] H.J. Xu, Z.B. Xing, F.Q. Wang, Z.M. Cheng, Review on heat conduction, heat convection, thermal radiation and phase change heat transfer of nanofluids in porous media: Fundamentals and applications, Chem. Eng. Sci. (2019). https://doi.org/10.1016/j.ces.2018.09.045.

[8] A. Bhattacharya, R.L. Mahajan, Finned metal foam heat sinks for electronics cooling in forced convection, J. Electron. Packag. Trans. ASME. (2002). https://doi.org/10.1115/1.1464877.

[9] A. Bhattacharya, R.L. Mahajan, Metal foam and finned metal foam heat sinks for electronics cooling in buoyancy-induced convection, J. Electron. Packag. Trans. ASME. (2006). https://doi.org/10.1115/1.2229225.

[10] R. Rachedi, S. Chikh, Enhancement of electronic cooling by insertion of foam materials, Heat Mass Transf. Und Stoffuebertragung. (2001). https://doi.org/10.1007/s002310100192.

[11] C.Y. Zhao, T.J. Lu, Analysis of microchannel heat sinks for electronics cooling, Int. J. Heat Mass Transf. (2002). https://doi.org/10.1016/S0017-9310(02)00180-1.

[12] K. Boomsma, D. Poulikakos, F. Zwick, Metal foams as compact high performance heat exchangers, Mech. Mater. (2003). https://doi.org/10.1016/j.mechmat.2003.02.001.

[13] W. Fuqiang, M. Lanxin, C. Ziming, T. Jianyu, H. Xing, L. Linhua, Radiative heat transfer in solar thermochemical particle reactor: A comprehensive review, Renew. Sustain. Energy Rev. (2017). https://doi.org/10.1016/j.rser.2017.01.165.

[14] S. Suter, S. Haussener, Morphology engineering of porous media for enhanced solar fuel and power production, JOM. (2013). https://doi.org/10.1007/s11837-013-0787-9.

[15] H.I. Villafán-Vidales, S. Abanades, C. Caliot, H. Romero-Paredes, Heat transfer simulation in a thermochemical solar reactor based on a volumetric porous receiver, Appl. Therm. Eng. (2011). https://doi.org/10.1016/j.applthermaleng.2011.06.022.

[16] R. Vadi, K. Sepanloo, An improved porous media model for nuclear reactor analysis, Nucl. Sci. Tech. (2016). https://doi.org/10.1007/s41365-016-0016-7.

[17] Y.A. Hassan, E.E. Dominguez-Ontiveros, Flow visualization in a pebble bed reactor experiment using PIV and refractive index matching techniques, Nucl. Eng. Des. (2008). https://doi.org/10.1016/j.nucengdes.2008.01.027.

[18] S. Wanphen, K. Nagano, Experimental study of the performance of porous materials to moderate the roof surface temperature by its evaporative cooling effect, Build. Environ. (2009). https://doi.org/10.1016/j.buildenv.2008.03.012.

[19] S. Rashidi, J.A. Esfahani, N. Karimi, Porous materials in building energy technologies—A review of the applications, modelling and experiments, Renew. Sustain. Energy Rev. (2018). https://doi.org/10.1016/j.rser.2018.03.092.

[20] W. Lu, C.Y. Zhao, S.A. Tassou, Thermal analysis on metal-foam filled heat exchangers. Part I: Metal-foam filled pipes, Int. J. Heat Mass Transf. (2006). https://doi.org/10.1016/j.ijheatmasstransfer.2005.12.012.

[21] C.Y. Zhao, W. Lu, S.A. Tassou, Thermal analysis on metal-foam filled heat exchangers. Part II: Tube heat exchangers, Int. J. Heat Mass Transf. (2006). https://doi.org/10.1016/j.ijheatmasstransfer.2005.12.014.

[22] S. Mahjoob, K. Vafai, A synthesis of fluid and thermal transport models for metal foam heat exchangers, Int. J. Heat Mass Transf. (2008). https://doi.org/10.1016/j.ijheatmasstransfer.2007.12.012.

[23] Z. Liu, Y. Yao, H. Wu, Numerical modeling for solid-liquid phase change phenomena in porous media: Shell-and-tube type latent heat thermal energy storage, Appl. Energy. (2013). https://doi.org/10.1016/j.apenergy.2013.02.022.

[24] Y. Xu, Q. Ren, Z.J. Zheng, Y.L. He, Evaluation and optimization of melting performance for a latent heat thermal energy storage unit partially filled with porous media, Appl. Energy. (2017). https://doi.org/10.1016/j.apenergy.2017.02.019.

[25] J. Wang, P. Rubini, Q. Qin, Application of a porous media model for the acoustic damping of perforated plate absorbers, Appl. Acoust. (2017). https://doi.org/10.1016/j.apacoust.2017.07.003.

[26] I.S. Saguy, A. Marabi, R. Wallach, New approach to model rehydration of dry food particulates utilizing principles of liquid transport in porous media, Trends Food Sci. Technol. (2005). https://doi.org/10.1016/j.tifs.2005.07.006.

[27] A.K. Datta, Porous media approaches to studying simultaneous heat and mass transfer in food processes. I: Problem formulations, J. Food Eng. (2007). https://doi.org/10.1016/j.jfoodeng.2006.05.013.

[28] A.K. Datta, Porous media approaches to studying simultaneous heat and mass transfer in food processes. II: Property data and representative results, J. Food Eng. (2007). https://doi.org/10.1016/j.jfoodeng.2006.05.012.

[29] R. Brooks, A. Corey, Hydraulic properties of porous media, Hydrol. Pap. Color. State Univ. (1964).

[30] M.T. van Genuchten, P.J. Wierenga, Mass Transfer Studies in Sorbing Porous Media I. Analytical Solutions, Soil Sci. Soc. Am. J. (1976). https://doi.org/10.2136/sssaj1976.03615995004000040011x.

[31] W. Woodside, J.H. Messmer, Thermal conductivity of porous media. I. Unconsolidated sands, J. Appl. Phys. (1961). https://doi.org/10.1063/1.1728419.

[32] G.G. Bernard, L.W. Holm, Effect of Foam on Permeability of Porous Media to Gas, Soc. Pet. Eng. J. (1964). https://doi.org/10.2118/983-pa.

[33] S.S. Marsden, S.A. Khan, The Flow of Foam Through Short Porous Media And Apparent Viscosity Measurements, Soc. Pet. Eng. J. (1966). https://doi.org/10.2118/1319-pa.

[34] D.A. Nield, A. V Kuznetsov, An historical and topical note on convection in porous media, J. Heat Transfer. (2013). https://doi.org/10.1115/1.4023567.

[35] S. Hadadpour, M. Paul, H. Oumeraci, Numerical Investigation of Wave Attenuation by Rigid Vegetation Based on a Porous Media Approach, J. Coast. Res. (2019). https://doi.org/10.2112/si92-011.1.

[36] C.E. Oldham, J.J. Sturman, The effect of emergent vegetation on convective flushing in shallow wetlands: Scaling and experiments, Limnol. Oceanogr. (2001). https://doi.org/10.4319/lo.2001.46.6.1486.

[37] A.M. Morega, A. Bejan, S.W. Lee, Free stream cooling of a stack of parallel plates, Int. J. Heat Mass Transf. (1995). https://doi.org/10.1016/0017-9310(94)00123-D.

[38] K. Hooman, H. Gurgenci, Porous Medium Modeling of Air-Cooled Condensers, Transp. Porous Media. (2010). https://doi.org/10.1007/s11242-009-9497-8.

[39] S. Whitaker, Flow in porous media I: A theoretical derivation of Darcy’s law, Transp. Porous Media. (1986). https://doi.org/10.1007/BF01036523.

[40] S. Whitaker, Diffusion and dispersion in porous media, AIChE J. (1967). https://doi.org/10.1002/aic.690130308.

[41] S. Whitaker, Flow in porous media II: The governing equations for immiscible, two-phase flow, Transp. Porous Media. (1986). https://doi.org/10.1007/BF00714688.

[42] J.A. Ochoa-Tapia, S. Whitaker, Momentum transfer at the boundary between a porous medium and a homogeneous fluid-I. Theoretical development, Int. J. Heat Mass Transf. (1995). https://doi.org/10.1016/0017-9310(94)00346-W.

[43] O. V Trevisan, A. Bejan, Natural convection with combined heat and mass transfer buoyancy effects in a porous medium, Int. J. Heat Mass Transf. (1985). https://doi.org/10.1016/0017-9310(85)90261-3.

[44] D. a Nield, A. Bejan, Convection in Porous Media Third Edition, 2006.

[45] M. Kaviany, Principles of Heat Transfer in Porous Media, Mech. Eng. Ser. (1995). https://doi.org/10.1007/978-1-4612-4254-3.

[46] K. Vafai, S.J. Kim, On the limitations of the Brinkman-Forchheimer-extended Darcy equation, Int. J. Heat Fluid Flow. (1995). https://doi.org/10.1016/0142-727X(94)00002-T.

[47] K. Vafai, C.L. Tien, Boundary and inertia effects on flow and heat transfer in porous media, Int. J. Heat Mass Transf. (1981). https://doi.org/10.1016/0017-9310(81)90027-2.

[48] A. Amiri, K. Vafai, Analysis of dispersion effects and non-thermal equilibrium, non-Darcian, variable porosity incompressible flow through porous media, Int. J. Heat Mass Transf. (1994). https://doi.org/10.1016/0017-9310(94)90219-4.

[49] K. Vafai, Convective flow and heat transfer in variable-porosity media, J. Fluid Mech. (1984). https://doi.org/10.1017/S002211208400207X.

[50] A.R.A. Khaled, K. Vafai, Heat transfer enhancement through control of thermal dispersion effects, Int. J. Heat Mass Transf. (2005). https://doi.org/10.1016/j.ijheatmasstransfer.2004.12.035.

[51] M.F. Ashby, The properties of foams and lattices, Philos. Trans. R. Soc. A Math. Phys. Eng. Sci. (2006). https://doi.org/10.1098/rsta.2005.1678.

[52] D.J. Brink, M.E. Lee, Confined blue iridescence by a diffracting microstructure: an optical investigation of the Cynandra opis butterfly, Appl. Opt. (1999). https://doi.org/10.1364/ao.38.005282.

[53] J. Hai, F. Chen, J. Su, F. Xu, B. Wang, Porous Wood Members-Based Amplified Colorimetric Sensor for Hg2+ Detection through Hg2+-Triggered Methylene Blue Reduction Reactions, Anal. Chem. (2018). https://doi.org/10.1021/acs.analchem.8b00710.

[54] F. López Jiménez, N. Triantafyllidis, Buckling of rectangular and hexagonal honeycomb under combined axial compression and transverse shear, Int. J. Solids Struct. (2013). https://doi.org/10.1016/j.ijsolstr.2013.08.001.

[55] Z. Xie, T. Ikeda, Y. Okuda, H. Nakajima, Sound absorption characteristics of lotus-type porous copper fabricated by unidirectional solidification, Mater. Sci. Eng. A. (2004). https://doi.org/10.1016/j.msea.2004.07.058.

[56] K.C. Leong, L.W. Jin, Characteristics of oscillating flow through a channel filled with open-cell metal foam, Int. J. Heat Fluid Flow. (2006). https://doi.org/10.1016/j.ijheatfluidflow.2005.05.004.

[57] S. Mancin, C. Zilio, A. Diani, L. Rossetto, Air forced convection through metal foams: Experimental results and modeling, Int. J. Heat Mass Transf. (2013). https://doi.org/10.1016/j.ijheatmasstransfer.2013.02.050.

[58] Y. Mu, G. Yao, L. Liang, H. Luo, G. Zu, Deformation mechanisms of closed-cell aluminum foam in compression, Scr. Mater. (2010). https://doi.org/10.1016/j.scriptamat.2010.05.041.

[59] L. Shi, Y. Shi, S. Zhuo, C. Zhang, Y. Aldrees, S. Aleid, P. Wang, Multi-functional 3D honeycomb ceramic plate for clean water production by heterogeneous photo-Fenton reaction and solar-driven water evaporation, Nano Energy. (2019). https://doi.org/10.1016/j.nanoen.2019.03.039.

[60] S. Yamamura, H. Shiota, K. Murakami, H. Nakajima, Evaluation of porosity in porous copper fabricated by unidirectional solidification under pressurized hydrogen, Mater. Sci. Eng. A. (2001). https://doi.org/10.1016/S0921-5093(01)01263-1.

[61] C.S.Y. Jee, N. Özgüven, Z.X. Guo, J.R.G. Evans, Preparation of high porosity metal foams, Metall. Mater. Trans. B Process Metall. Mater. Process. Sci. (2000). https://doi.org/10.1007/s11663-000-0021-3.

[62] B.P. Neville, A. Rabiei, Composite metal foams processed through powder metallurgy, Mater. Des. (2008). https://doi.org/10.1016/j.matdes.2007.01.026.

[63] B. Ozmat, B. Leyda, B. Benson, Thermal applications of open-cell metal foams, in: Mater. Manuf. Process., 2004. https://doi.org/10.1081/AMP-200030568.

[64] C.Y. Zhao, Review on thermal transport in high porosity cellular metal foams with open cells, Int. J. Heat Mass Transf. (2012). https://doi.org/10.1016/j.ijheatmasstransfer.2012.03.017.

[65] P. Ranut, On the effective thermal conductivity of aluminum metal foams: Review and improvement of the available empirical and analytical models, Appl. Therm. Eng. (2016). https://doi.org/10.1016/j.applthermaleng.2015.09.094.

[66] T. Kim, H.P. Hodson, T.J. Lu, Fluid-flow and endwall heat-transfer characteristics of an ultralight lattice-frame material, Int. J. Heat Mass Transf. (2004). https://doi.org/10.1016/j.ijheatmasstransfer.2003.10.012.

[67] J. Banhart, Manufacturing routes for metallic foams, JOM. (2000). https://doi.org/10.1007/s11837-000-0062-8.

[68] J. Banhart, Manufacture, characterisation and application of cellular metals and metal foams, Prog. Mater. Sci. (2001). https://doi.org/10.1016/S0079-6425(00)00002-5.

[69] C. Moon, D. Kim, G. Bamorovat Abadi, S.Y. Yoon, K.C. Kim, Effect of ligament hollowness on heat transfer characteristics of open-cell metal foam, Int. J. Heat Mass Transf. (2016). https://doi.org/10.1016/j.ijheatmasstransfer.2016.06.068.

[70] J.J. Hwang, G.J. Hwang, R.H. Yeh, C.H. Chao, Measurement of interstitial convective heat transfer and frictional drag for flow across metal foams, J. Heat Transfer. (2002). https://doi.org/10.1115/1.1416690.

[71] V. V Calmidi, R.L. Mahajan, Forced convection in high porosity metal foams, J. Heat Transfer. (2000). https://doi.org/10.1115/1.1287793.

[72] S.Y. Kim, B.H. Kang, J.H. Kim, Forced convection from aluminum foam materials in an asymmetrically heated channel, Int. J. Heat Mass Transf. (2001). https://doi.org/10.1016/S0017-9310(00)00187-3.

[73] K. Boomsma, D. Poulikakos, The effects of compression and pore size variations on the liquid flow characteristics in metal foams, J. Fluids Eng. Trans. ASME. (2002). https://doi.org/10.1115/1.1429637.

[74] L. Giani, G. Groppi, E. Tronconi, Mass-transfer characterization of metallic foams as supports for structured catalysts, Ind. Eng. Chem. Res. (2005). https://doi.org/10.1021/ie0490886.

[75] S. Mancin, C. Zilio, A. Cavallini, L. Rossetto, Heat transfer during air flow in aluminum foams, Int. J. Heat Mass Transf. (2010). https://doi.org/10.1016/j.ijheatmasstransfer.2010.05.033.

[76] R. Wulf, M.A.A. Mendes, V. Skibina, A. Al-Zoubi, D. Trimis, S. Ray, U. Gross, Experimental and numerical determination of effective thermal conductivity of open cell FeCrAl-alloy metal foams, Int. J. Therm. Sci. (2014). https://doi.org/10.1016/j.ijthermalsci.2014.06.030.

[77] A.C. Kaya, C. Fleck, Deformation behavior of open-cell stainless steel foams, Mater. Sci. Eng. A. (2014). https://doi.org/10.1016/j.msea.2014.07.098.

[78] H. Oun, A. Kennedy, Tailoring the pressure-drop in multi-layered open-cell porous inconel structures, J. Porous Mater. (2015). https://doi.org/10.1007/s10934-015-0046-2.

[79] H.N.G. Wadley, N.A. Fleck, A.G. Evans, Fabrication and structural performance of periodic cellular metal sandwich structures, Compos. Sci. Technol. (2003). https://doi.org/10.1016/S0266-3538(03)00266-5.

[80] H.N.G. Wadley, Cellular metals manufacturing, Adv. Eng. Mater. (2002). https://doi.org/10.1002/1527-2648(20021014)4:10<726::AID-ADEM726>3.0.CO;2-Y.

[81] H.N.G. Wadley, Multifunctional periodic cellular metals, Philos. Trans. R. Soc. A Math. Phys. Eng. Sci. (2006). https://doi.org/10.1098/rsta.2005.1697.

[82] K.J. Kang, Wire-woven cellular metals: The present and future, Prog. Mater. Sci. (2015). https://doi.org/10.1016/j.pmatsci.2014.11.003.

[83] G.O. Cook, C.D. Sorensen, Overview of transient liquid phase and partial transient liquid phase bonding, J. Mater. Sci. (2011). https://doi.org/10.1007/s10853-011-5561-1.

[84] J. Tian, T. Kim, T.J. Lu, H.P. Hodson, D.T. Queheillalt, D.J. Sypeck, H.N.G. Wadley, The effects of topology upon fluid-flow and heat-transfer within cellular copper structures, Int. J. Heat Mass Transf. (2004). https://doi.org/10.1016/j.ijheatmasstransfer.2004.02.010.

[85] J. Tian, T.J. Lu, H.P. Hodson, D.T. Queheillalt, H.N.G. Wadley, Cross flow heat exchange of textile cellular metal core sandwich panels, Int. J. Heat Mass Transf. (2007). https://doi.org/10.1016/j.ijheatmasstransfer.2006.11.042.

[86] J. Xu, J. Tian, T.J. Lu, H.P. Hodson, On the thermal performance of wire-screen meshes as heat exchanger material, Int. J. Heat Mass Transf. (2007). https://doi.org/10.1016/j.ijheatmasstransfer.2006.05.044.

[87] L. Zhao, S.M. Ryan, J.K. Ortega, S. Ha, K.W. Sharp, J.K. Guest, K.J. Hemker, T.P. Weihs, Experimental investigation of 3D woven Cu lattices for heat exchanger applications, Int. J. Heat Mass Transf. (2016). https://doi.org/10.1016/j.ijheatmasstransfer.2015.12.059.

[88] J.H. Joo, K.J. Kang, T. Kim, T.J. Lu, Forced convective heat transfer in all metallic wire-woven bulk Kagome sandwich panels, Int. J. Heat Mass Transf. (2011). https://doi.org/10.1016/j.ijheatmasstransfer.2011.08.018.

[89] J.H. Joo, K.J. Kang, B.S. Kang, The hydraulic and heat transfer characteristics for the Wire-woven Bulk Kagome (WBK) composed of aluminum helix wires, in: MetFoam 2007 - Proc. 5th Int. Conf. Porous Met. Met. Foam., 2008.

[90] X. Yang, J. Bai, K.-J. Kang, T. Lu, T. Kim, Effective thermal conductivity of wire-woven bulk Kagome sandwich panels, Theor. Appl. Mech. Lett. (2014). https://doi.org/10.1063/2.1405110.

[91] S.S. Feng, M.Z. Li, J.H. Joo, K.J. Kang, T. Kim, T.J. Lu, Thermomechanical properties of brazed wire-woven bulk Kagome cellular metals for multifunctional applications, J. Thermophys. Heat Transf. (2012). https://doi.org/10.2514/1.49434.

[92] J. Xu, R.A. Wirtz, In-plane effective thermal conductivity of plain-weave screen laminates, in: IEEE Trans. Components Packag. Technol., 2002. https://doi.org/10.1109/TCAPT.2002.807993.

[93] K.S. Remella, F.M. Gerner, In-plane effective thermal conductivity of a single layered metallic wire-mesh screen, in: Annu. IEEE Semicond. Therm. Meas. Manag. Symp., 2016. https://doi.org/10.1109/SEMI-THERM.2016.7458446.

[94] X.H. Yang, J.X. Bai, K.J. Kang, T.J. Lu, T. Kim, Experimental Investigations of Natural Convection in Wire-Woven Bulk Kagome, Transp. Porous Media. (2014). https://doi.org/10.1007/s11242-014-0354-z.

[95] V.B. Gawande, A.S. Dhoble, D.B. Zodpe, Effect of roughness geometries on heat transfer enhancement in solar thermal systems - A review, Renew. Sustain. Energy Rev. (2014). https://doi.org/10.1016/j.rser.2014.01.024.

[96] S.B. Prasad, J.S. Saini, K.M. Singh, Investigation of heat transfer and friction characteristics of packed bed solar air heater using wire mesh as packing material, Sol. Energy. (2009). https://doi.org/10.1016/j.solener.2008.11.011.

[97] L. Varshney, J.S. Saini, Heat transfer and friction factor correlations for rectangular solar air heater duct packed with wire mesh screen matrices, Sol. Energy. (1998). https://doi.org/10.1016/S0038-092X(98)00017-6.

[98] R. Kurian, C. Balaji, S.P. Venkateshan, Experimental investigation of near compact wire mesh heat exchangers, Appl. Therm. Eng. (2016). https://doi.org/10.1016/j.applthermaleng.2016.07.172.

[99] E.M.S. El-Said, S.M. Elshamy, A.E. Kabeel, Performance enhancement of a tubular solar still by utilizing wire mesh packing under harmonic motion, Desalination. (2020). https://doi.org/10.1016/j.desal.2019.114165.

[100] M.A. Sayed, A.M.T.A. ELdein Hussin, N.A. Mahmoud, W. Aboelsoud, Performance evaluation of wire mesh heat exchangers, Appl. Therm. Eng. (2020). https://doi.org/10.1016/j.applthermaleng.2019.114891.

[101] R. Kurian, C. Balaji, S.P. Venkateshan, Experimental investigation of convective heat transfer in a vertical channel with brass wire mesh blocks, Int. J. Therm. Sci. (2016). https://doi.org/10.1016/j.ijthermalsci.2015.08.002.

[102] H. Yan, X. Yang, T. Lu, G. Xie, Convective heat transfer in a lightweight multifunctional sandwich panel with X-type metallic lattice core, Appl. Therm. Eng. (2017). https://doi.org/10.1016/j.applthermaleng.2017.08.081.

[103] O. Sanz, E.D. Banús, A. Goya, H. Larumbe, J.J. Delgado, A. Monzón, M. Montes, Stacked wire-mesh monoliths for VOCs combustion: Effect of the mesh-opening in the catalytic performance, Catal. Today. (2017). https://doi.org/10.1016/j.cattod.2017.05.054.

[104] A. V. Porsin, A. V. Kulikov, V.N. Rogozhnikov, A.N. Serkova, A.N. Salanov, K.I. Shefer, Structured reactors on a metal mesh catalyst for various applications, Catal. Today. (2016). https://doi.org/10.1016/j.cattod.2016.03.033.

[105] T. Li, Dependence of filtration properties on stainless steel medium structure, Filtr. Sep. (1997). https://doi.org/10.1016/S0015-1882(97)90379-7.

[106] M.K. Mittal, L. Varshney, Optimal thermohydraulic performance of a wire mesh packed solar air heater, Sol. Energy. (2006). https://doi.org/10.1016/j.solener.2005.10.004.

[107] S. Mori, K. Okuyama, Enhancement of the critical heat flux in saturated pool boiling using honeycomb porous media, Int. J. Multiph. Flow. (2009). https://doi.org/10.1016/j.ijmultiphaseflow.2009.05.003.

[108] X. Dai, F. Yang, R. Yang, Y.C. Lee, C. Li, Micromembrane-enhanced capillary evaporation, Int. J. Heat Mass Transf. (2013). https://doi.org/10.1016/j.ijheatmasstransfer.2013.05.030.

[109] Z.G. Xu, C.Y. Zhao, Experimental study on pool boiling heat transfer in gradient metal foams, Int. J. Heat Mass Transf. (2015). https://doi.org/10.1016/j.ijheatmasstransfer.2015.02.017.

[110] Z.G. Xu, J. Qin, Pool boiling investigation on gradient metal foams with double layers, Appl. Therm. Eng. (2018). https://doi.org/10.1016/j.applthermaleng.2017.12.040.

[111] L.L. Manetti, G. Ribatski, R.R. de Souza, E.M. Cardoso, Pool boiling heat transfer of HFE-7100 on metal foams, Exp. Therm. Fluid Sci. (2020). https://doi.org/10.1016/j.expthermflusci.2019.110025.

[112] Z.G. Xu, C.Y. Zhao, Pool boiling heat transfer of open-celled metal foams with V-shaped grooves for high pore densities, Exp. Therm. Fluid Sci. (2014). https://doi.org/10.1016/j.expthermflusci.2013.09.003.

[113] R. Pastuszko, Pool boiling heat transfer on micro-fins with wire mesh – Experiments and heat flux prediction, Int. J. Therm. Sci. (2018). https://doi.org/10.1016/j.ijthermalsci.2017.11.019.

[114] R. Pastuszko, R. Kaniowski, T.M. Wójcik, Comparison of pool boiling performance for plain micro-fins and micro-fins with a porous layer, Appl. Therm. Eng. (2020). https://doi.org/10.1016/j.applthermaleng.2019.114658.

[115] C. Zhang, L. Zhang, H. Xu, P. Li, B. Qian, Performance of pool boiling with 3D grid structure manufactured by selective laser melting technique, Int. J. Heat Mass Transf. (2019). https://doi.org/10.1016/j.ijheatmasstransfer.2018.09.021.

[116] K.K. Wong, K.C. Leong, Saturated pool boiling enhancement using porous lattice structures produced by Selective Laser Melting, Int. J. Heat Mass Transf. (2018). https://doi.org/10.1016/j.ijheatmasstransfer.2017.12.148.

[117] R.S. Bunker, A review of shaped hole turbine film-cooling technology, J. Heat Transfer. (2005). https://doi.org/10.1115/1.1860562.

[118] Z. Min, G. Huang, S.N. Parbat, L. Yang, M.K. Chyu, Experimental investigation on additively manufactured transpiration and film cooling structures, J. Turbomach. 141 (2019) 1–10. https://doi.org/10.1115/1.4042009.

[119] G. Huang, Z. Min, L. Yang, P.X. Jiang, M. Chyu, Transpiration cooling for additive manufactured porous plates with partition walls, Int. J. Heat Mass Transf. (2018). https://doi.org/10.1016/j.ijheatmasstransfer.2018.03.110.

[120] O.T. Ibrahim, J.G. Monroe, S.M. Thompson, N. Shamsaei, H. Bilheux, A. Elwany, L. Bian, An investigation of a multi-layered oscillating heat pipe additively manufactured from Ti-6Al-4V powder, Int. J. Heat Mass Transf. 108 (2017) 1036–1047. https://doi.org/10.1016/j.ijheatmasstransfer.2016.12.063.

[121] D. Jafari, W.W. Wits, B.J. Geurts, Phase change heat transfer characteristics of an additively manufactured wick for heat pipe applications, Appl. Therm. Eng. 168 (2020) 114890. https://doi.org/10.1016/j.applthermaleng.2019.114890.

[122] T. Kim, H.P. Hodson, T.J. Lu, Contribution of vortex structures and flow separation to local and overall pressure and heat transfer characteristics in an ultralightweight lattice material, Int. J. Heat Mass Transf. (2005). https://doi.org/10.1016/j.ijheatmasstransfer.2005.04.026.

[123] T. Kim, C.Y. Zhao, T.J. Lu, H.P. Hodson, Convective heat dissipation with lattice-frame materials, in: Mech. Mater., 2004. https://doi.org/10.1016/j.mechmat.2003.07.001.

[124] K.N. Son, J.A. Weibel, V. Kumaresan, S. V. Garimella, Design of multifunctional lattice-frame materials for compact heat exchangers, Int. J. Heat Mass Transf. (2017). https://doi.org/10.1016/j.ijheatmasstransfer.2017.07.073.

[125] X. Zhang, X. Jin, G. Xie, H. Yan, Thermo-fluidic comparison between sandwich panels with tetrahedral lattice cores fabricated by casting and metal sheet folding, Energies. (2017). https://doi.org/10.3390/en10070906.

[126] H.B. Yan, Q.C. Zhang, T.J. Lu, An X-type lattice cored ventilated brake disc with enhanced cooling performance, Int. J. Heat Mass Transf. (2015). https://doi.org/10.1016/j.ijheatmasstransfer.2014.09.060.

[127] H.B. Yan, Q.C. Zhang, T.J. Lu, T. Kim, A lightweight X-type metallic lattice in single-phase forced convection, Int. J. Heat Mass Transf. (2015). https://doi.org/10.1016/j.ijheatmasstransfer.2014.11.061.

[128] X. Jin, Y. Li, H. Yan, G. Xie, Comparative study of flow structures and heat transfer enhancement in a metallic lattice fabricated by metal sheet folding: Effects of punching location shift, Int. J. Heat Mass Transf. (2019). https://doi.org/10.1016/j.ijheatmasstransfer.2019.01.036.

[129] X. Jin, B. Shen, H. Yan, B. Sunden, G. Xie, Comparative evaluations of thermofluidic characteristics of sandwich panels with X-lattice and Pyramidal-lattice cores, Int. J. Heat Mass Transf. (2018). https://doi.org/10.1016/j.ijheatmasstransfer.2018.07.087.

[130] Y. Ma, H. Yan, K. Hooman, G. Xie, Enhanced heat transfer in a pyramidal lattice sandwich panel by introducing pin-fins/protrusions/dimples, Int. J. Therm. Sci. (2020). https://doi.org/10.1016/j.ijthermalsci.2020.106468.

[131] Y. Ma, H. Yan, G. Xie, Flow and thermal performance of sandwich panels with plate fins or/and pyramidal lattice, Appl. Therm. Eng. (2020). https://doi.org/10.1016/j.applthermaleng.2019.114468.

[132] Y. Li, G. Xie, S.K.S. Boetcher, H. Yan, Heat transfer enhancement of X-lattice-cored sandwich panels by introducing pin fins, dimples or protrusions, Int. J. Heat Mass Transf. (2019). https://doi.org/10.1016/j.ijheatmasstransfer.2019.07.009.

[133] H. Yan, Q. Zhang, W. Chen, G. Xie, J. Dang, T.J. Lu, An X-lattice cored rectangular honeycomb with enhanced convective heat transfer performance, Appl. Therm. Eng. (2020). https://doi.org/10.1016/j.applthermaleng.2019.114687.

[134] L. Valdevit, A. Pantano, H.A. Stone, A.G. Evans, Optimal active cooling performance of metallic sandwich panels with prismatic cores, Int. J. Heat Mass Transf. (2006). https://doi.org/10.1016/j.ijheatmasstransfer.2006.03.042.

[135] B. Hanks, J. Berthel, M. Frecker, T.W. Simpson, Mechanical properties of additively manufactured metal lattice structures: Data review and design interface, Addit. Manuf. (2020). https://doi.org/10.1016/j.addma.2020.101301.

[136] D. Ali, S. Sen, Finite element analysis of mechanical behavior, permeability and fluid induced wall shear stress of high porosity scaffolds with gyroid and lattice-based architectures, J. Mech. Behav. Biomed. Mater. (2017). https://doi.org/10.1016/j.jmbbm.2017.07.035.

[137] M. Wong, I. Owen, C.J. Sutcliffe, A. Puri, Convective heat transfer and pressure losses across novel heat sinks fabricated by Selective Laser Melting, Int. J. Heat Mass Transf. (2009). https://doi.org/10.1016/j.ijheatmasstransfer.2008.06.002.

[138] A. Elkholy, R. Kempers, Enhancement of pool boiling heat transfer using 3D-printed polymer fixtures, Exp. Therm. Fluid Sci. (2020). https://doi.org/10.1016/j.expthermflusci.2020.110056.

[139] J.Y. Ho, K.C. Leong, T.N. Wong, Additively-manufactured metallic porous lattice heat exchangers for air-side heat transfer enhancement, Int. J. Heat Mass Transf. (2020). https://doi.org/10.1016/j.ijheatmasstransfer.2019.119262.

[140] J.Y. Ho, K.C. Leong, T.N. Wong, Experimental and numerical investigation of forced convection heat transfer in porous lattice structures produced by selective laser melting, Int. J. Therm. Sci. (2019). https://doi.org/10.1016/j.ijthermalsci.2018.11.022.

[141] J.Y. Ho, K.C. Leong, Cylindrical porous inserts for enhancing the thermal and hydraulic performance of water-cooled cold plates, Appl. Therm. Eng. (2017). https://doi.org/10.1016/j.applthermaleng.2017.04.101.

[142] S. Yun, J. Kwon, D.C. Lee, H.H. Shin, Y. Kim, Heat transfer and stress characteristics of additive manufactured FCCZ lattice channel using thermal fluid-structure interaction model, Int. J. Heat Mass Transf. (2020). https://doi.org/10.1016/j.ijheatmasstransfer.2019.119187.

[143] A. Chaudhari, P. Ekade, S. Krishnan, Experimental investigation of heat transfer and fluid flow in octet-truss lattice geometry, Int. J. Therm. Sci. (2019). https://doi.org/10.1016/j.ijthermalsci.2019.05.003.

[144] J. Broughton, Y. Joshi, Comparison of Single-Phase Convection in Additive Manufactured Versus Traditional Metal Foams, J. Heat Transfer. (2020). https://doi.org/10.1115/1.4046972.

[145] K. Saha, S. Acharya, C. Nakamata, Heat Transfer Enhancement and Thermal Performance of Lattice Structures for Internal Cooling of Airfoil Trailing Edges, J. Therm. Sci. Eng. Appl. (2013). https://doi.org/10.1115/1.4007277.

[146] C. Carcasci, B. Facchini, M. Pievaroli, L. Tarchi, A. Ceccherini, L. Innocenti, Heat transfer and pressure loss measurements of matrix cooling geometries for gas turbine airfoils, in: Proc. ASME Turbo Expo, 2014. https://doi.org/10.1115/GT2014-25384.

[147] D. Liang, W. Bai, W. Chen, M.K. Chyu, Investigating the effect of element shape of the face-centered cubic lattice structure on the flow and endwall heat transfer characteristics in a rectangular channel, Int. J. Heat Mass Transf. (2020). https://doi.org/10.1016/j.ijheatmasstransfer.2020.119579.

[148] B. Shen, Y. Li, H. Yan, S.K.S. Boetcher, G. Xie, Heat transfer enhancement of wedge-shaped channels by replacing pin fins with Kagome lattice structures, Int. J. Heat Mass Transf. (2019). https://doi.org/10.1016/j.ijheatmasstransfer.2019.06.059.

[149] D.A. Ramirez, L.E. Murr, S.J. Li, Y.X. Tian, E. Martinez, J.L. Martinez, B.I. Machado, S.M. Gaytan, F. Medina, R.B. Wicker, Open-cellular copper structures fabricated by additive manufacturing using electron beam melting, Mater. Sci. Eng. A. (2011). https://doi.org/10.1016/j.msea.2011.03.053.

[150] Z. Ma, D.Z. Zhang, F. Liu, J. Jiang, M. Zhao, T. Zhang, Lattice structures of Cu-Cr-Zr copper alloy by selective laser melting: Microstructures, mechanical properties and energy absorption, Mater. Des. (2020). https://doi.org/10.1016/j.matdes.2019.108406.

[151] I. Kaur, P. Singh, Flow and Thermal Transport Through Unit Cell Topologies of Cubic and Octahedron Families, Int. J. Heat Mass Transf. (2020). https://doi.org/10.1016/j.ijheatmasstransfer.2020.119784.

[152] A.D. Dressler, E.W. Jost, J.C. Miers, D.G. Moore, C.C. Seepersad, B.L. Boyce, Heterogeneities dominate mechanical performance of additively manufactured metal lattice struts, Addit. Manuf. (2019). https://doi.org/10.1016/j.addma.2019.06.011.

[153] C.Y. Lin, T. Wirtz, F. LaMarca, S.J. Hollister, Structural and mechanical evaluations of a topology optimized titanium interbody fusion cage fabricated by selective laser melting process, J. Biomed. Mater. Res. - Part A. (2007). https://doi.org/10.1002/jbm.a.31231.

[154] S. Arabnejad, R. Burnett Johnston, J.A. Pura, B. Singh, M. Tanzer, D. Pasini, High-strength porous biomaterials for bone replacement: A strategy to assess the interplay between cell morphology, mechanical properties, bone ingrowth and manufacturing constraints, Acta Biomater. (2016). https://doi.org/10.1016/j.actbio.2015.10.048.

[155] I. Echeta, X. Feng, B. Dutton, R. Leach, S. Piano, Review of defects in lattice structures manufactured by powder bed fusion, Int. J. Adv. Manuf. Technol. (2020). https://doi.org/10.1007/s00170-019-04753-4.

[156] R. Gümrük, R.A.W. Mines, S. Karadeniz, Static mechanical behaviours of stainless steel micro-lattice structures under different loading conditions, Mater. Sci. Eng. A. (2013). https://doi.org/10.1016/j.msea.2013.07.070.

[157] S. Tsopanos, R.A.W. Mines, S. McKown, Y. Shen, W.J. Cantwell, W. Brooks, C.J. Sutcliffe, The influence of processing parameters on the mechanical properties of selectively laser melted stainless steel microlattice structures, J. Manuf. Sci. Eng. Trans. ASME. (2010). https://doi.org/10.1115/1.4001743.

[158] T. Yu, H. Hyer, Y. Sohn, Y. Bai, D. Wu, Structure-property relationship in high strength and lightweight AlSi10Mg microlattices fabricated by selective laser melting, Mater. Des. (2019). https://doi.org/10.1016/j.matdes.2019.108062.

[159] A. Du Plessis, D.P. Kouprianoff, I. Yadroitsava, I. Yadroitsev, Mechanical properties and in situ deformation imaging of microlattices manufactured by laser based powder bed fusion, Materials (Basel). (2018). https://doi.org/10.3390/ma11091663.

[160] C. Kenel, N.P.M. Casati, D.C. Dunand, 3D ink-extrusion additive manufacturing of CoCrFeNi high-entropy alloy micro-lattices, Nat. Commun. (2019). https://doi.org/10.1038/s41467-019-08763-4.

[161] A. Vyatskikh, S. Delalande, A. Kudo, X. Zhang, C.M. Portela, J.R. Greer, Additive manufacturing of 3D nano-architected metals, Nat. Commun. (2018). https://doi.org/10.1038/s41467-018-03071-9.

[162] T. Kolb, F. Huber, B. Akbulut, C. Donocik, N. Urban, D. Maurer, J. Franke, Laser Beam Melting of NdFeB for the production of rare-earth magnets, in: 2016 6th Int. Electr. Drives Prod. Conf. EDPC 2016 - Proc., 2016. https://doi.org/10.1109/EDPC.2016.7851311.

[163] N. Urban, F. Huber, J. Franke, Influences of process parameters on rare earth magnets produced by laser beam melting, in: 2017 7th Int. Electr. Drives Prod. Conf. EDPC 2017 - Proc., 2018. https://doi.org/10.1109/EDPC.2017.8328149.

CHAPTER III

FLOW AND THERMAL TRANSPORT THROUGH UNIT CELL TOPOLOGIES OF CUBIC AND OCTAHEDRON FAMILIES[2]

Abstract

Advancements in Additive Manufacturing (AM) routes have opened several opportunities for manufacturing complex porous structures which could not have been manufactured by the conventional *foaming* process that essentially results in unit cells represented as *Tetrakaidecahedron (TKD)* shape. The regular open-cell lattices belonging to the cubic and octahedron family of structures provide wide spectrum of porosity, pore-density, permeability, and surface area-to-volume ratios. These complex cell topologies can potentially be manufactured additively, making the realization of above-mentioned properties possible. For efficient heat exchanger designs, the reticulated structures made from these unit cells are expected to have higher permeability, porosity, effective thermal conductivity, and interstitial heat transfer coefficient. A detailed understanding of local flow and heat transport characteristics is necessary to design unit cells with such properties. To this end, four different metal foam unit cell topologies have been investigated in the present study, viz. *Tetrakaidecahedron (TKD), Cube*, *FD-Cube* and *Octet*. The

---

[2] Kaur, I. and Singh, P., 2020. Flow and thermal transport through unit cell topologies of cubic and octahedron families. International Journal of Heat and Mass Transfer, 158, p.119784.
doi: 10.1016/j.ijheatmasstransfer.2020.119784

Cube and *FD-Cube* unit cell topologies investigated in the present study belong to the cubic family, where the fibers are present only along the edges and face of the unit cell volume. The *TKD* and *Octet* configurations belong to the octahedron class of lattices, where complex connectivity exists within the unit cell volume. To allow for direct comparison between these three unit cells, circular fibers are chosen, which is different from the general *TKD* cells (tricuspid cross-sections). The porosity was fixed 0.986 which dictated the fiber dimensions of respective unit cells, with *Octet* fibers being thinnest. Direct simulations have been carried out with periodic boundary conditions on unit cell faces which were parallel to the flow. Such configurations when reticulated in three dimensions are representative of porous structures which are single-cell thick in the streamwise direction. These foam shapes have been proven to be very efficient as they do not allow the thermal boundary layer development. Flow and heat transfer results obtained for above boundary conditions have also been compared with the periodic boundary condition on all the faces.

The direct simulation results include pressure drop per unit length and volumetric Nusselt number (corresponding to constant heat flux and constant wall temperature boundary conditions on fibers). Flow stagnation on fibers was the main contributor for both, pressure drop increase, and interstitial heat transfer enhancement. *TKD* unit cell had higher flow losses and thermal performance than *FD-Cube*. *Octet* (octahedron family) configuration had the highest flow losses as well as Nusselt number compared to all other unit cell topologies, because of the large surface area offered for flow stagnation.

Keywords: Metal foam; lattice structure; heat transfer.

3.1 Introduction

Open-celled metal foams have been proven to be efficient for heat exchanger applications involving forced convection, as they provide high effective thermal conductivity due to the three-dimensional interconnections of fibers and promote enhanced mixing due to tortuosity in flow path. The flow mixing assisted high interstitial heat transfer coefficient when coupled with high wetted surface area yields enhanced heat dissipation. Most of the studies involve metal foams manufactured through *foaming* process where the resultant *TKD* cells are stochastic in nature, such that the pores are interconnected by a complex and random arrangement of fibers (a.k.a. struts). Earlier investigations on metal foams were focused on experimental determination of permeability (K), inertial coefficient (C_f), effective thermal conductivity (k_{eff}) and interstitial heat transfer coefficient (h_{sf}). Above flow and thermal characteristics are usually combined with constituent geometric parameters, commonly pore- and fiber-diameters, to construct the semi-empirical correlations. These relationships are employed in volume-averaged computational flow and heat transfer studies, which is a very cost-effective way to analyze thermal systems involving metal foams. However, the volume-averaged simulations do not provide any information regarding flow and thermal transport at the pore/fiber-level.

Hwang et al. [1] performed experimental investigation on aluminum foams with porosities ($\boldsymbol{\varepsilon}$) 0.7, 0.8 and 0.95 for Reynolds number ranging between 1900 and 7800. Under constant pumping power, the highest thermal hydraulic performance was obtained for 0.8 porosity foam. The correlations for Nusselt number versus Reynolds number (both based on pore diameter) were developed for the foam samples. Their [1] heat transfer results were in good agreement with Younis and Viskanta [2] and Ichimiya et al. [3]. The effect of porosity ($\boldsymbol{\varepsilon}$ ~ 0.87 to 0.94), pore density (PPI = 10, 20 and 40) and Reynolds number (based on equivalent pore diameter, Re_d ~ 6 to 45) on the frictional losses and Nusselt number was analyzed in an experimental study by Hsieh et al. [4]. The Nusselt number showed increasing trend with increasing porosity and pore density, and this trend was attributed to the enhanced surface area of metal foam for heat dissipation. The authors also reported the presence of local thermal non-equilibrium (LTNE) based on the temperature difference measured for the solid- and gas-phases. Mancin et al. [5] explored different metal foam samples to analyze the effect of pore density (PPI ~ 5 to 40), porosity ($\boldsymbol{\varepsilon}$ ~ 0.896 to 0.956), foam sample heights (H= 20 and 40 mm), mass flow rate ($\dot{m}$)and heat flux (q") on net convective heat transport and pressure drop. Copper foams yielded in the highest heat dissipation due to their inherent higher solid-phase thermal conductivity. Correlations were proposed for interstitial heat transfer coefficient (h_{sf}) and pressure gradient based on the Reynolds number, Prandtl number, fiber thickness, porosity and pore density.

Paek et al. [6] evaluated the thermophysical properties of aluminum metal foams. The authors provided the effective thermal conductivity (k_e) and permeability (K) for metal foams in porosity range of ~ 0.89 to 0.96. The effective thermal conductivity increased with decreasing porosity, however negligible dependence on the pore sizes (d= 0.665, 1.25 and 2.50 mm) was observed. In contrast to the effective thermal conductivity, permeability was found to be dependent on both porosity and pore size. Experimental, analytical and computational work was conducted by Calmidi et al. [7-9] to find the effective thermal conductivity, thermal dispersion conductivity (k_d), interstitial heat transfer coefficient and permeability. Zhao et al. [10] explored the temperature dependence of the effective thermal conductivity (k_e) of the steel-alloy foams under ambient as well vacuum conditions for a temperature range of ~ 500K to 800K. For temperature higher than 500K, the thermal conductivity was found to be increasing with increase in temperature. Heat conduction was found to be significantly influenced by natural convection which depended upon the void space and local solid- and fluid-phase density differences.

Volume-averaged simulations have been extensively employed in past, to predict the thermal behavior of metal foams. The correlations for interfacial heat transfer coefficient and surface area density obtained from the experimental investigations in [7-9] were employed by Nithyanandam and Mahajan [11] in their study on using metal foams in waste heat recovery applications through volume-averaged computations. Feng et al. [12] and Yang et al. [13] performed the volume-averaged simulations in metal foams infused with phase change materials (PCM), and their results were in good agreement with the DNS results for a unit cell configuration. In another numerical investigation by Hu et al. [14], the DNS were performed on the real micro-foam geometry (containing PCM) to obtain the effective thermal conductivity and interstitial heat transfer coefficient, which were further used in volume-averaged simulations. Finite-volume-based method was employed by Tian et al. [15] to investigate the temperature profiles of PCM during phase change process. The volume-averaged technique provided insight into the temperature, velocity, melting fraction and heat flux information in the domain, however the information on pore-level phenomena could not be obtained due to the nature of simulations.

More recent investigations in the past decade focused on understanding the pore- and fiber-level flow and thermal transport of the constituent unit cell with periodic boundary conditions, such that the conclusions drawn from the unit cell-based studies can be extended to their three-dimensionally reticulated structures. Since the arrangement of fibers in metal foams is highly random, the extraction of representative unit cell from these porous matrices is critical to ensure accurate flow and thermal predictions. The structure of the commercial metal foams is dependent on their manufacturing process. One method of manufacturing commercial metal foams is through injection of a foaming gas in a molten metal pool, where the gas-metal mixture is allowed to reach to an equilibrium state corresponding to the minimum surface energy of a certain volume, and the remaining metal when solidifies results in a porous structure [16]. Thus, the space filling structures which could divide the given volume into minimum surface area is a desirable candidate to represent the unit cell configuration of commercial metal foams. Lord Kelvin [17] in 1887 proposed a fourteen-sided body centered cubic (BCC) *Tetrakaidecahedron* (TKD) structure to have minimum surface area to volume ratio. Geometrically, the *TKD* structure is essentially a polyhedron with fourteen faces, where six are quadrilaterals and eight are hexagons. Lord Kelvin proposed that if slight curvature is provided to the edges of the hexagonal faces in order to satisfy the Plateau's law [18], the resulting structure would have the minimum surface area to volume ratio, and such a geometry is now popularly known as *Lord Kelvin's cell* structure. The *Lord Kelvin structure* was deemed to be the most efficient in filling a certain volume, until Weaire and Phelan [19] proposed another space filling arrangement consisting of eight polyhedron units (six of which were the fourteen-sided polyhedron and two were the twelve-sided polyhedron). This arrangement [19] was concluded to have 0.3% less surface area energy as compared to the Lord Kelvin's *TKD*. From the perspective of minimum surface area by volume ratio occupied by these structures and the physics guiding the equilibrium structure of the metal foams during commercial manufacturing, both the Kelvin as well as Weaire-Phelan models have been numerically simulated to visualize pore-level phenomenon of the metal foams.

These unit cells are commonly constructed through following methods, (i) Kelvin and Weaire-Phelan model generation using *Surface Evolver* software, (ii) X-ray micro tomography (CT scan), (iii) geometrical construction of idealized unit cells in a CAD software. Brakke et al. [21] developed *Surface Evolver* program that iteratively minimizes the surface energy of a body subjected to constraints by energy-gradient descent method. The Lord Kelvin and Weaire-Phelan structures are thus created by minimizing the surface area energy using constant volume constraint. The steps involved in the generation of these models in this software are elaborated in [20, 21]. Another methodology is the use of X-ray CT scan images of the commercial metal foams to reconstruct the metal foams and further post-process in suitable software (e.g. Simpleware [22]), which makes the model compatible with other CAD or mesh generating modules. The resultant models provided by the *Surface Evolver* are the exact representation of the Kelvin and Weaire-Phelan models, which are considered as the open-cell metal foam representative unit cell based on physical arguments whereas the final three-dimensional structure obtained by CT image processing is the exact representation of the randomly organized unit cells of which metal foam volume is comprised of. An alternative approach to the above discussed procedures to model open-cell metal foams is to manually construct the idealized unit cells using a suitable CAD software. Body-centered cubic (BCC) structure as well sphere-centered *TKD* are generally explored for the unit cell investigation where the BCC structure is generated by extracting the spheres from the corner and center of the unit cube volume and the sphere-centered *TKD* structure is generated by subtracting a sphere from a regular octahedron geometry. The details of the construction procedure as well as the differences in the resulting geometries obtained from these two procedures is presented in the following section. It should be noted that the above BCC and sphere-centered *TKD* structures are near-exact geometries of Lord Kelvin cell structure and much easier to create as compared to that by *Surface Evolver* and CT imaging. Also, these simplified ideal structures can accurately predict the pressure drop as well as heat transfer characteristics of actual foams.

The analytical expression for effective thermal conductivity of *TKD* structure (with saturated fluid) was derived by Boomsma and Poulikakos [23], which showed good agreement with their experimental results. Both air and water working fluids were studied with aluminum as solid phase with porosity of 0.95. The authors concluded that the effective thermal conductivity was dominantly controlled by the thermal conductivity of the solid phase. In another study by Boomsma et al. [24], the flow through Weaire-Phelan cell structure ($\boldsymbol{\varepsilon} = 0.96$) developed in

Surface Evolver with water as the working fluid was simulated. The pressure drop values were significantly lower than the experimentally reported values in [25], and this discrepancy was attributed to the presence of wall effects in the physical set-up. Krishnan et al. [26] performed direct simulations on fully periodic body-centered-cubic (BCC) unit cell and reported the effective thermal conductivities and normalized permeability as a function of porosity, friction factor as a function of Reynolds number (based on Brinkman screening length, $\sqrt{K}$) and Nusselt number as a function of Peclet number. Kopanidis et al. [27] studied conjugate heat transfer in a high porosity pore-scale model. The heat transfer coefficients obtained from conjugate analysis were compared to that obtained from constant fiber temperature boundary condition. The values for conjugate heat transfer coefficient were reported to be lower than that in fixed fiber temperature case. Bai and Chung [28] numerically investigated sphere-centered *TKD* structure with porosity of 0.97. The pressure drop results showed good agreement with the experimental study in [29]. Cunsolo et al. [21] compared the volumetric heat transfer coefficient and friction factor values of fluid domain packed with Lord Kelvin and Weaire-Phelan foam models ($\boldsymbol{\varepsilon}$ = 0.85, 0.90 and 0.95) developed in *Surface Evolver* software. The percentage difference between Nusselt number and frictional losses for porosity greater than 0.90 was less than 5% and 10%, respectively. The authors concluded that the Lord Kelvin cell structure can be used to simulate porous medium for higher porosity without compromising the accuracy. Diani et al. [30] performed numerical investigation on a foam matrix domain reconstructed from micro-CT scan to analyze the pressure drop and heat transfer characteristics. The pore level flow dynamics was visualized, and interfacial heat transfer coefficient was calculated by employing constant heat flux boundary condition on the fibers. Similar geometry reconstruction procedure was adopted by Dixit and Ghosh [31] to visualize flow development in open-cell metal foam fin. Iasiello et al. [32] studied the developing flow in a fluid domain consisting of twenty-one Kelvin model unit cells in a row. The authors identified the following three regions: impingement zone, thermally developing and thermally developed zone. Recently, numerical investigation was performed on an octet-truss lattice structure by Ekade and Krishnan [33] for which the normalized permeability, effective thermal conductivity, Nusselt number and friction factors were reported for different porosity values. These unit cell simulations provided insight into pore-level fluid-metal interaction and improved the understanding of the flow physics in the Octet-cell based metal foam volumes.

The above discussion suggests that the open-cell morphology of the commercial metal-foams provides high heat exchange. The fiber inter-connections can be controlled by direct molding or additive processes which can result in an organized metal foam volume with superior thermal-hydraulic performance. In this paper, the regular metal foams with *TKD* unit cell have been studied as the baseline configuration. Three fiber topologies, viz. *Cube, Face Diagonal (FD)-Cube* and *Octet* have been explored in contrast with the conventional *TKD*. The flow dynamics, pressure losses and volumetric Nusselt number of the unit cell topologies are compared for range of inlet velocities such that the flow is in laminar regime. The local interstitial heat transfer coefficient was evaluated for constant heat flux and constant temperature boundary condition imposed on the fiber walls and corresponding volumetric Nusselt number was obtained by using appropriate characteristic length scale. The working fluid was air in this study.

3.2 Generation of Tetrakaidecahedron (TKD) structure

As mentioned earlier, the body-centered cube (BCC) and sphere-centered *TKD* structures are used as representative unit cell volume to simulate the open-cell metal foams produced by the foaming process. The open-cell BCC structure is obtained by subtracting sphere volumes from the corners and the center of solid cube volume as shown in Fig. 3.1a.

Sphere-centered *TKD* is constructed from a truncated octahedron (Fig. 3.1b). Six-corners of a regular octahedron are sliced to generate regular truncated octahedron. A sphere is then subtracted from the center of the truncated octahedron yielding the final sphere-centered *TKD*. The fibers in the BCC structure are curved as compared to sphere-centered *TKD*. Although, model generation is simple through these two procedures, the resultant geometries have some limitations on minimum porosity that can be achieved.

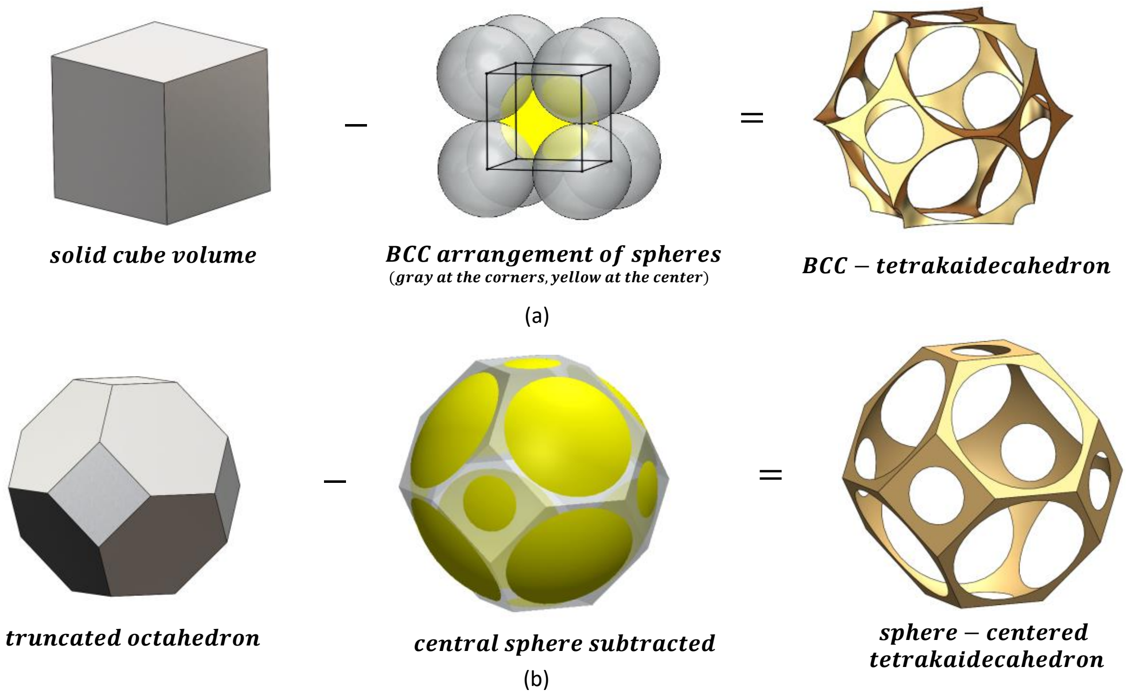

Figure 3.1 Model generation procedure for (a) BCC and (b) sphere-centered TKD

Both BCC and sphere-centered *TKD* cell can be bounded in a unit cube cell of edge length ‘s’, and an example of the sphere-centered *TKD* cell is shown in Fig. 3.2. For the resultant BCC as well as sphere-centered *TKD* cell, the radius of the sphere (R) which is subtracted from the solid cube volume as well as truncated octahedron should be greater than half of the cube edge length

($R > s/2$) for an open-celled structure, which imposes a constraint on the porosity. Analytical analysis of Krishnan et al. [26] resulted in a minimum porosity of 0.94 for BCC cell. For porosities above 0.94, the flow and thermal transport predictions in [26] agreed well with [24]. Bai and Chung [28] analyzed the flow-field in a sphere-centered *TKD* cell and showed good agreement between the pressure drop predictions and the experimental work of [29]. Another method of generating unit cell which is representative of the open-cell metal foams produced by the foaming process is through the open-source software *Surface Evolver*. The authors in [21, 32] used this software to generate the unit cells and studied the flow-field and thermal transport.

In the present paper, flow, and thermal transport for sphere-centered *TKD* is analyzed, where the geometry is produced through the CAD software method presented in Fig. 3.1b, and the BCC geometry is used for validation purposes and is discussed at a later stage. The final geometry of *TKD* unit cell is reproduced in Fig. 3.2 where the circumscribing cube is also shown. Analytical expression for the porosity of the generated unit cell and a brief discussion on its limiting values is presented below.

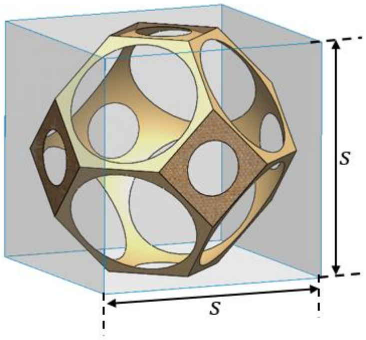

Figure 3.2 Unit cube cell of *TKD* structure

3.2.1 Sphere-centered *TKD* structure

The porosity ($\boldsymbol{\varepsilon}$) of open-cell metal foams is defined as $(\forall_{total} - \forall_s)/\forall_{total}$, where $\forall_{total} = s^3$ and $\forall_s$ is the total volume of the fibers. From the geometric calculations, the total volume occupied by the fibers or solid phase in the *TKD* unit cell is given by,

$$\forall_s = \frac{s^3}{2} - \left(\frac{4\pi R^3}{3} - \frac{6\pi}{3}\left(R - \frac{s}{2}\right)^2\left(2R + \frac{s}{2}\right) - \frac{8\pi}{3}\left(R - \frac{\sqrt{3}s}{4}\right)^2\left(2R + \frac{\sqrt{3}s}{4}\right)\right) \tag{3.1}$$

For open celled foams, $R > s/2$, hence, to facilitate further discussion, a parameter $\boldsymbol{\alpha}$ is defined such that $R = 0.5s(1 + \alpha)$ where $\boldsymbol{\alpha}$ >0. The solid phase volume can be written in the form of $\boldsymbol{\alpha}$,

$$\forall_s = \frac{s^3}{2} - \pi s^3\left[-\boldsymbol{\alpha}^3 + \left(\frac{2\sqrt{3} - 9}{4}\right)\boldsymbol{\alpha}^2 + \left(\frac{2\sqrt{3} - 3}{2}\right)\boldsymbol{\alpha} + \left(\frac{3\sqrt{3} - 4}{8}\right)\right] \tag{3.2}$$

The porosity, thus, becomes:

$$\varepsilon = \frac{1}{2} + \pi\left[-\boldsymbol{\alpha}^3 + \left(\frac{2\sqrt{3} - 9}{4}\right)\boldsymbol{\alpha}^2 + \left(\frac{2\sqrt{3} - 3}{2}\right)\boldsymbol{\alpha} + \left(\frac{3\sqrt{3} - 4}{8}\right)\right] \tag{3.3}$$

The variation of unit cell porosity with α is shown in Fig. 3.3, with porosity having a cubic dependence on the parameter α, with α=0 being the limiting case for open-cell structure. To further illustrate the limiting case of α=0 (ε=0.969), Fig. 3.4 shows the cellular structure where the pores through the square windows are not present. The value of α corresponding to $d\varepsilon/d\alpha = 0, and\ d^2\varepsilon/d\alpha^2 < 0$ was 0.077 and the corresponding porosity was 0.998. At this porosity, the TKD cell is shown in Fig. 3.4(b), where the fibers are very thin and physical realization of such fibers from manufacturability perspective is deemed unrealistic.

Further, the total fiber volume ($\forall_s$) of *TKD* can be equated to an equivalent circular cylinder with volume $\sim \pi d_f^2 L_e/4$, where the effective length L_e ($9\sqrt{2}s$) is the sum of all the edge lengths of *TKD*. The equivalent diameter can be presented by the following relation,

$$d_f = s\left(\sqrt{\frac{2\sqrt{2}}{9\pi}\left\{\frac{1}{2} - \pi\left[-\boldsymbol{\alpha}^{\mathbf{3}} + \left(\frac{2\sqrt{3}-9}{4}\right)\boldsymbol{\alpha}^{\mathbf{2}} + \left(\frac{2\sqrt{3}-3}{2}\right)\boldsymbol{\alpha} + \left(\frac{3\sqrt{3}-4}{8}\right)\right]\right\}}\right) \tag{3.4}$$

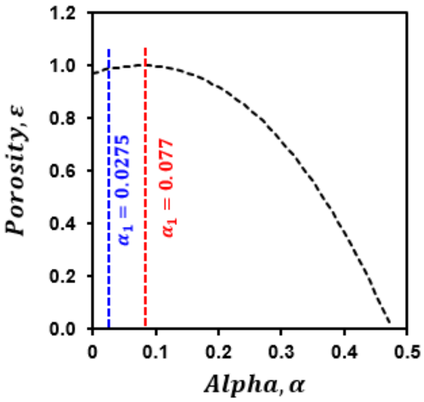

Figure 3.3 Porosity variation with respect to alpha, α

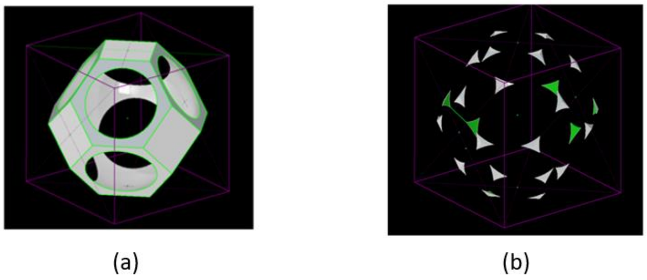
(a)
(b)

Figure 3.4 The *TKD* structure corresponding to (a) α=0, (b) α=0.077

3.3 Description of unit cell geometries

Figure 3.5 shows four different unit cell configurations (topologies) investigated in the present study. The dimensions of the *TKD* cell were similar to the one analyzed in [28]. The unit cell edge length was 2.54 mm, which would translate to 10 cells per inch (CPI) in reticulated form. Note that 10 CPI in this study is different from the 10 pores per inch (PPI) nomenclature used in the discussion related to commercial metal foams. The radius (R) of the central sphere was 2.61 mm. The resultant parameter α was 0.0275 and porosity ε was 0.986. This porosity value obtained from the mathematical analysis presented above was higher than that reported in [28]. The *Cube*, *FD-Cube* and *Octet* cell configurations (adopted from Egan et al. [34]) were inscribed in the same cubic cell and the porosity was fixed at 0.986. The construction methodology adopted for the construction of *TKD* cell resulted in a tricuspid shape (triangular cross-section), however, the fibers in *Cube, FD-Cube* and *Octet* configurations were of circular cross section. The figure given below present periodic unit cells where the truncated periodic faces are shown as textured surface.

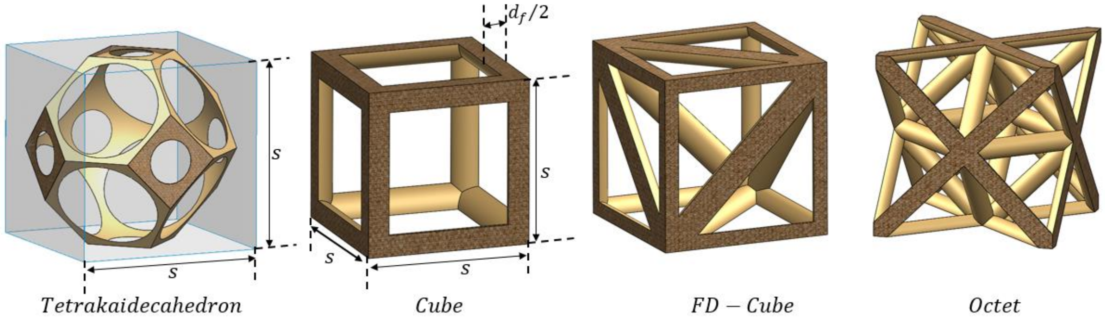

Figure 3.5 Four unit-cell configurations investigated in the present study

The geometric parameters of the configurations investigated in the current study are summarized in Table 3.1. The *Octet* configuration consisted of an octahedron with junctions at the face centers of the cube and eight tetrahedron at the cubic corners. *Octet* had the lowest fiber diameter (d_f) as compared to other configurations for same porosity. The fiber diameter for *TKD* was evaluated using *Eq*. 3.4.

Table 3.1 Fiber diameter (d_f) and Surface-to-Volume ($S/\forall_{total}$) ratio of different unit cell topologies for s=2.54 mm and ε=0.986

Unit cell topology	d_f, mm	$\frac{S}{\forall_{total}}, m^{-1}$
TKD	0.093	645.6
$Cube$	0.200	271.5
$FD - Cube$	0.129	421.9
$Octet$	0.084	644.2

3.4 Numerical setup

This section provides details of the fluid domain, boundary conditions, mesh generation, grid independence study, pressure drop as well as interstitial heat transfer calculation procedure.

3.4.1 Fluid Domain and boundary conditions

Figure 6 shows the computational domain with the boundary condition types and important dimensions highlighted. The fiber skeletons were subtracted from a solid cube generating fluid domain corresponding to the unit cell having length and height equal to s (2.54 mm). An extended inlet ($0.2s$) and outlet ($0.6s$) length was also provided upstream and downstream of the unit cell. Uniform inlet velocity with constant inlet temperature was provided at the inlet plane while the outlet was set at zero-gauge pressure condition. Periodic boundary flow conditions were employed on the faces in y- and z- direction.

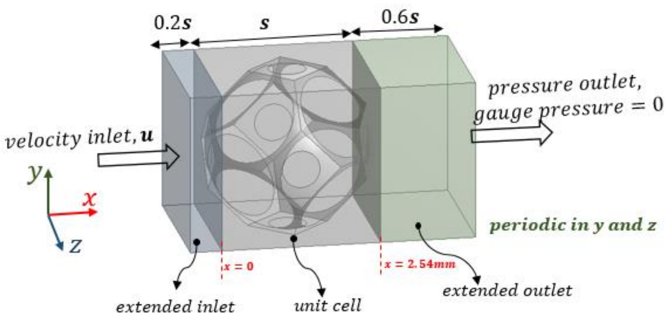

Figure 3.6 Fluid domain shown with the boundary conditions

The flow was not periodic in the streamwise direction (x). No slip-boundary condition was provided on the fibers. The interfacial heat transfer calculations reported in the present study corresponds to two fibers boundary conditions: constant heat flux ($q"$) and constant wall (fiber) temperature (T_w). The thermo-physical properties of air (working fluid) were evaluated at the inlet temperature and were assumed to be constant throughout the flow domain due to negligible temperature rise through the unit cell length.

3.4.2 Governing Equations

The inlet velocity range of 0.5 m/s to 2.3 m/s was investigated in the present study. Dybbs and Edwards [35] reported the flow transits from laminar to transitional regime in porous media at pore Reynolds number $(\mathrm{Re_d}/\varepsilon)\ \sim 300$. Considering the weighted average of the diameter of the circular openings of the TKD structure, the pore diameter was 1.0617 mm. The pore Reynolds number corresponding to maximum velocity investigated in the present study was ~170.The steady-state, three-dimensional and incompressible fluid flow was solved using the following laminar governing equations for mass, momentum, and energy:

Continuity equation:

$$\frac{\partial}{\partial x_i}(\rho v_i) = 0 \tag{3.5}$$

Momentum equation:

$$\frac{\partial}{\partial x_j}\left(\rho v_j v_i\right) = -\frac{\partial P}{\partial x_i} + \frac{\partial}{\partial x_j}\left(\mu \frac{\partial v_i}{\partial x_j}\right) \tag{3.6}$$

Energy equation:

$$\frac{\partial}{\partial x_i}\left(\rho v_i c_p T\right) = \frac{\partial}{\partial x_i}\left(\lambda \frac{\partial T}{\partial x_i}\right) \tag{3.7}$$

where $v, \rho, \mu, \lambda\ and\ c_p$ are the velocity, density, dynamic viscosity, thermal conductivity, and specific heat capacity of air, respectively.

3.4.3 Mesh generation and numerical procedure

Considering the complexity of four different unit cell geometries, an unstructured mesh strategy was adopted. The pore-level simulation studies present in the literature ([24, 26, 27, 28, 30, 32]) adopted the hybrid-unstructured meshing schemes. The CAD model was exported to the mesh generator module provided by ANSYS 2019 R2. Unstructured mesh comprising of tetrahedral elements was created for all the configurations, an example of *TKD* cell is provided in Fig. 3.7.

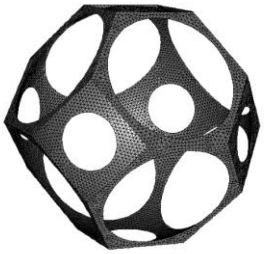

Figure 3.7 Tetrahedral mesh elements shown on *TKD* fibers

After meshing, the fluid domain was exported to Fluent module to solve the above-mentioned governing equations. SIMPLE scheme was adopted for pressure-velocity coupling. Second order upwind scheme was activated for discretizing momentum and energy equations. The relaxation factors were set as the default values of 0.3, 0.7 and 1 for pressure, momentum, and energy respectively. The convergence criterion for velocities and energy equation was set to the normalized residual values of 10^{-6} and 10^{-8} respectively.

3.5 Pressure drop and heat transfer calculations

The pressure gradient reported in this study is given as,

$$\frac{\Delta P}{s} = \frac{P_1 - P_2}{s} \tag{3.8}$$

where, P_1 and P_2 were the mean pressures at the entry and exit of the unit cell. The local interstitial heat transfer coefficient was analyzed for constant fiber temperature and heat flux. Local heat transfer coefficient was defined as following:

$$h(x, y, z) = \frac{q"(x, y, z)}{[T_w(x, y, z) - T_b\ (x)]} \tag{3.9}$$

where, h is the local heat transfer coefficient, $q"$ is the heat flux imposed on the fibers in constant flux case $(q"(x, y, z) = constant)$ and calculated from the numerical results in constant temperature boundary condition, T_w is the local wall temperature and T_b is the local bulk fluid temperature.

Average heat transfer coefficient ($\bar{h}_{sf}$) was obtained using:

$$\bar{h}_{sf} = \frac{q"}{\left[\frac{1}{A_{sf}} \iint T_w dA - \frac{1}{s} \int_0^s T_b\ (x) dx\right]} \tag{3.10}$$

where, $(1/A_{sf}) \iint T_w\, dA$ is the area averaged fiber wall temperature, $(1/s) \int_0^s T_b(x) dx,$ is the length-averaged bulk flow temperature. The average heat transfer coefficient ($\bar{h}_{sf}$) mentioned above accounts for the bulk variations in the temperature field. Another methodology adopted for calculating heat transfer coefficient ($\bar{\bar{h}}_{sf}$) is by calculating the local heat transfer coefficient using $Eq.$ 3.9 and then averaging it over the entire fiber wall area, as following:

$$\bar{\bar{h}}_{sf} = \frac{1}{A_{sf}} \iint h\ (x, y, z) dA \tag{3.11}$$

3.6 Grid independence study

To ensure that the reported heat transfer and pressure drop results were independent of the mesh, three different grid schemes, referred to as coarse, medium, and fine, were evaluated for each configuration and presented in Table 3.2. The interstitial heat transfer coefficient results provided in the table correspond to the constant fiber heat flux boundary condition. The percentage difference of the coarse and medium grid with respect to the fine mesh is given in Table 3.3. The deviation of the pressure gradient and heat transfer coefficient corresponding to medium mesh was

Table 3.2 Grid independence study

$Unit\ cell\ topology$	$Grid$ 1 (coarse)			$Grid$ 2 (medium)			$Grid$ 3 (fine)		
	$Total\ Elements$	$\frac{\Delta P}{s}$ (Pa/mm)	$\bar{h}_{sf}$ (W/m^2K)	$Total\ Elements$	$\frac{\Delta P}{s}$ (Pa/mm)	$\bar{h}_{sf}$ (W/m^2K)	$Total\ Elements$	$\frac{\Delta P}{s}$ (Pa/mm)	$\bar{h}_{sf}$ (W/m^2K)
$Tetrakaidecahedron$	261, 085	1.861	273.105	507,263	1.911	272.970	731,551	1.915	272.361
$Cube$	260, 765	1.03	263.324	500,887	1.036	262.696	752,466	1.043	261.369
$FD - Cube$	225,099	1.429	322.622	487,185	1.507	323.102	685,130	1.535	323.918
$Octet$	254,153	1.796	518.995	511,985	1.955	517.438	872,995	1.966	516.903

Table 3.3 Percentage deviation of coarse and medium grids with respect to the fine grids

$Parameter$	Tetrakaidecahedron		Cube		FD-Cube		Octet	
	$Grid$ 1 ($coarse$)	$Grid$ 2 ($medium$)	$Grid$ 1 ($coarse$)	$Grid$ 2 ($medium$)	$Grid$ 1 ($coarse$)	$Grid$ 2 ($medium$)	$Grid$ 1 ($coarse$)	$Grid$ 2 ($medium$)
$\frac{\Delta P}{s}$	2.90	0.21	1.26	0.68	7.42	1.86	9.47	0.56
$\bar{h}_{sf}$	-0.22	-0.27	-0.7	-0.5	0.40	0.25	-0.40	-0.10

less than 1% relative to the fine mesh for all the configurations (except for the pressure gradient deviation in *FD-Cube*). Apart from these global parameters, the local velocity variation for each mesh grid is also presented in Fig. 3.8 along two lines drawn in streamwise direction (parallel to the fluid flow). Line1 was drawn at the centerline of the unit cell and Line2 was drawn at the quarter-span of the cell height from the Line 1. Considering the acceptable differences in the global parameters $(\Delta P/s) and\ \bar{h}_{sf}$, and the close agreement of local velocity profiles drawn at Lines 1 and 2, between medium and fine grid schemes, the medium grid scheme was adopted for further computations to maintain a balance between cost and accuracy. The local velocity profiles for Line 1 and Line 2 are discussed further in the next section.

3.7 Results and discussion

This section presents a discussion on the flow-field, pressure drop as well as volumetric Nusselt number for the four unit cell configurations.

3.7.1 Flow field and pressure drop

The normalized velocity (u_{local}/u) contours, superimposed by surface streamlines, for all the configurations are shown in Fig. 3.9, where ‘u’ is the inlet velocity of 2.3 m/s. Planes P1 and P2 are drawn perpendicular and parallel to the flow, respectively, and pass through the centerline of the cube circumscribing the unit cells. Among all the representative planes shown in Fig. 3.9, *TKD* structure had the maximum local velocity values in both directions (y-z and x-z). As the fluid impinged and stagnated on the quadrilateral face of the *TKD*, it accelerated through the narrow pore area on the face (high velocity region on plane P2). Low velocity wake regions were observed downstream of the fibers walls. These regions are characterized by strong recirculatory zones as shown by secondary flows on plane P1.

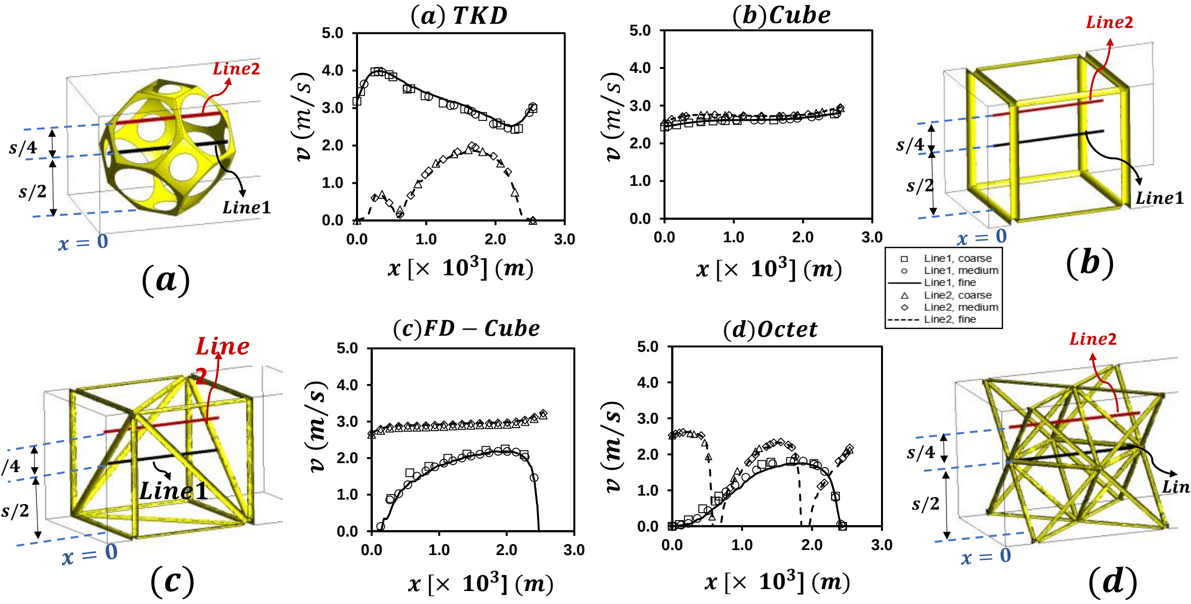

Figure 3.8 Local velocity variation along lines drawn along the streamwise direction parallel to the fluid flow in (a) *TKD*, (b) *Cube*, (c) *FD-Cube*, (d) *Octet* configurations

The velocity plot along Line1 in Fig. 3.8(a) showed increasing trend in the beginning, reached a peak value of about 4 m/s and then decreased until $x/s \sim 1$, from where the flow encountered the small pore on the quadrilateral face again. The peak velocity observed at this location was much lower than that observed near the inlet face. The development of the velocity profile along Line2 (also shown in Fig. 3.9 at plane P2) was inhibited by the large wake regions downstream of the fiber walls. The effect of the wake region is reflected as lower velocity values along Line2 in Fig. 3.8(a) up to a quarter span in streamwise direction (i.e.$x/s \sim 0.25$). There was a steady increment in the fluid velocity till$x/s \sim 0.65$, beyond which it started decreasing until it stagnated on the rear fiber walls.

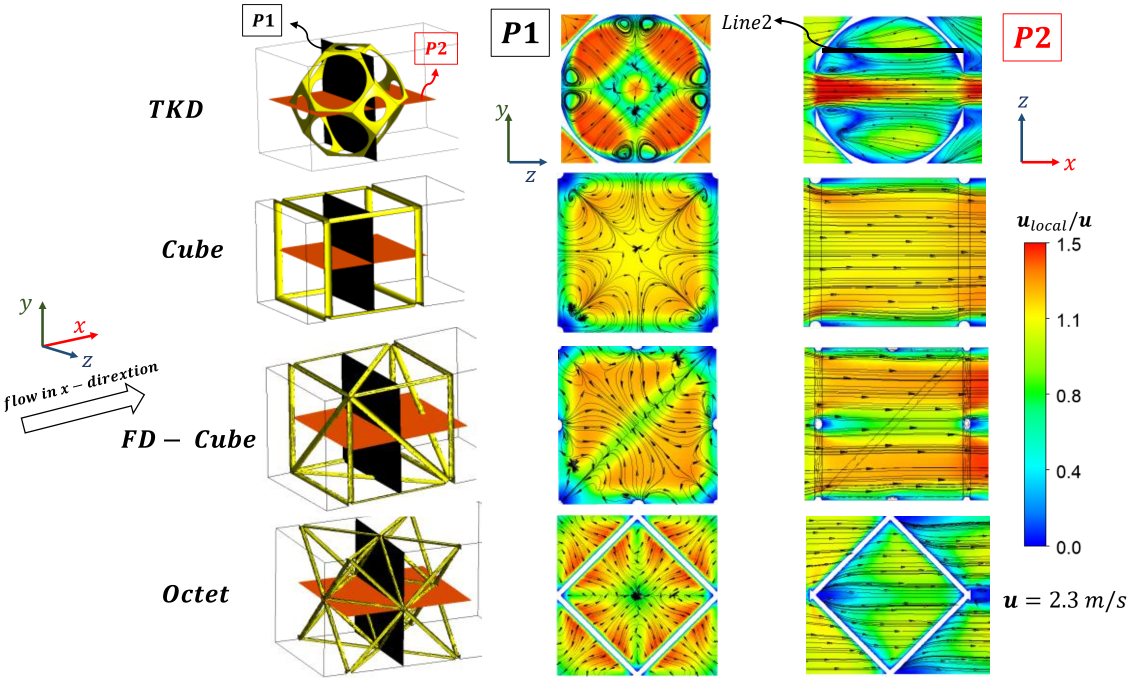

Figure 3.9 Normalized velocity contours superimposed by surface streamlines on plane (P1) perpendicular to the flow direction and plane (P2) parallel to the flow direction for inlet velocity (u) equal to 2.3 m/s

The flow dynamics in *Cube* and *FD-Cube* was relatively less complicated as compared to *TKD* because of simpler fiber connections. The presence of face diagonal fibers near the inlet of the *FD-Cube* disturbed the regular flow pattern otherwise observed in *Cube* at plane P1. The effect of extra fibers connectivity at the face diagonal was realized all along the unit cell as the higher velocity regions were divided into two triangular zones at the plane P1. The plane P2 demonstrated fluid stagnation and concentrated wake region behind the fibers. The flow in Cube was symmetric about the center whereas it was symmetric about the diagonal in FD-Cube. The face-diagonal fibers resulted in two distinct streamwise stripes of higher velocity region on P2. The velocity variation (Fig. 3.8c) at Line1 increased from near-zero at the face diagonal fiber, all along the unit cell length and dropped significantly near $x/s \sim 1$due to upstream effects of the rear face-diagonal fibers, consequently bringing it to zero on the walls.

Octet unit cell configuration was the most complex topology investigated in this study. The local velocity values at a plane perpendicular to the flow (P1) were relatively higher as compared to *Cube* and *FD-Cube*, but they were significantly lower than the *TKD* structure. For *Cube* and *FD-Cube* configurations, the fiber connectivity was present only along the faces of the cubic unit cell, whereas in the case of *Octet*, a complex network of these fibers was present within the unit cell cubic volume as well. Therefore, the flow pattern observed at plane P1 and P2 in *Cube* and *FD-Cube* configurations were influenced by the fibers present at the edges or at the front face of the unit cell cube but the flow dynamics in case of *Octet* configuration was influenced by upstream fibers as well as by the ones present on the representative planes. As the flow moved over the fibers, the lateral acceleration of the fluid was observed perpendicular to the main flow direction (plane P1) but strong wake regions were present in the flow direction (plane P2). The rate of velocity increment at the beginning of the unit cell was higher for *FD-Cube* as compared to *Octet* configuration. This can be concluded by observing the slopes of the velocity line plots in Fig. 3.8. Flow development along Line2 was slower in *Octet* configuration as compared to *FD-Cube* because of the stronger and widespread wake region downstream of the fiber junction present at the face center of the unit cell cube.

The configurations investigated in the present study were periodic in directions normal to the flow. Thus, the flow and thermal characteristics were governed by the impingement effect of the oncoming flow. A comparison with the configuration periodic in x-, y- and z- direction is presented in Fig. 3.10 for inlet velocity of 1 m/s. While simulating fully periodic unit cells, mass flow rate corresponding to 1m/s was specified and the local velocity values were normalized by the average velocities at the inlet faces of each unit cell topology. The velocity profile at the inlet faces of the streamwise periodic unit cell showed contrast to the otherwise non-periodic cells. This apparent difference resulted due to developed velocity profiles in cells periodic in all three directions, where the localized velocity enhancements could be observed due to fluid-metal structure interactions.

The flow physics explains the pressure drop and heat transfer characteristics of any geometrical configuration subjected to the convective flows. The *TKD* structure had pressure drop per unit length of ~ 0.55 to 25.12 (Pa/mm) for velocity range of 0.5 to 2.3 m/s, which were in close agreement with Bai and Chung [28] for similar geometrical parameters (Fig. 3.11.a).

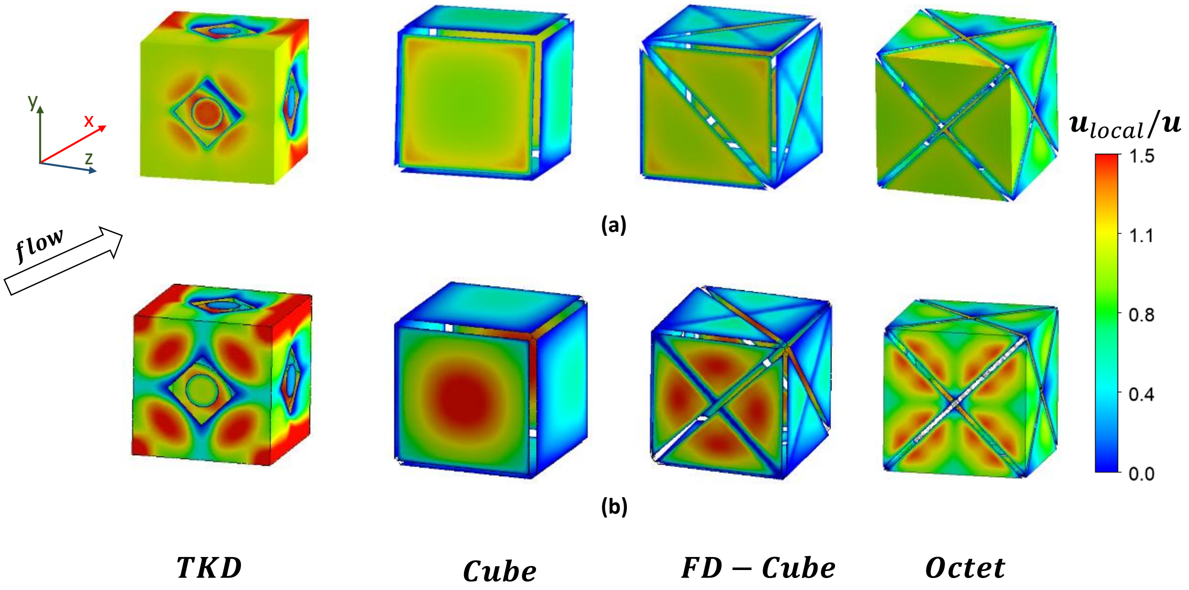

Figure 3.10 Normalized velocity contours on the unit cell faces for (a) flow periodic in y- and z- direction, (b) flow periodic in x-, y- and z- direction at mass flow rate corresponding to inlet velocity of 1 m/s

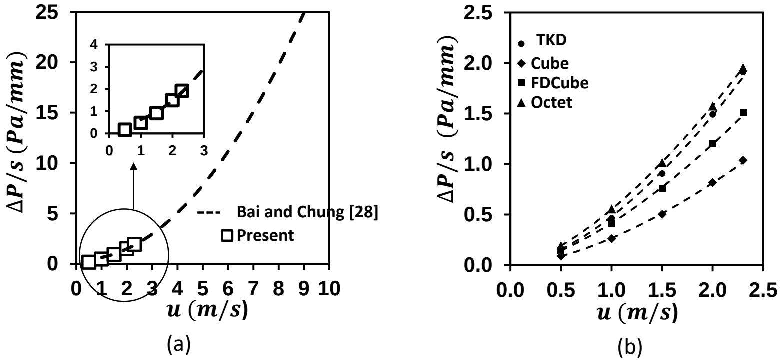

Figure 3.11 (a) Pressure drop validation with Bai and Chung [28], (b) Pressure drop comparison of four unit cell configurations in the present study

Among the four different unit cell configurations, *Octet* had the highest pressure drop, closely followed by *TKD*. The *FD-Cube* and *Cube* configurations had the least flow losses resulting in lower pressure drops. The flow dynamics presented on plane P2 (Fig. 3.9) had major influence in determining the flow resistance because the wake formation behind the fibers take place in direction parallel to the flow. *Octet* configuration had the highest flow resistance, which was apparent from strong wake formation and slow flow development in streamwise direction. Unlike *Octet*, *Cube* and *FD-Cube* did not have any fibers within the cell volume, therefore there is relatively less flow resistance leading to lower pressure drops. *Octet* configuration had 1.2-, 1.3- and 2.15-times higher pressure drop than *TKD*, *FD-Cube* and *Cube* respectively.

3.7.2 Interstitial heat transfer coefficient

Detailed heat transfer coefficient on the fiber walls have been shown in Fig. 3.12 for the constant heat flux type boundary condition (Eq. 3.9). In *TKD*, the flow stagnation on the fibers walls directly facing the incoming flow resulted in enhanced local heat transfer. The curved inner walls of the quadrilateral faces had relatively lower heat transfer as these regions were in the wake of the upstream fibers.

The fibers on the face near the inlet in *Cube* and *FD-Cube* configuration had the highest heat transfer because of direct impingement of the incoming flow. At a fixed porosity, the *Octet* cell yielded more instances of flow impingement leading to higher stagnation heat transfer, compared to other three topologies. Further, the reported heat transfer is only accounting for the convective heat transfer coefficient as the thermal boundary conditions were fixed *a priori*, be it a constant wall heat flux or constant wall temperature. In conjugate heat transfer configurations, the octet topology will perform even better as it had the maximum surface area through which the flow can interact, and this coupled with high local interstitial heat transfer coefficient would result in enhanced heat dissipation. In all the four topologies, the primary mechanism of heat transfer enhancement was the stagnation type for the low velocity range investigated here.

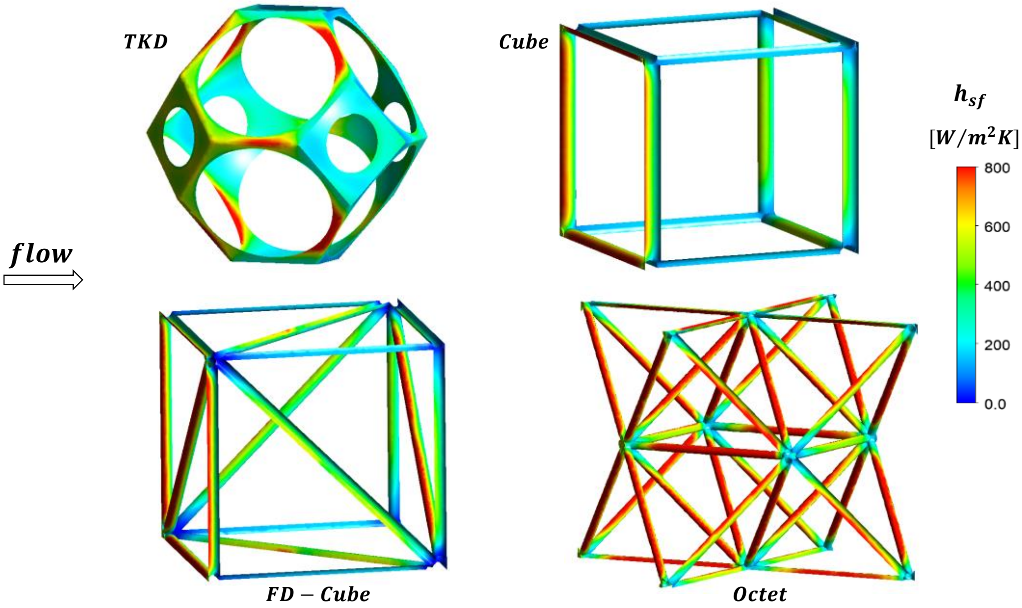

Figure 3.12 Interfacial heat transfer coefficient shown on fiber walls for constant wall flux boundary condition

3.7.2.1 Interstitial heat transfer coefficient prediction validation

(a) Validation for *Cube, FD-Cube* and *Octet*

Following discussion is focused on the heat transfer prediction validation. Since the structures presented in this paper are new to the DNS-based studies (except *TKD*, whose heat transfer validation is presented later), the local fiber-scale validation methodology has been adopted. The fibers considered in the new unit cell topologies investigated in the present study were of circular cross-section (except *TKD*). The flow dynamics over these fibers can be compared to crossflow over circular cylinders. In order to validate the average heat transfer coefficient measurements, circular cylinders corresponding to diameter of 0.2 mm and 0.084 mm were simulated in a crossflow. The diameters chosen for simulation corresponded to the *Cube* and *Octet* configurations' fiber diameters which were representative of the upper and lower limits of the fiber diameters analyzed in this paper.

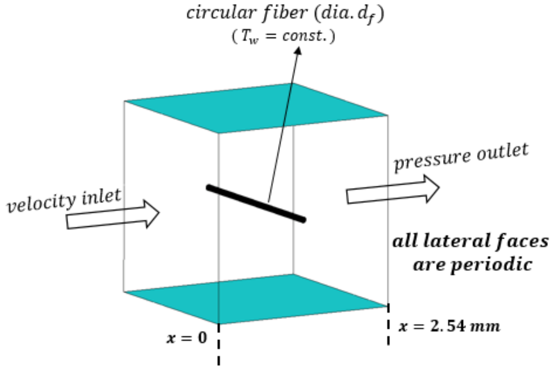

Figure 3.13 Computational domain for simulation of circular cylinder in cross flow

A cylinder (diameter, d_f) was placed at the center of a unit cell which was a cube of edge length 2.54 mm. The extended inlet and outlet were provided to replicate the overall dimensions of the fluid domain shown in Fig. 3.6 (not shown in Fig. 3.13 for simplification). A uniform inlet velocity and uniform inlet temperature was provided at the inlet and uniform wall temperature (T_w) was imposed on the cylinder wall. The average heat transfer coefficient $\left(\bar{h}_{d_f}\right)$ based on cylinder diameter was calculated using,

$$\bar{h}_{d_f} = \frac{q"}{(T_w - T_{in})} \tag{3.12}$$

The above heat transfer coefficient was normalized ($\overline{Nu}_{d_f} = \bar{h}_{d_f} d_f / k_f$) to allow comparison with Churchill and Bernstein [36] shown below,

$$\overline{Nu}_{d_f} = 0.3 + \frac{0.62\,Re_{d_f}^{1/2}Pr^{1/3}}{[1+(0.4/Pr)^{2/3}]^{1/4}}\left[1+\left(\frac{Re_{d_f}}{282{,}000}\right)^{5/8}\right]^{4/5} \tag{3.13}$$

where, Re_{d_f} $(= \boldsymbol{u}d_f/\vartheta)$ is fiber diameter-based Reynolds number, Pr is the air Prandtl number and λ is the thermal conductivity of air. The thermo-physical properties of air were calculated at the film temperature $((T_w + T_{in})/2)$. The above correlation is valid for $RePr > 0.2$ and constant wall temperature thermal boundary condition. The Reynolds number range for present simulations (considering both the diameters) varied between 2.5 and 30. The average heat transfer coefficient obtained from the crossflow simulations are presented in Fig. 3.14. The maximum deviation from correlation was within 6% for the range of velocities investigated.

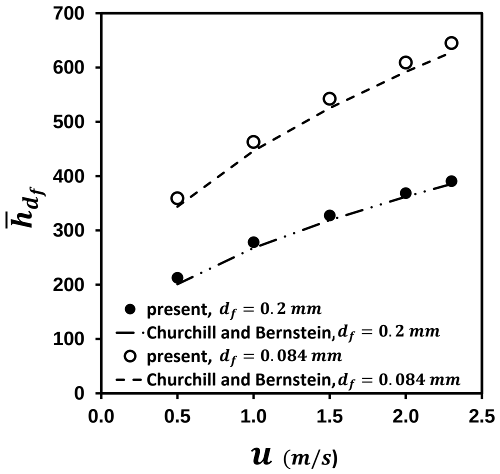

Figure 3.14 Comparison of heat transfer coefficient results with the Churchill and Bernstein correlation

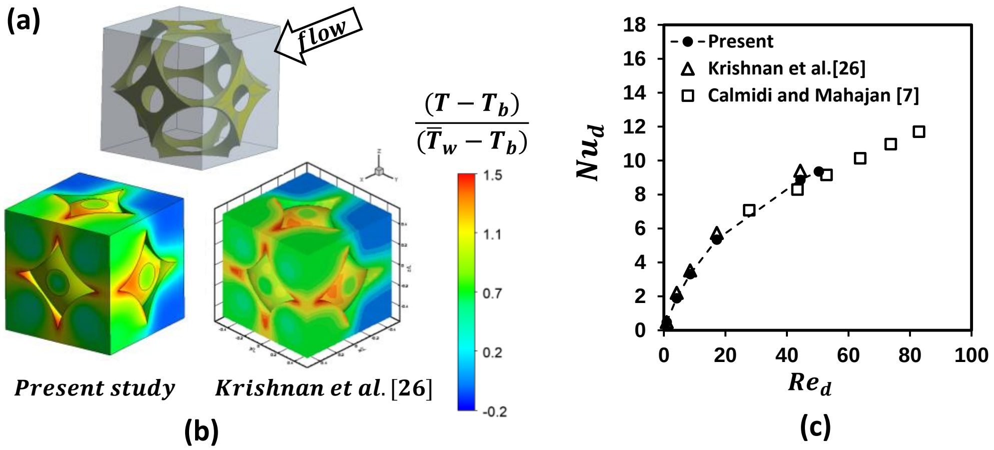

Figure 3.15 (a) BCC geometry adopted for simulations by Krishnan et al. [26], (b) comparison of normalized temperature contours on the faces of unit cell and fiber walls at $Re_d = 50$, (c) Nusselt number (based on pore diameter) validation with [7] and [26]

(b) Validation for *TKD* structure

Since the generation procedure of *TKD* led to sharp edges and triangle-like fibers cross-section, the validation of the structure was performed for fully-periodic BCC cell (ϵ ~0.968) shown in Fig. 3.15(a), same as the one considered in the study of Krishnan et al. [26]. The calculation methodology is elaborated in [26] and is not presented here in the interest of brevity. Figure 3.15(b) compares the normalized temperature contours ($\overline{T}_W$ and T_b are average fiber wall temperature and upstream bulk temperature respectively) on the faces of the unit cell and fiber walls at pore Reynolds number ~50 obtained in the present analysis with that provided in [26]. Figure 3.15(c) shows the comparison of the Nusselt number (based on pore-diameter) for BCC structure with the results presented in literature [7, 26]. The fair qualitative and quantitative agreement of the heat transfer characteristics of the BCC structure with the results of [7, 26] ensures the fidelity of the results obtained in the present study for *TKD* structure.

3.7.3 Volumetric Nusselt number

Morphological parameters such as porosity, pore diameter, fiber diameter, cell diameter and surface area-to-volume ratio are generally used to normalize the heat transfer coefficients. In the present study, the comparison of the thermal performance for different structures is presented using volumetric Nusselt number given as,

$$Nu = \frac{h_{sf}\ (d_c/\epsilon)}{\lambda} \tag{3.14}$$

where, h_{sf} is the interstitial heat transfer coefficient and d_c is the cell diameter. Characteristic length of d_c/ϵ was employed by Iasiello et al. [32] to normalize heat transfer coefficient. The cell diameter in their study was defined as the diameter of the largest sphere inscribed in a unit cell. In the present study, the equivalent cell diameter is the unit cell length (2.54 mm). Based on the arguments provided by [32], the specification of the unit cell lengths is easier as compared to pore or fiber diameters, something which can be universally adapted. It is to be noted that the analysis provided by [32] is for the stochastic metal foams. The customized cellular structures investigated in the present study had circular fibers and different opening areas to the incoming fluid, thus a single definition for all the structures was not straightforward. Moreover, the comparison is drawn with the conventional *TKD* structure, the fibers for which were not circular. In the view of the above arguments, the usage of d_c/ϵ as the characteristic length seemed to be the most appropriate. Volumetric heat transfer coefficient is defined as following:

$$Nu_v = \frac{h_v\ (d_c/\epsilon)^2}{\lambda} = \frac{h_{sf}\ (S/\forall)\ (d_c/\epsilon)^2}{\lambda} \tag{3.15}$$

where h_v is the volumetric heat transfer coefficient given by $h_v = h_{sf}(S/\forall)$. The surface area-to-volume ratio ($S/\forall$) for different structures is provided in Table 1. The volumetric Nusselt numbers corresponding to the $Eq. 3.10$ and $Eq. 3.11$ are denoted by $\overline{Nu_v}$ and $\overline{\overline{Nu_v}}$ respectively. A Reynolds number based on the same length scale is defined as:

$$Re_c = \frac{\boldsymbol{u}\,(d_c/\epsilon)}{\vartheta} \tag{3.16}$$

Figure 3.16 shows volumetric Nusselt number as a function of cell Reynolds number. The volumetric Nusselt number ($\overline{Nu_v}$) based on average heat transfer coefficient, $\bar{h}_{sf}$ ($Eq. 3.10$) was highest for *Octet*, followed by *TKD, FD-Cube* and *Cube*, respectively. For the constant heat flux boundary condition, the volumetric Nusselt Number ($\overline{Nu_v}$) of *Octet* configuration was 1.63 to 1.89, 2.31 to 2.45 and 4.17 to 4.68 times higher than *TKD*, *FD-Cube* and *Cube,* respectively. For constant temperature boundary condition, the *Octet* configuration provided 1.8 to 1.9, 2.18 to 2.25, 4.59 to 4.62 times heat transfer enhancement than the *TKD*, *FD-Cube* and *Cube* configurations respectively. The volumetric Nusselt number ($\overline{Nu_v}$) values were higher for the constant temperature wall boundary condition compared to the constant heat flux condition.

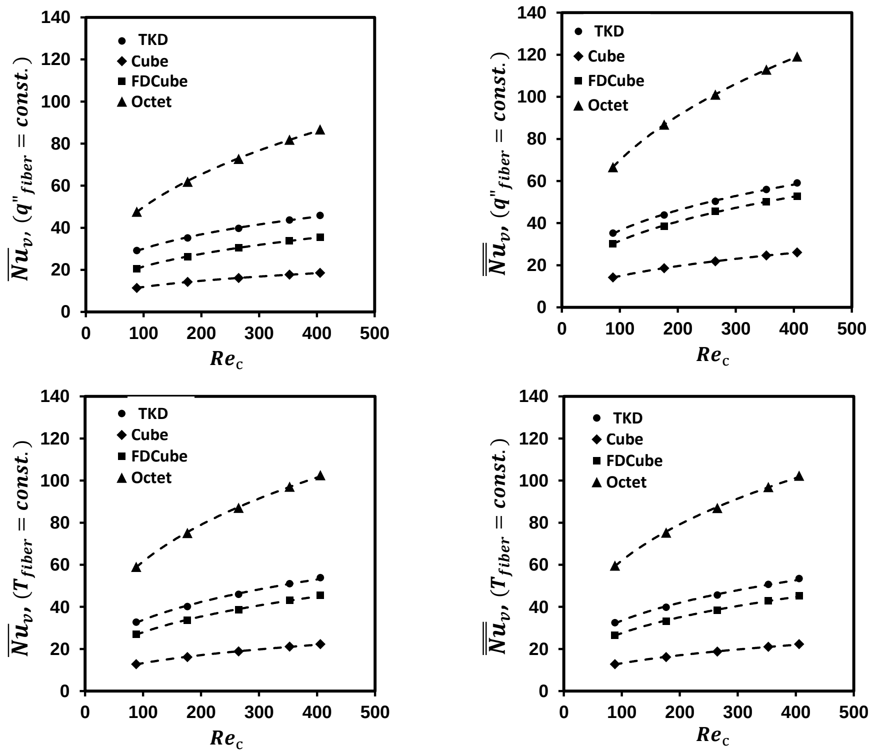

Figure 3.16 Volumetric Nusselt number for different unit cell configurations and wall boundary conditions

The volumetric Nusselt number ($\overline{\overline{\overline{Nu_v}}}$) based on interfacial heat transfer coefficient ($\overline{\overline{h}}_{sf}$)obtained by area averaging the local heat transfer coefficient over the fiber walls ($Eq. 3.11$) showed similar trend to $\overline{Nu_v}$. For constant heat flux boundary condition, the Nusselt numbers coefficient calculated from both the methodologies ($\overline{h}_{sf}$ and $\overline{\overline{h}}_{sf}$) showed significant difference for *Octet, TKD* and *FD-Cube* but almost similar values were exhibited for constant temperature boundary condition. The value of $\overline{\overline{\overline{Nu_v}}}$ for *Octet* was 1.83 to 2.02, 2.25 to 2.26, 4.59 to 4.69 times higher than *TKD, FD-Cube* and *Cube* respectively. These enhancements were similar for both heat flux and constant temperature boundary condition.

Above results of volumetric Nusselt number are summarized in the form of a correlation, $Nu_v = a\, Re_c^b Pr^{0.4}$, where, $\left(\bar{a}, \bar{b}\right)$ and $\left(\bar{\bar{a}}, \bar{\bar{b}}\right)$ are coefficients corresponding to $\overline{Nu}_v$ and $\overline{\overline{Nu}}_v$, respectively and subscripts q'' and T_w denote the constant heat flux and constant temperature boundary conditions, respectively. The correlations in the present study are reported for $88 \le Re_c(\boldsymbol{u}\, d_c/\epsilon\vartheta) \le 405$. These correlation coefficients are summarized in Table 3.4.

Table 3.4 Correlation coefficients for $Nu_v = a\, Re_c^b Pr^{0.4}$

$Configuration$	$\bar{a}_{q''}$	$\bar{b}_{q''}$	$\bar{\bar{a}}_{q''}$	$\bar{\bar{b}}_{q''}$	$\bar{a}_{T_w}$	$\bar{b}_{T_w}$	$\bar{\bar{a}}_{T_w}$	$\bar{\bar{b}}_{T_w}$
TKD	8.8613	0.2955	8.8375	0.3382	8.6688	0.3256	8.5427	0.3268
$Cube$	3.1733	0.3168	2.7047	0.4001	2.8424	0.3648	2.795	0.3675
$FD-Cube$	4.7926	0.3566	6.6922	0.3673	6.6330	0.3425	6.3060	0.3502
$Octet$	9.3982	0.3926	13.928	0.3806	13.412	0.3611	13.991	0.3536

3.8 Conclusions

The present study reports the flow dynamics, pressure drop and interstitial heat transfer characteristics of four different unit cell configurations, viz. *Tetrakaidecahedron (TKD)*, *Cube*, *FD-Cube* and *Octet*. The detailed geometrical construction of the *TKD* unit cell is described and the chosen porosity of 0.986 corresponding to $\alpha = 0.0275$ is explained. For other topologies, the porosity was held constant, which resulted in different fiber diameters. The two pairs of opposite faces parallel to fluid flow were set as periodic and the planes orthogonal to the flow were set as velocity inlet and zero gage-pressure outlet, respectively. This unit cell study is representative of reticulated foam structures where the thickness in the flow direction is equivalent to one unit cell length, or the crossflow is allowed to interact with only one unit cell in the streamwise direction.

Octet configuration had the highest pressure drop among all the configurations and *Cube* had the lowest pressure drop. The interstitial heat transfer coefficient was calculated for two thermal boundary conditions on the fiber walls, viz. constant heat flux and constant wall temperature. The volumetric Nusselt number was found to be the highest for *Octet* unit cell, followed by *TKD*, *FD-Cube* and *Cube*. Impingement effect of the approaching flow on the fiber walls was the major factor for local enhancement of interstitial heat transfer coefficient for all the configurations. *Octet* unit cell topology seems promising when reticulated in three dimensions, in terms of enhanced heat dissipation at relatively lower increment in pumping power penalty.

NOMENCLATURE

d_f	fiber diameter
h_{sf}	interfacial heat transfer coefficient
K	permeability
Nu_d	Nusselt number based on pore diameter
Nu	mean convective Nusselt number
Nu_v	volumetric Nusselt number
Pr	Prandtl number
q''	heat flux on the fiber walls
Re_c	Reynolds number based on cell diameter (unit cell length)
Re_d	Reynolds number based on pore diameter
Re_{df}	Reynolds number based on fiber diameter
s	unit cell length
T_w	temperature of the fiber walls
T_b	bulk fluid temperature
T_{in}	uniform inlet temperature
$\boldsymbol{u}$	inlet velocity of the fluid
$\forall_s$	total fiber volume in a unit cell
$\forall_{total}$	total volume of the unit cell
ΔP	pressure drop across unit cell

Greek symbols

ρ	density of air
μ	dynamic viscosity of air
ϑ	kinematic viscosity of air
λ	thermal conductivity of air
ε	porosity

REFERENCES

[1] Hwang, J.J., Hwang, G.J., Yeh, R.H. and Chao, C.H., 2001. Measurement of interstitial convective heat transfer and frictional drag for flow across metal foams. J. Heat Transfer, 124(1), pp.120-129.

[2] Younis, L.B. and Viskanta, R., 1993. Experimental determination of the volumetric heat transfer coefficient between stream of air and ceramic foam. International journal of heat and mass transfer, 36(6), pp.1425-1434.

[3] Ichimiya, K., 1999. A new method for evaluation of heat transfer between solid material and fluid in a porous medium. Journal of heat transfer, 121(4), pp.978-983.

[4] Hsieh, W.H., Wu, J.Y., Shih, W.H. and Chiu, W.C., 2004. Experimental investigation of heat-transfer characteristics of aluminum-foam heat sinks. International Journal of Heat and Mass Transfer, 47(23), pp.5149-5157.

[5] Mancin, S., Zilio, C., Diani, A. and Rossetto, L., 2013. Air forced convection through metal foams: Experimental results and modeling. International Journal of Heat and Mass Transfer, 62, pp.112-123.

[6] Paek, J.W., Kang, B.H., Kim, S.Y. and Hyun, J.M., 2000. Effective thermal conductivity and permeability of aluminum foam materials. International Journal of Thermophysics, 21(2), pp.453-464.

[7] Calmidi, V.V. and Mahajan, R.L., 2000. Forced convection in high porosity metal foams. J. Heat Transfer, 122(3), pp.557-565.[8] Calmidi, V.V. and Mahajan, R.L., 1999. The effective thermal conductivity of high porosity fibrous metal foams. Journal of Heat Transfer, 121(2).

[9] Bhattacharya, A., Calmidi, V.V. and Mahajan, R.L., 2002. Thermophysical properties of high porosity metal foams. International Journal of Heat and Mass Transfer, 45(5), pp.1017-1031.

[10] Zhao, C.Y., Lu, T.J., Hodson, H.P. and Jackson, J.D., 2004. The temperature dependence of effective thermal conductivity of open-celled steel alloy foams. Materials Science and Engineering: A, 367(1-2), pp.123-131.

[11] Nithyanandam, K. and Mahajan, R.L., 2018. Evaluation of metal foam based thermoelectric generators for automobile waste heat recovery. International Journal of Heat and Mass Transfer, 122, pp.877-883.

[12] Feng, S., Shi, M., Li, Y. and Lu, T.J., 2015. Pore-scale and volume-averaged numerical simulations of melting phase change heat transfer in finned metal foam. International Journal of Heat and Mass Transfer, 90, pp.838-847.

[13] Yang, X., Bai, Q., Guo, Z., Niu, Z., Yang, C., Jin, L., Lu, T.J. and Yan, J., 2018. Comparison of direct numerical simulation with volume-averaged method on composite phase change materials for thermal energy storage. Applied energy, 229, pp.700-714.

[14] Hu, X., Wan, H. and Patnaik, S.S., 2015. Numerical modeling of heat transfer in open-cell micro-foam with phase change material. International Journal of Heat and Mass Transfer, 88, pp.617-626.

[15] Tian, Y. and Zhao, C.Y., 2011. A numerical investigation of heat transfer in phase change materials (PCMs) embedded in porous metals. Energy, 36(9), pp.5539-5546.

[16] Banhart, J., 2000. Manufacturing routes for metallic foams. Jom, 52(12), pp.22-27.

[17] Lord Kelvin (Sir William Thomson), 1887, "On the Division of Space With Minimum Partitional Area," Acta Math., 11(1–4), pp. 121–134.19. Plateau, J., 1873. Statique expérimentale et théorique des liquides soumis aux seules forces moléculaires (Vol. 2). Gauthier-Villars.

[18] Plateau, J., 1873. Statique expérimentale et théorique des liquides soumis aux seules forces moléculaires (Vol. 2). Gauthier-Villars.

[19] Weaire, D. and Phelan, R., 1994. A counter-example to Kelvin's conjecture on minimal surfaces. Philosophical Magazine Letters, 69(2), pp.107-110.

[20] Brakke, K.A., 1992. The surface evolver. Experimental mathematics, 1(2), pp.141-165.

[21] Cunsolo, S., Iasiello, M., Oliviero, M., Bianco, N., Chiu, W.K. and Naso, V., 2016. Lord Kelvin and Weaire–Phelan Foam Models: Heat Transfer and Pressure Drop. Journal of Heat Transfer, 138(2), p.022601.

[22] Simpleware Ltd, 2012, Exeter, UK.

[23] Boomsma, K. and Poulikakos, D., 2001. On the effective thermal conductivity of a three-dimensionally structured fluid-saturated metal foam. International Journal of Heat and Mass Transfer, 44(4), pp.827-836.

[24] Boomsma, K., Poulikakos, D. and Ventikos, Y., 2003. Simulations of flow through open cell metal foams using an idealized periodic cell structure. International Journal of Heat and Fluid Flow, 24(6), pp.825-834.

[25] Boomsma, K. and Poulikakos, D., 2001. The effects of compression and pore size variations on the liquid flow characteristics in metal foams. J. Fluids Eng., 124(1), pp.263-272.

[26] Krishnan, S., Murthy, J.Y. and Garimella, S.V., 2006. Direct simulation of transport in open-cell metal foam. Journal of heat transfer, 128(8), pp.793-799.

[27] Kopanidis, A., Theodorakakos, A., Gavaises, E. and Bouris, D., 2010. 3D numerical simulation of flow and conjugate heat transfer through a pore scale model of high porosity open cell metal foam. International Journal of Heat and Mass Transfer, 53(11-12), pp.2539-2550.

[28] Bai, M. and Chung, J.N., 2011. Analytical and numerical prediction of heat transfer and pressure drop in open-cell metal foams. International Journal of Thermal Sciences, 50(6), pp.869-880.

[29] Leong, K.C. and Jin, L.W., 2006. Effect of oscillatory frequency on heat transfer in metal foam heat sinks of various pore densities. International journal of heat and mass transfer, 49(3-4), pp.671-681.

[30] Diani, A., Bodla, K.K., Rossetto, L. and Garimella, S.V., 2015. Numerical investigation of pressure drop and heat transfer through reconstructed metal foams and comparison against experiments. International Journal of Heat and Mass Transfer, 88, pp.508-515.

[31] Dixit, T. and Ghosh, I., 2018. Simulation intricacies of open-cell metal foam fin subjected to convective flow. Applied Thermal Engineering, 137, pp.532-544.

[32] Iasiello, M., Cunsolo, S., Bianco, N., Chiu, W.K.S. and Naso, V., 2017. Developing thermal flow in open-cell foams. International Journal of Thermal Sciences, 111, pp.129-137.

[33] Ekade, P. and Krishnan, S., 2019. Fluid flow and heat transfer characteristics of octet truss lattice geometry. International Journal of Thermal Sciences, 137, pp.253-261.

[34] Egan, P.F., Gonella, V.C., Engensperger, M., Ferguson, S.J. and Shea, K., 2017. Computationally designed lattices with tuned properties for tissue engineering using 3D printing. PloS one, 12(8), p.e0182902.

[35] Dybbs, A. and Edwards, R.V., 1984. A new look at porous media fluid mechanics—Darcy to turbulent. In Fundamentals of transport phenomena in porous media (pp. 199-256). Springer, Dordrecht.

[36] Churchill, S.W. and Bernstein, M., 1977. A correlating equation for forced convection from gases and liquids to a circular cylinder in crossflow.

CHAPTER IV

NUMERICAL INVESTIGATION ON CONJUGATE HEAT TRANSFER IN OCTET-SHAPE-BASED SINGLE UNIT CELL THICK METAL FOAM[3]

Abstract

Present study reports flow and thermal transport characteristics of metal-foam based on Octet-shaped unit cell (porosity~0.97) for electronic cooling application with water as the working fluid. Conjugate simulations were carried out on a single cell thick lattice frame comprising of four consecutive connected unit cells in the streamwise direction. Simulations were performed for flow velocity range of 2 - 8 cm/s with the substrate subjected to a heat flux of 10 $\mathrm{W/cm^2}$, for two different solid-phases corresponding to solid-to-fluid thermal conductivity ratios ($\mathrm{k_s/k_f}$) of 37 and 288. A control-volume-based energy balance method was adopted for calculation of global and cell-based convective heat transfer coefficient in the conjugate simulations, where the global heat transfer coefficient was ~2,900 $\mathrm{W/m^2K}$ for $\mathrm{k_s/k_f \sim 288}$ and ~2,100 $\mathrm{W/m^2K}$ for $\mathrm{k_s/k_f \sim 37}$, both for flow velocity of 8 cm/s. The cell-based heat transfer coefficient showed a sharp declining trend typical of developing flow. The interfacial heat transfer coefficient ($\mathrm{h_{sf}}$) on the fibers and the substrate-endwall was also obtained through separate simulations imposing constant heat flux and constant temperature boundary conditions on the walls. The averaged $\mathrm{h_{sf}}$ on fiber walls and

---

[3] Kaur, I. and Singh, P., 2021. Numerical investigation on conjugate heat transfer in octet-shape-based single unit cell thick metal foam. International Communications in Heat and Mass Transfer, 121, p.105090. doi: 10.1016/j.icheatmasstransfer.2020.105090

substrate-endwall was ~8,700 $\mathrm{W/m^2K}$ and ~2,000 $\mathrm{W/m^2K}$, respectively, corresponding to average flow velocity of 8 cm/s.

4.1 Introduction

Miniaturization of high-performance electronic equipment results high power density and hence high heat generation per unit volume [1]. The rapidly increasing power density of miniaturized electronic packages pose serious thermal management challenges. With local heat fluxes as high as ~300 $\mathrm{W/cm^2}$, it is imperative to develop efficient and lightweight cooling technologies to maintain the chip temperature within optimal working range to ensure the device reliability and prolonged life. Air-cooled heat sinks are popular as they are reliable, cost-effective, easy to install and require less maintenance. Extended surfaces in the forms of plates and pin fins are commonly used to provide increased surface area for heat dissipation via. forced and free convection [2,3,4]. Hwang [5] reported an increment of 30-50% in heat transfer coefficient by mounting turbulators on printed circuit boards (PCB) as compared to configurations without turbulators with air as the working fluid. Air-based jet impingement is a popular cooling concept as it yields high local heat transfer coefficient and has proven to be effective in managing the hotspots on electronic chips. Saini et al. [6] investigated the heat rejection limits of air-cooled plate fin heat sinks and analyzed the effect of increasing fan speed and base size on the cooling limits for in-duct and impinging flow. With 25% and 33% increment in fan speed and total area, respectively, the air-cooling limits for jet-impingement plane fin heat sink was reported to outperform the duct flow. Garimella et al. [7, 8, 9] investigated the heat transfer characteristics of air-jet impingement for different nozzle diameters, varying nozzle-to-target spacing and for different Reynolds number. The heat transfer on the extended surfaces can be further enhanced by installing ribs, fins, microscale cubic, concentric, and cylindrical roughness features [10-12].

Liquid-based cooling is also popular because of its ability to dissipate significantly higher heat fluxes which are typical of microelectronics, fuel cells and solar power cells, as compared to air. Water is commonly used as coolant in heat sinks because of its high thermal conductivity and heat capacity which results in high convective transport. Single- and two-phase flows in microchannels and in porous media and liquid jet impingement cooling are the state-of-art cooling technologies for chips generating high heat loads. Tuckerman and Pease [13] carried out a pioneering work in the development of water-cooled microchannels, where they demonstrated heat dissipation of ~ 790 $\mathrm{W/cm^2}$ with rise of 71ºC of substrate temperature above the input water temperature. Extensive research has been conducted on microchannels since then, e.g. [14, 15]. Effect of fin-spacing was investigated in water cooled mini-channel heat sinks by Jajja et al. [16] where fin spacing of 0.2 mm yielded the maximum heat transfer coefficient of 2,156 $\mathrm{W/m^2K}$ at a volumetric flow rate of 1 L/min. Several numerical studies [17-20] have reported the performance of the modified microchannels, such as single- and double-layer wavy microchannels, microchannels with near-inlet bifurcations and microchannels equipped with dimples, grooves, and protrusions. Although high heat dissipation capabilities have been observed for micro- and mini-channels, the significantly large pumping power required to maintain a certain flow rate is still a concern which motivates the development of some alternative cooling schemes.

Open-celled metal foam structures have high effective thermal conductivity, large specific area for fluid interaction and provide enhanced fluid mixing due to flow tortuosity. Boomsma et al. [21] investigated compressed aluminum-alloy foams for heat flux up to 68.8 $\mathrm{W/cm^2}$ with water as coolant. The thermal resistance of compressed foam was 2 to 3 times lower than commercially available heat exchanger at a given pumping power. Zhang et al. [22] investigated the flow and heat transfer characteristics of eight copper foam specimens with pore density of 60 and 100 PPI and four porosities between 0.6 to 0.9. Based on thermal resistance curve against pumping power, the optimal porosity (yielding in lowest thermal resistance) for 60 PPI and 100 PPI, was 0.8 and 0.9, respectively. Recently, extensive research on the flow and heat transfer potential of metal foams subjected to air jet impingement has been conducted by Singh et al. [23-29]. Above literature highlights some common technologies employed in electronic cooling where every technology has its own pros and cons. Liquid-cooled heat sinks clearly outperform the air-cooled ones for high heat flux applications. However, the direct impingement of air jet on chip surface, impingement of air jet on extended surface attached to the heated chip and integration of heat pipes can significantly improve the performance of air-based heat sinks over parallel or cross flow ducts. Microchannels with liquid coolant and metal foams inserts provide high heat transfer coefficient but at the expense of very high pressure drop. Comprehensive reviews on different cooling technologies has been provided in the studies [30-33].

Introduction of inserts into the flow path of microchannels [34,35] enhance heat transfer through turbulence generation and enhanced mixing but are also associated with higher pressure drop penalty. Zhang et al. [22] compared the thermal-hydraulic performance of open-cell copper foams with microchannel heat sinks having similar finned area and found that foam-based heat sinks performed better than microchannels at higher pumping power. While open-cell metal foams are associated with high pressure drops, which may be partially attributed to the random and chaotic arrangement of fibers, they are still a preferred cooling mechanism when the cost associated with pumping power is an important design consideration. Further, these foams are fabricated from foaming gas-based method, which essentially results in unit cells of a certain shape based on minimum free surface energy principle (commonly represented with tetrakaidecahedron structure). This method limits the ability to fabricate different unit cell configurations, porosity, and pore density, and hence impose design considerations in efficient heat exchanger development.

More recently, the advancements in the additive manufacturing sector has opened pathways to fabricate repeatable and organized strut-based lattice structures as opposed to random commercial foam structures (which already have high heat dissipation capabilities). The flow and thermal transport of tetrakaidecahedron unit cells has been explored in detail, however, novel cellular structures which fall under different classes, have not been explored for their thermal transport behavior to that extent. Two common classes of cellular structures that are widely investigated because of their structural integrity are the 'Cubic' and 'Octahedron' family [36]. The Cube, Face-diagonal cube (FD-Cube) and Body-centered cube (BC-Cube) topologies comprise the 'Cubic' family, whereas Octa, Octet and V-Octet are some of the common topologies belonging to the 'Octahedron' family. The truncation of edges of Octa topology from 'Octahedron' family yield truncated Octahedron, also known as tetrakaidecahedron, the unit cell representative of commercial metal foams made through foaming process. Klumpp et al. [37] proposed correlations for pressure drop post an extensive study of pressure drop characteristics across the Cubic lattice structures. Recently, two studies have been reported on effective thermal conductivity and interstitial heat transfer coefficient measurements and computations on metal foam based on Octet-shaped unit cells for different porosities with air as the working fluid [38,39].

This study focusses on the numerical investigation of flow and thermal transport in circular-fiber based Octet lattice structure. Here we numerically investigate developing flow and heat transfer characteristics of a single-cell thick Octet lattice (porosity~0.97) where four-unit cells were organized in the streamwise direction. The substrate on which the unit cells were arranged was subjected to a heat flux of 10 W/cm^2 with water as working fluid at mean flow velocities varying between 2-8 cm/s. The effect of thermal boundary condition on heat transfer is studied, where firstly, conjugate heat transfer simulations were conducted which is representative of samples which can be additively manufactured with zero thermal contact resistance between porous structure and the substrate (e.g. as in [40]). The conjugate heat transfer study brings out the net convective heat transport through a control volume. Second, to determine the interstitial heat transfer coefficient around the fibers and at the substrate interface with fluid domain (endwall), a constant heat flux and constant temperature boundary condition was imposed. Detailed flow physics has been discussed to explain the mechanism of flow and thermal transport of this configuration. Following sections present details of the geometrical configuration, computational domain, numerical set up, prediction validation and results.

4.2 Description of test configuration and computational domain

Figure 4.1 shows the representative heat sink channel featuring one-cell thick Octet lattice structure. The unit cell length (s) and circular fiber diameter (d_f) was 10 mm and 0.48 mm, respectively, resulting in porosity of ~97%. The thickness (t) of the bottom and side wall was 1.5 mm. We have undertaken a problem statement involving cooling small areas subjected to high heat flux levels, which allowed placement of four unit cells in the streamwise direction (x). The dimensions of the heat sink channel used in the current study were similar to the plate fin and plate pin fin channels investigated in [2, 3]. Bower et al. [41] studied heat transfer in seven water cooled milli-channels extruded in a solid silicon carbide block. The dimensions of one of the configurations were 33 x 22 x 10.8 mm (L x W x H). Configuration with one cell thick tetrahedral lattice frame was studied by Kim et al. [42, 43] with air as the working fluid.

The derivation of the computational domain simulated in this study is shown in Fig. 4.1a. The symmetric nature of the configuration allowed modeling only one half of a single-cell in the spanwise direction. The inlet and exit lengths were extended by 10 mm and 20 mm, respectively, to achieve hydrodynamically developed flow at entrance and to avoid convergence issues due to back pressure effects. The total length and width of the computational domain was 70 mm and 5 mm, respectively.

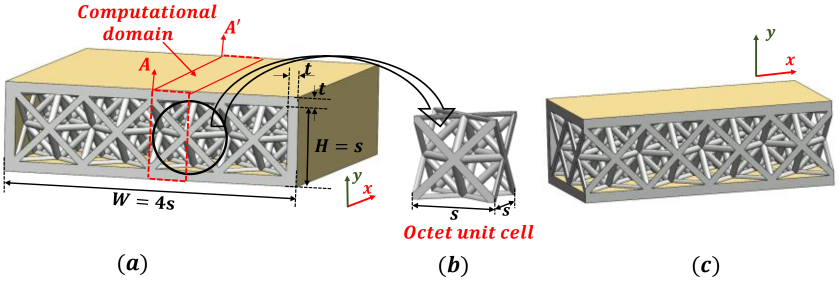

Figure 4.1 (a) Representative heat sink configuration, (b) repeating Octet unit cell, (c) cut-section view of the heat sink channel at plane AA′

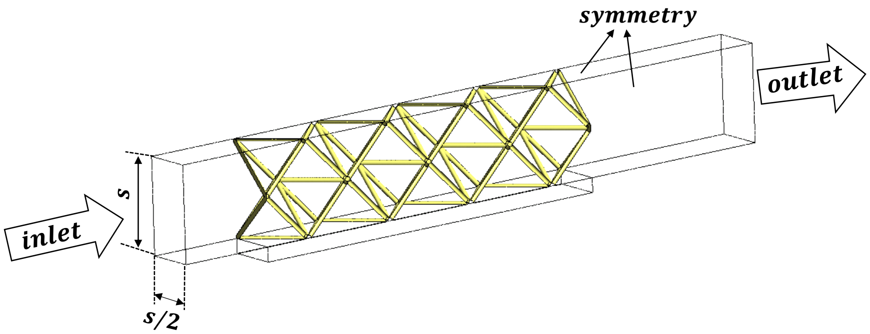

Figure 4.2 Computational domain

4.3 Numerical set-up

This section describes the governing equations for flow and thermal transport in fluid domain and thermal transport in the solid domain, numerical set-up, mesh details, boundary conditions, heat transfer coefficient and pressure drop calculation methodology.

4.3.1 Governing equations

Single unit cell thick tetrahedral configuration of porosity ~0.93 was investigated by Kim et al. [43, 44], where flow was considered to be laminar for Reynolds number ($\mathrm{Re_H}$, based on channel height) smaller than 1,632. Son et al. [45] investigated similar sandwich configuration for ~0.98 porosity tetrahedral unit cell configuration and reported the flow regime to be laminar below Reynolds number ($\mathrm{Re_H}$) of 710. The $\mathrm{Re_H}$ corresponding to the maximum velocity of ~8 cm/s in the present study was 796 and porosity was ~0.97. Based on the range of transition Reynolds number reported for single-unit cell thick configurations, laminar flow assumption was considered for simulations. Following three-dimensional, steady-state, incompressible laminar equations were solved for mass, momentum, and energy:

Continuity:

$$\frac{\partial u_i}{\partial x_i} = 0 \tag{4.1}$$

Momentum:

$$\frac{\partial(\rho_f u_j u_i)}{\partial x_j} = -\frac{\partial p}{\partial x_i} + \frac{\partial}{\partial x_j}\left(\mu_f \frac{\partial u_i}{\partial x_j}\right) \tag{4.2}$$

Energy transport equation in fluid domain:

$$\frac{\partial(\rho_f c_{p_f} u_j T_f)}{\partial x_j} = \frac{\partial}{\partial x_j}\left(k_f \frac{\partial T_f}{\partial x_j}\right) \tag{4.3}$$

Energy transport equation in solid domain:

$$\frac{\partial}{\partial x_j}\left(\frac{\partial T_S}{\partial x_j}\right) \quad = 0 \tag{4.4}$$

where u, c_{p_f}, and μ_f are velocity, specific heat capacity and dynamic viscosity of the fluid, respectively. The fluid properties were assumed constant in the simulations.

4.3.2 Numerical schemes, boundary conditions and conjugate heat transfer considerations

The simulations were carried out using finite-volume based solver ANSYS FLUENT ver. 2019 R2 (academic license). The convective terms in momentum and energy equations were discretized by second order upwind method and diffusion terms were discretized by central-difference method. SIMPLE scheme was used for coupling pressure and velocity. The minimum residual values for convergence were set at 10^{-6} for momentum, x-, y-, and z-velocities and 10^{-8} for energy. The average temperature at the bottom solid-fluid interface wall was also monitored to ensure the convergence of the solution.

Uniform inlet velocity and fluid temperature (300K) was specified at the entrance of the fluid domain, and simulations were conducted for velocities ranging from 2 cm/s to 8 cm/s. Symmetry boundary condition was provided on the two side-walls of the computational domain (Fig. 4.2). Constant heat flux ($\mathrm{q}'' = 10\,\mathrm{W/cm^2}$) was provided at the bottom wall of the substrate in conjugate heat transfer simulations. A pressure outlet-type (zero-gauge pressure) boundary condition was set at the exit. The upper wall and the bottom wall of the inlet and outlet extensions were adiabatic. No-slip boundary condition was imposed on the walls. Coupled boundary condition with heat flux and temperature continuity was imposed on the solid-fluid interface. Figure 4.3 shows the schematic of the solid-fluid interface wall along with adjacent fluid- and solid-phase cells on the either side. The temperature and heat flux continuity across the interface are given as,

$$T_{s,i} = T_{f,i} = T_i \tag{4.5}$$

and

$$k_s \frac{(T_s - T_i)}{\Delta n_s} = k_f \frac{(T_i - T_f)}{\Delta n_f} \tag{4.6}$$

where $T_{s,i}$ and $T_{f,i}$ represents the fluid- and solid-side temperatures at the interface wall. By the assumption of temperature continuity, these temperatures were equal and denoted by T_i, the common interface-wall temperature. T_f and T_s were the fluid- and solid-phase cell temperatures adjacent to the interface wall. Δn_f and Δn_s were the distances of the fluid- and solid-phase cell centers from the interface wall surface.

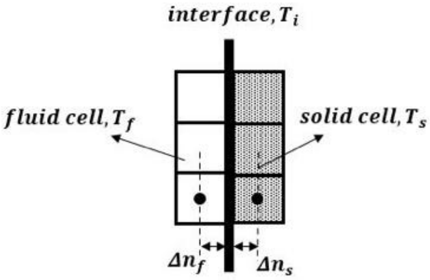

Figure 4.3 Schematic of fluid-solid interface temperature calculation

The conjugate nature of simulations necessitates the evaluation of solid-to-fluid thermal conductivity ratio (k_s/k_f) on local thermal equilibrium (LTE) at the solid-fluid interface. The comparison of LTE and local thermal non-equilibrium (LTNE) results by Xu et al. [46] and Yang et al. [47] revealed that significant differences may be incurred between solid and fluid temperatures for high (k_s/k_f) values such as that encountered in aluminum-air pair where $k_s/k_f \sim$

O (10^4). Phanikumar and Mahajan [48] numerically studied the LTNE effects in air-aluminum and water-aluminum foam samples by comparing the solid and fluid phase temperature and found that the difference between solid and fluid temperature for water-aluminum pair was 7.4% and 16% in aluminum-air case, concluding that LTE would be justified for water-aluminum case (lower k_s/k_f ratio).

In the present study, two different solids have been simulated, viz. 420 Stainless Steel (infiltrated with bronze, 40%) and aluminum alloy (AlSi10Mg). The thermophysical properties of these two solids are summarized in Table 4.1, along with that of the working fluid. The k_s/k_f value for the stainless steel-based solid and the aluminum alloy was ~ 37 and ~ 288, respectively. The reason behind the choice of these two solid mediums is because of their application in additive manufacturing of porous structures based on the configuration present here. The resultant values of (k_s/k_f) is sufficiently low and LTNE was not invoked considering the recommendations of Hunt and Tien [49], who carried out an experimental and numerical investigation on foams made from aluminum, carbon and nickel with water as working fluid with LTE assumption for solid and fluid heat exchange.

Table 4.1 Thermophysical properties of materials used in simulations

Property	**AlSi10Mg**	**420**	**Water**
Density, ρ (kg/m^3)	2,670	7,860	998
Specific heat capacity, c_p (J/kgK)	890	478	4,182
Thermal conductivity, k (W/mK)	173	22	0.6
Dynamic viscosity, μ (kg/ms)	--	--	0.001003

4.3.3 Mesh generation and grid independence

The solid and fluid domains were discretized using tetrahedral elements with conformal meshing at their interface (Fig. 4.4). A typical view of the mesh is shown in Fig. 4.4a which captures a part of the entrance region, fibers, fluid domain, and the substrate. Figure 4.4b shows a zoomed-in view of the mesh for fibers (diameter = 0.48 mm) with dense mesh to accurately model the heat diffusion according to the governing $Eq. (4.4)$ in the solid-phase and to resolve the heat flux at the solid-fluid interface. The mesh in the fluid domain at the solid-fluid interface was also refined to capture the steep gradients in the fluid-phase (essentially resolving fluid-phase heat flux).

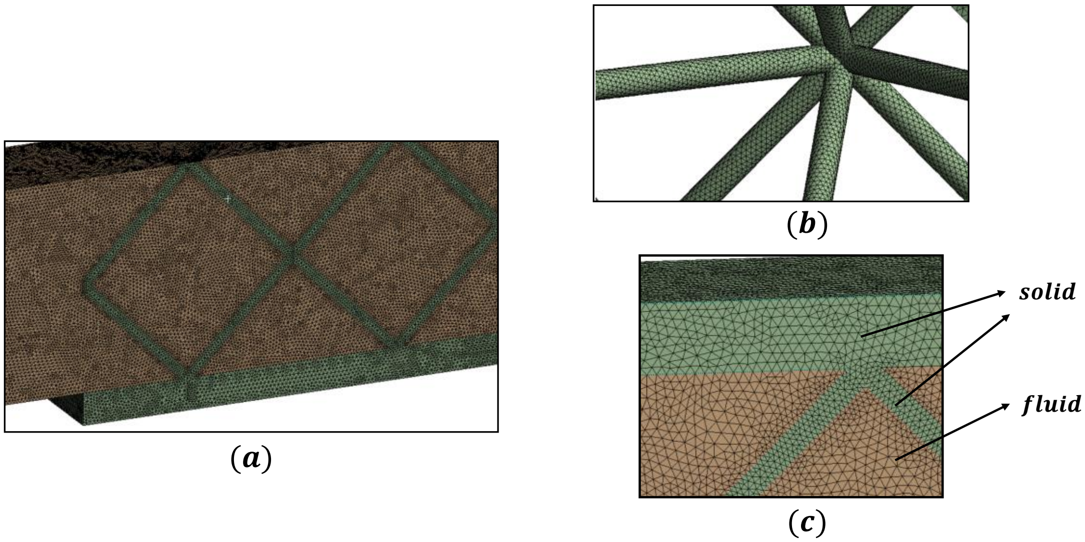

Figure 4.4 (a) Tetrahedral elements in the solid and fluid domain, (b) refinement on the surface of the fibers, (c) conformal meshing at solid-fluid interface

The grid independence study was carried out at the highest velocity of 8 cm/s for $k_s/k_f \sim 288$. Nearly 5.6 million elements were present in the base mesh which was then refined to a finer mesh scheme with a total of ~10.6 million elements. The difference in the average endwall (solid-fluid interface) temperature and inlet pressure was within 0.1% when baseline mesh was compared with the fine mesh, and hence the baseline mesh (already significantly refined) was chosen for further computations to strike a balance between computational accuracy and cost.

4.4 Heat transfer coefficient and pressure drop calculations

Figure 4.5 represents the computational domain mirrored about symmetry plane. Important nomenclature associated with the configuration is also indicated, along with the thermal boundary conditions in different segments of the computational domain. The global heat transfer coefficient is defined as,

$$h_c = \frac{q''_{heated\ wall}}{\left(\bar{T}_{w,L} - \frac{1}{L}\int_0^{L=4s} T_b(x)dx\right)} = \frac{\dot{m}c_p(T_{b,i_{max}} - T_{b,i_{min}-1})}{A_{b,L}\left(\bar{T}_{w,L} - \frac{1}{L}\int_0^{L=4s} T_b(x)dx\right)} \tag{4.7}$$

where $'i'$ denotes the index number of unit cells. $T_{b,i_{min}-1}$ and $T_{b,i_{max}}$ were the bulk fluid temperatures at the planes marking the beginning and end of the Octet unit cells, respectively. The area $'A_{b,L}'$ and average wall temperature $'\bar{T}_{w,L}'$ were calculated on the surface of the solid substrate underlying the solid-fluid interface. $'T_b(x)'$ denotes the bulk temperature variation interpolated in the streamwise direction. The cell-based heat transfer coefficient is defined as,

$$h_{c,i} = \frac{\dot{m}c_p(T_{b,i} - T_{b,i-1})}{A_{b,i}\left(\bar{T}_{w,i} - \frac{1}{s}\int_{(i-1)s}^{is} T_b(x)dx\right)} \tag{4.8}$$

where $\dot{m}c_p(T_{b,i} - T_{b,i-1})$ is the net heat dissipated in i^{th} cell. The definition of rest of the parameters was similar to that described for global heat transfer coefficient h_c.

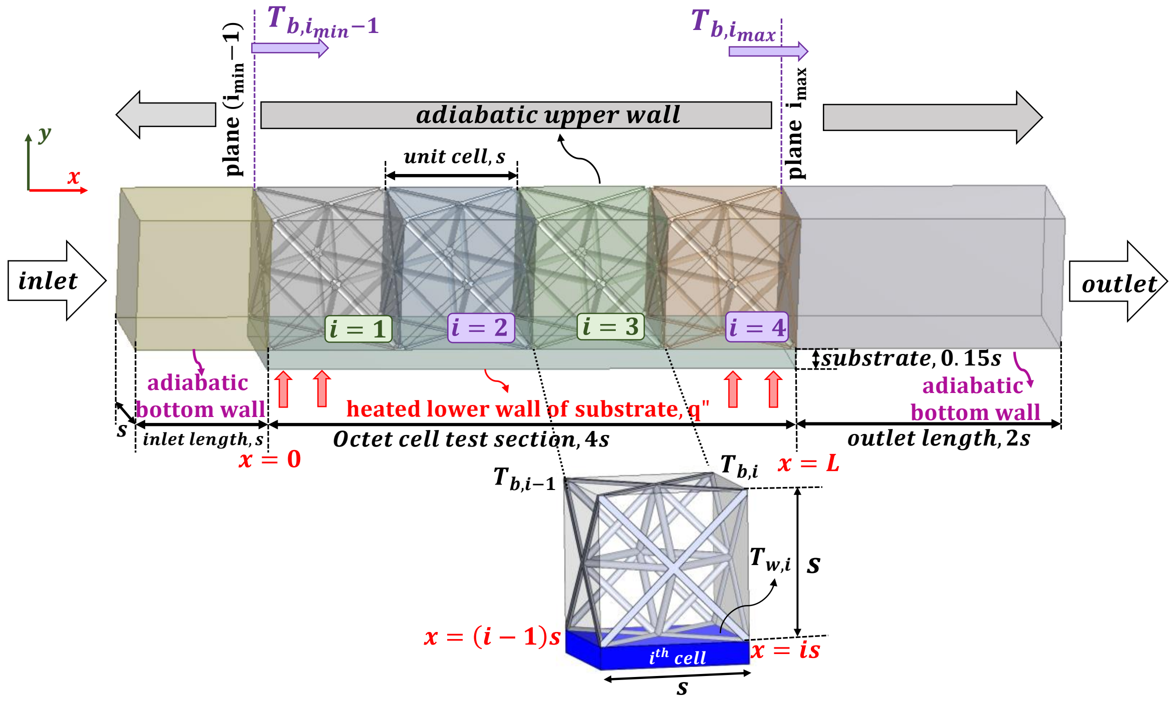

Figure 4.5 Schematic of one cell spanwise width showing boundary conditions and notations used in the heat transfer and pressure drop calculations

Apart from wall heat transfer coefficient, calculation of interfacial heat transfer coefficient of metal foams is of interest to researchers. Wall heat transfer coefficients are more useful from the perspective of practical applications as the heat flux and temperature on the base plate are generally the parameters which can be predicted from wall heat transfer coefficient values. However, the information of interfacial heat transfer coefficients in conjunction with the interfacial area density can provide an insight into the heat dissipation potential around the solid-fluid interface in the fiber region. With the knowledge of endwall heat transfer coefficient and the interfacial heat transfer coefficient at the fibers, one can investigate the convective transport capability of the entire heat sink. Furthermore, interfacial heat transfer coefficients are input a priori in volume-averaged simulations. To this end, interfacial heat transfer coefficient was calculated by imposing constant heat flux and constant temperature on the walls. Local interfacial heat transfer coefficient was defined as,

$$h_{sf}(x,y,z) = \frac{q"(x,y,z)_{octet\ wall}}{[T_{octet\ wall}(x,y,z) - T_b(x)]} \tag{4.9}$$

Average interfacial heat transfer coefficient was then obtained by,

$$\bar{h}_{sf} = \frac{1}{A_{sf}} \iint h_{sf} dA \tag{4.10}$$

where, $'A_{sf}'$ is the total interfacial area. Similarly, local, and average interfacial heat transfer coefficient on the endwall for the constant heat flux/temperature boundary conditions were calculated using $Eq. (4.11)$ and (4.12), respectively.

$$h_w(x,y,z) = \frac{q"(x,y,z)_{endwall}}{[T_{endwall}(x,y,z) - T_b(x)]} \tag{4.11}$$

$$\bar{h}_w = \frac{1}{A_w} \iint h_w dA \tag{4.12}$$

4.5 Results and discussion

This section presents the numerical validation study, flow-field and local heat transfer coefficients, averaged heat transfer performance and pressure drop characteristics of the Octet lattice structure. The section concludes with a relative comparison of thermal performance with other similar study.

4.5.1 Numerical validation

Sundén [50] performed conjugate numerical heat transfer simulations on a cylinder in crossflow with heated core and for different k_s/k_f ratios. Similar validation was performed by Kopanidis et al. [51] on a hollow cylinder having heated internal core and subjected to fluid velocity corresponding to Reynolds number (based on outer cylinder diameter) of 20. The test configuration for validation (Fig. 4.6a and b) in the present study was taken to be a hollow cylinder with inner to outer diameter (D_c/D_o) ratio of 0.5. The corresponding mesh is shown in Fig. 4.6c. Constant temperature (T_c) boundary condition was imposed on the inner core of the solid cylinder.

Figure 4.7(a, b) shows the comparison of Nusselt number variation as a function of angular position along the curved surface for k_s/k_f = 20 and k_s/k_f = 4, respectively, at Reynolds number of 40. Figure 4.7(c, d) shows the comparison of normalized temperature distribution along the line passing through the center of the cylinder in the streamwise direction. The temperature T_o refers to the freestream fluid temperature. The temperature distribution within the solid and the prediction of Nusselt number variation on the surface were found to be in acceptable agreement with [50], ensuring that the temperature predictions along the solid-fluid interface were fairly accurate.

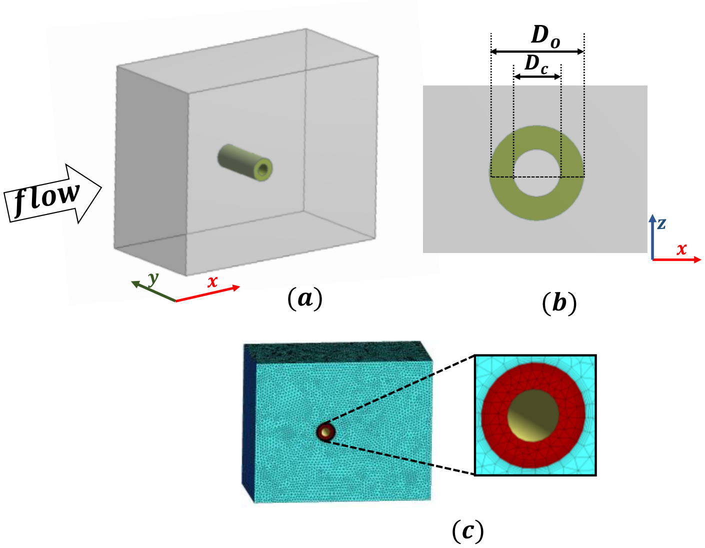

(a) (b)

(c)

Figure 4.6 (a) Configurational set-up of hollow cylinder in cross flow, (b) cross-sectional area of cylinder showing inner and outer diameter, (c) mesh generated in the solid and fluid domain

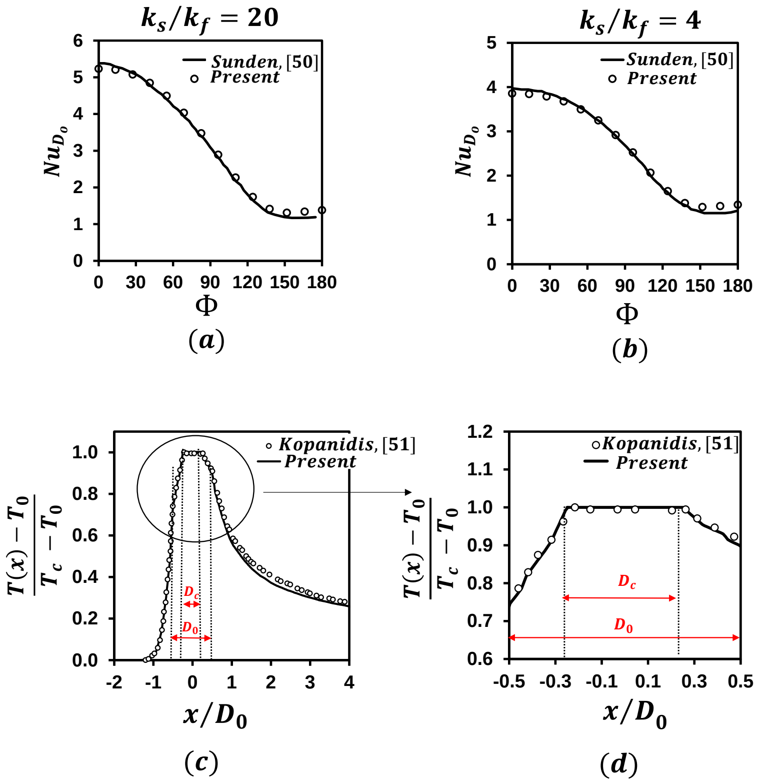

(*a*) (*b*)

(*c*) (*d*)

Figure 4.7 (a) Nusselt number based on outer cylinder diameter as a function of angular displacement along the curved surface for k_s/k_f=20 at Reynolds number of 40, (b) Nusselt number based on outer cylinder diameter as a function of angular displacement along the curved surface for k_s/k_f=4 at Reynolds number of 40, (c) Normalized temperature variation along the line drawn through the cylinder center in the streamwise direction for k_s/k_f=4 at Reynolds number of 20, (d) Normalized temperature variation within the solid thickness for k_s/k_f=4 at Reynolds number of 20

4.5.2 Flow-field predictions

Figure 4.8a shows the velocity contours on the symmetry plane (Fig. 4.2) for inlet velocity of 8 cm/s. Low velocity recirculation zones were observed in the wake region of fiber junctions. Similar recirculation zones were apparent on plane P1 parallel to the endwall passing through the mid of the third unit cell as shown in Fig. 4.8b. The streamlines then follow a symmetric distribution about the center line. Secondary flows perpendicular to the flow direction are presented on plane P2 parallel to the inlet and passing through the middle of the third unit cell in the streamwise direction. The incoming flow stagnates on the fiber walls and then accelerates laterally away from either side of the fibers. Amongst all the planes shown in Fig. 4.8, highest velocity magnitudes were observed on secondary flow plane P2. Unlike stochastic metal foams, the flow patterns in the additively manufactured Octet lattice is more ordered and symmetric about the mid planes due to well-defined fluid-domains.

4.5.3 Heat transfer characteristics

Figure 4.9 shows the temperature variation within the solid phase and on the bottom plane at the solid-fluid interface for the two thermal conductivity ratios at flow inlet velocity of 8 cm/s when the back side of the substrate was subjected to a heat flux of $10\ W/cm^2$. The conjugate heat transfer effects can be clearly observed through the local temperature values on the fiber wall and the endwall. The interesting finding of this study is that only the bottom half of the unit cell primarily participated in heat diffusion through the solid phase for both the k_s/k_f values, with more heat penetration along the foam height for $k_s/k_f = 288$, which is expected. This finding further supports the design of single-celled thick heat sinks since it provides enhanced utilization of metal foam volume in heat dissipation, unlike using thicker metal foams. At the endwall, the temperature gradient was higher for $k_s/k_f = 37$ as the lateral heat conduction for $k_s/k_f = 288$ was stronger, making this configuration more suitable for cooling electronic equipment due to the substrate temperature uniformity it offers.

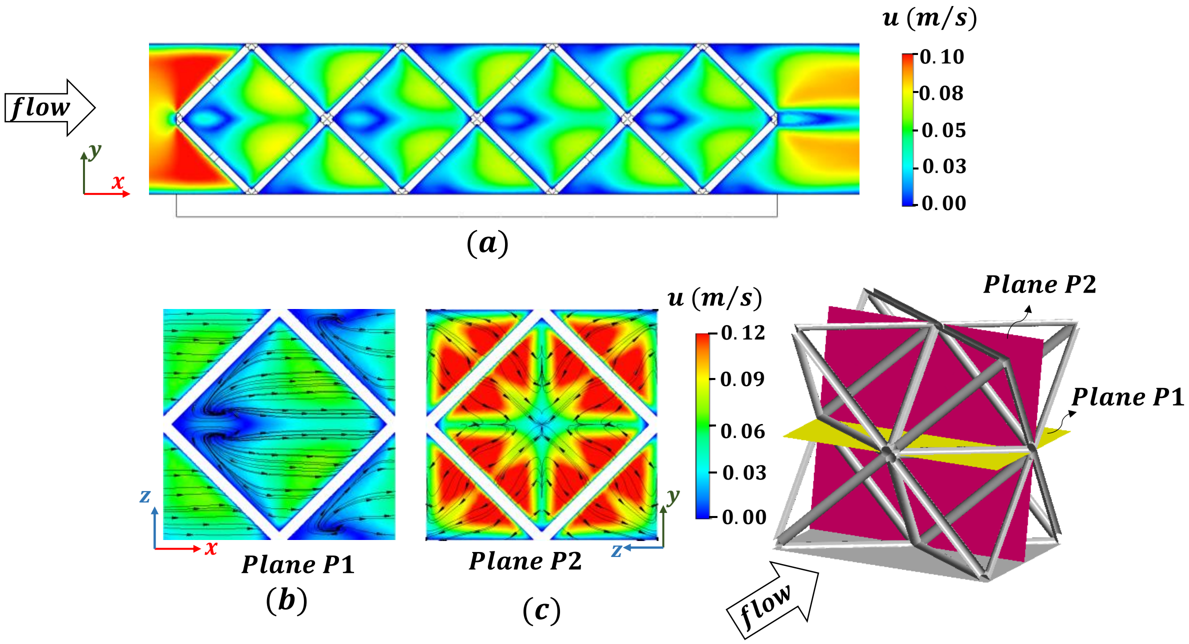

Figure 4.8 Velocity contour on symmetry plane at flow inlet velocity of 8 cm/s, (b) velocity contour on a plane passing through the mid of the third unit cell parallel to the endwall at flow inlet velocity of 8 cm/s (c) velocity contour on plane passing through the mid of the third unit cell perpendicular to the flow direction at flow inlet velocity of 8 cm/s

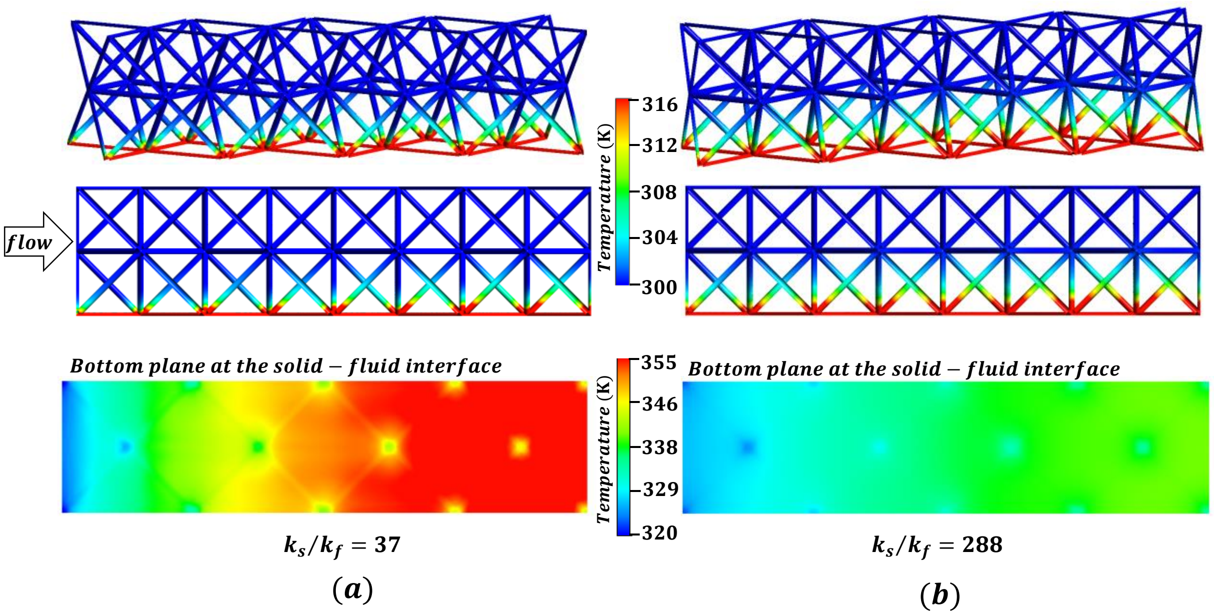

Figure 4.9 (a) Temperature contours in solid phase and on bottom plane at the solid-fluid interface for k_s/k_f=37 at flow inlet velocity of 8 cm/s, (b) Temperature contours in solid phase and on bottom plane at the solid-fluid interface for k_s/k_f=288 at flow inlet velocity of 8 cm/s

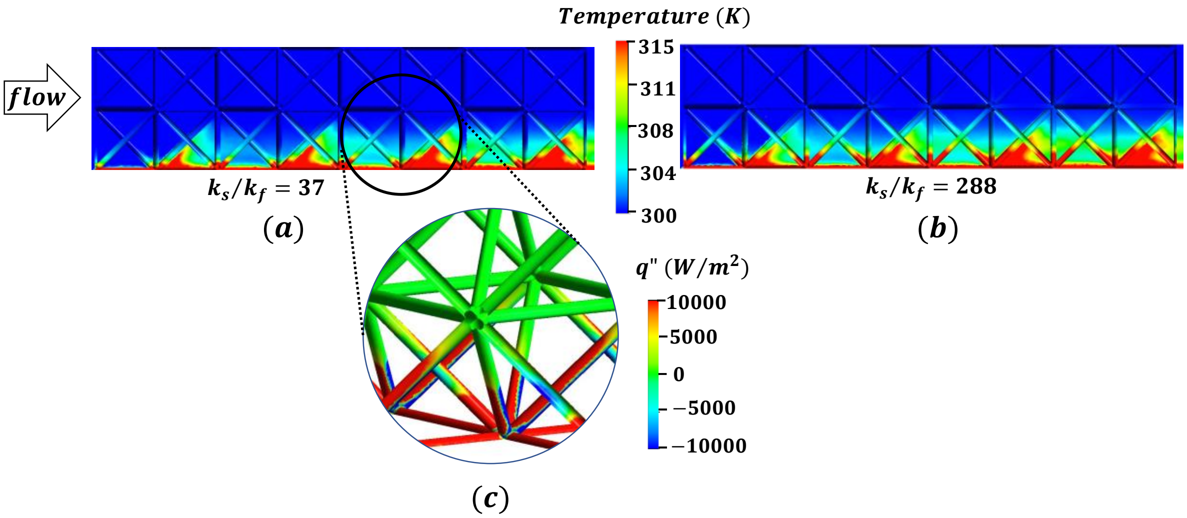

Figure 4.10 (a) Temperature contours in solid and fluid phase for k_s/k_f=37 at flow inlet velocity of the 8 cm/s, (b) Temperature contours in solid and fluid phase for k_s/k_f=288 at flow inlet velocity of the 8 cm/s, (c) Heat flux contours on Octet walls of third unit cell

4.5.3.1 A note on heat transfer reversal

Figure 4.10 shows the temperature profile in both solid and fluid phases at flow velocity of 8 cm/s (conjugate simulation). The increase in fluid phase temperature can be observed with increasing streamwise distance from the inlet, suggesting that long heat sink designs will result in low convective heat transfer capabilities towards the later few unit cells. Negative heat flux (heat transfer from fluid to solid phase) was observed for both k_s/k_f ratios. There is no detailed description of occurrence of reverse heat transfer in the literature pertaining to pore-scale conjugate metal foam simulations. The phenomenon of “heat transfer reversal” (HTR) was reported by Fiebig et al. [52] in the conjugate heat transfer analysis of finned tube. The reverse heat transfer occurred in the recirculation zones downstream of the tube. Figure 4.10 shows the presence of substantial reverse heat transfer zones in the wake regions of the circular fibers (similar to tubes). The slowly recirculating fluid in the vicinity of the solid was heated up to a temperature higher than the adjacent solid layer under steady-state condition, resulting in locally negative heat flux. Zoomed-in view of negative heat flux sites is shown in Fig. 4.10c. Relatively lower magnitudes of negative heat flux were present in small areas on the upstream faces of the fiber tubes that were directly facing the fluid.

The fluid near the endwall received heat from the adjacent Octet wall as well as the heated endwall surface. The fluid temperature in the upper Octet half was not directly influenced by the heat from the endwall. The local fluid temperature in the upper half of the unit cell depends on the heat that is being transported convectively by bulk flow in streamwise direction, by heat diffused (in positive y-direction) by the heated fluid in the lower half of the unit cell (in vicinity of heated fibers and the endwall) and the heat conducted from the adjacent fibers.

A resemblance between the low velocity regions near the endwall highlighted in Fig. 4.8a and the high fluid temperature regions (Fig. 4.10a, b) can be observed. The only difference is that the velocity profile is almost constant for successive unit cells, but the temperature profile showed growth due to heat accumulation. The reverse heat transfer was enhanced as the fluid velocity increased from 2 cm/s to 8 cm/s. Kopanidis et al. [51] performed conjugate pore scale simulations in metal foams using air and aluminum as fluid and solid phase in the turbulent regime. Broughton and Joshi [40] studied conjugate heat transfer in rhombic dodecahedron geometry with water and AlSi10Mg as fluid and solid phase in the laminar regime, but no heat transfer reversal phenomenon was reported in these studies. A possible reason may be that the thermal conductivity of water is roughly 25 times higher than that of the air, however the present study's authors reserve their comments on whether or not the heat transfer reversal can be observed with Al-air combination, since the local heat flux contours were not provided in [40,51]. This phenomenon is interesting and should be explored in more detail for wide range of k_s/k_f values.

4.5.3.2 Heat dissipation sites' contribution to overall convective heat transport

Figure 4.11 shows the ratio of heat transferred ($Q_{()}/Q_{total}$) from the fiber and endwall in reference to the total heat dissipated. The endwall being considered here refers to the bottom fluid-solid interface. For k_s/k_f=37, net heat dissipated from the fibers was lower than that carried away from the endwall. For higher thermal conductivity ratio case, k_s/k_f=288, the trend was reversed as more heat was dissipated from the fibers.

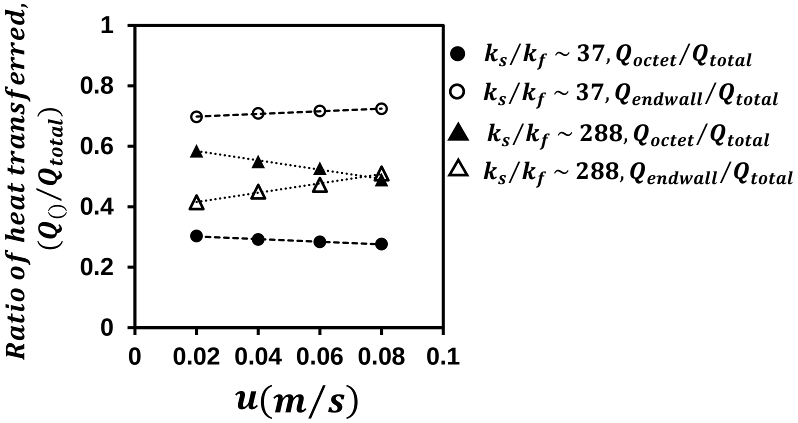

Figure 4.11 Ratio of heat transferred from the Octet wall and endwall to the total heat dissipated

The difference in the ratios of heat convected from the fibers and the endwall decreased with increasing flow velocity, with almost same heat dissipation levels at 8 cm/s. The trend is suggestive of higher heat dissipation from the endwall compared to the fiber walls for higher velocities, and hence, researchers can also investigate modifying the endwall by micro-scale roughness elements to further increase its role in overall heat dissipation. This would essentially reduce the requirement of one full cell thickness of the cellular structure and make the heat sink design even more compact.

Kim et el. [43] investigated the effect of thermal conductivity ratio (k_s/k_f) on endwall heat transfer coefficient in single-cell thick tetrahedral lattice structure having porosity of 94%. The Nusselt number ratio was increased 2.5 times by replacing polycarbonate material core with aluminum alloy. Consistent with the conclusions of the authors [43], Fig. 4.10 shows that solid conductivity is very significant even at very high porosities when solid ligaments are very thin.

4.5.3.3 Unit-cell length-based heat transfer coefficient and globally averaged heat transfer coefficient from conjugate simulations

The cell-based heat transfer coefficient ($h_{c,i}$) decreased with increasing cell number in the streamwise direction (Fig. 4.12a). The monotonic decrease in the heat transfer coefficient for downstream cells for the entire velocity range indicates that the heat transfer was not periodic for this streamwise length, which is a good outcome from the design since the aim was to cool a relatively small area where developing flow behavior can be retained for higher heat transfer coefficient.

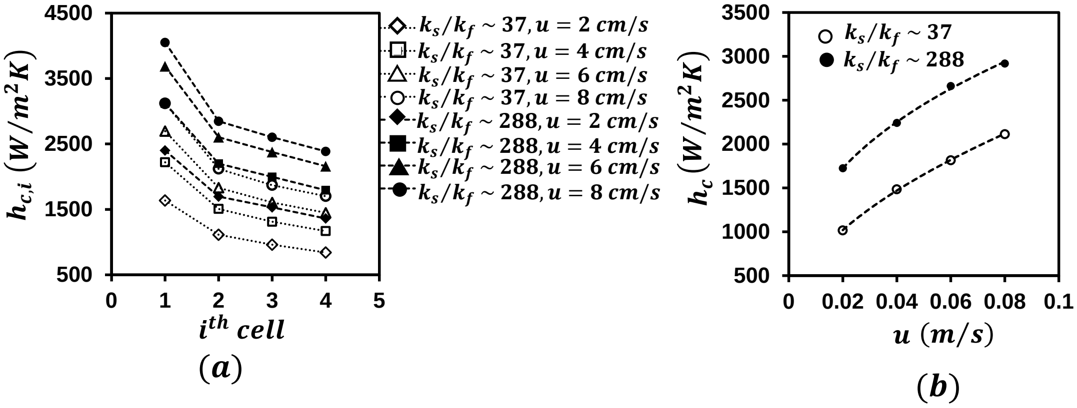

Figure 4.12 (a) Cell based heat transfer coefficient for k_s/k_f equal to 37 and 288, (b) Global heat transfer coefficients for k_s/k_f equal to 37 and 288 as function of flow inlet velocity

Figure 4.12b shows the trend of global heat transfer coefficient (h_c) calculated using $Eq. 4.7$ against the flow inlet velocity. The heat transfer coefficient increased with the increasing velocity as expected and followed an exponential trend. Heat transfer coefficient for k_s/k_f = 288 was 38% to 70% higher than that for k_s/k_f = 37, clearly showing the effect of solid thermal conductivity even at such a high porosity (97%).

4.5.3.4 Interfacial heat transfer coefficient for $q" = const.$ and $T_w = const.$ type thermal boundary conditions

Figure 4.13(a, b) shows the average interfacial heat transfer coefficient calculated using $Eq. (4.10, 4.12)$ for constant surface heat flux and constant surface temperature boundary conditions. For constant heat flux thermal boundary condition, $q" = 10\, W/cm^2$ was imposed on the fibers as well as the endwall. The average fiber temperature values obtained from the constant heat flux simulations were used as a constant wall temperature boundary condition in the other type of simulations. Interfacial heat transfer coefficient, $\bar{h}_{sf}$, on fibers (Fig. 4.13a), was found to be significantly higher for constant heat flux case over the entire range of velocities investigated. The average endwall heat transfer coefficient, $\bar{h}_w$, (Fig. 4.13b) showed similar trends as the constant heat flux imposition yielded higher values. The conjugate global wall heat transfer coefficient, h_c for k_s/k_f=37 was only slightly higher than global heat transfer coefficient obtained from constant heat flux boundary condition ($Eq.$ (4.12)) whereas, for k_s/k_f=288, it was 43% to 69% higher.

Figure 4.13c shows the contours of local interfacial heat transfer coefficient on the Octet wall surface at flow velocity of 8 cm/s. The local interfacial heat transfer distribution on the Octet walls for both the thermal boundary conditions were nearly identical in terms of distribution however different in magnitudes. Higher values were observed on the upstream faces of the fibers that encountered the direct fluid flow impingement and reduced heat transfer values were observed on the rear end of the fibers due to flow recirculation. On the endwalls, lower heat transfer coefficients could be observed just downstream of the fiber-endwall junction (Fig. 4.13d).

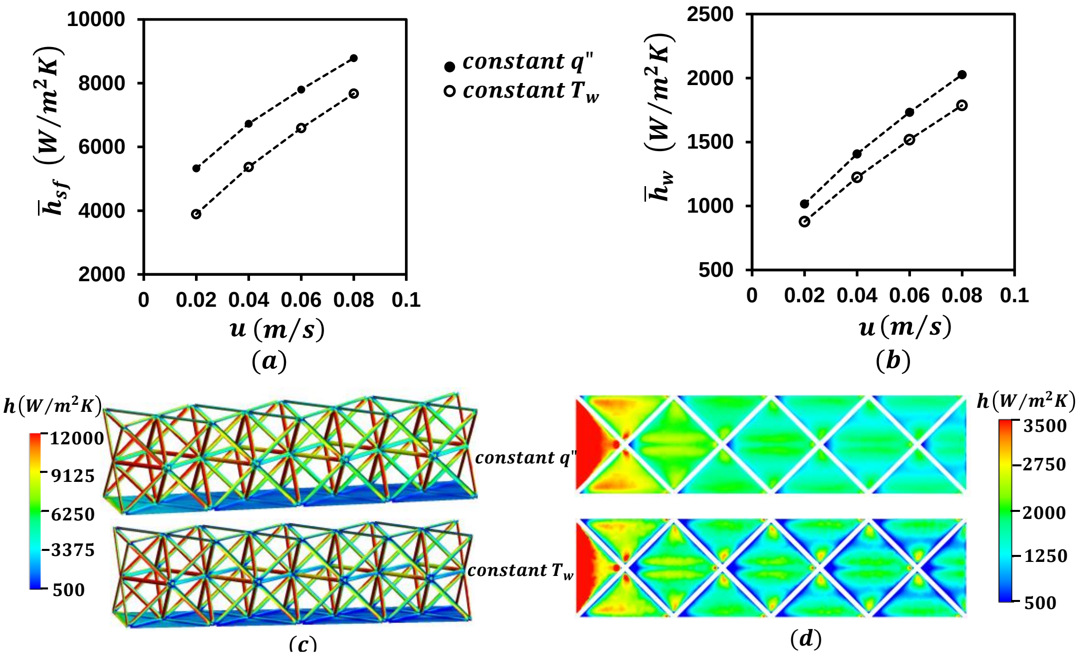

Figure 4.13 (a) Average interfacial heat transfer coefficient on Octet walls corresponding to constant heat flux and constant wall temperature, (b) Average interfacial heat transfer coefficient on endwall corresponding to constant heat flux and constant wall temperature, (c) Contours of local interfacial heat transfer coefficient on the Octet wall surface at flow inlet velocity of 8 cm/s, (d) Contours of local interfacial heat transfer coefficient on the endwall surface at flow inlet velocity of 8 cm/s

4.5.4 Pressure drop characteristics

The pressure drop in metal foams is presented by the following second order Darcy-Forchheimer equation:

$$\frac{\Delta P}{L} = \frac{\mu}{K}u + \frac{\rho C_F}{\sqrt{K}}u^2 \tag{4.13}$$

where, K is the permeability and C_F is the inertial or Forchheimer coefficient. The pressure drop showed quadratic trend with respect to the superficial inlet velocity (Fig. 4.14). The average pressure drop data was measured across the octet cell test section i.e. $L = 4s$ as shown in Fig. 4.5.

Based on the obtained data, permeability (K) and inertial coefficient (C_F) were calculated to be 4.85 x 10^{-7} m^2 and 0.02747, respectively. Maximum pressure drop of ~ 416 Pa/m was encountered corresponding to the maximum flow velocity of 8 cm/s.

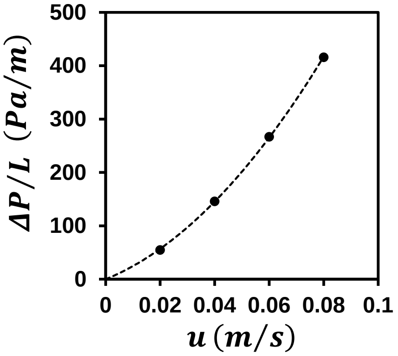

Figure 4.14 Pressure drop per unit length

4.5.5 Comparison of heat transfer performance of present study's Octet configuration with stochastic metal foam and additively manufactured foams

Figure 4.15 compares the globally averaged Nusselt number of the present Octet configuration (based on conjugate simulations) with that of the stochastic and additively manufactured (AM) rhombic dodecahedron unit cell lattice investigated by Broughton and Joshi [40]. The solid material in stochastic ERG sample and AM rhombic dodecahedron lattice was Al6101 ($k_s = 167\,W/mK$) and AlSi10Mg ($k_s = 173\,W/mK$), respectively, and water ($k_f = 0.6\,W/mK$) was used as the working fluid. To allow direct comparison with Broughton and Joshi [40], we have chosen channel height as the characteristic length to define the Nusselt number ($h_c H/k_f$) and Reynolds number ($\rho u H/\mu$). The authors in [40] found that additively manufactured lattice yielded in higher Nusselt number values compared to the stochastic metal foams. The present Octet configuration had higher Nusselt number values than the stochastic metal foam for both the thermal conductivity ratios (k_s/k_f=37 and k_s/k_f=288). The Octet lattice with k_s/k_f=288 had better thermal performance than the rhombic dodecahedron lattice in [40], however, the Octet lattice configuration with k_s/k_f=37 showed similar Nusselt number values at Re_H ~700 and the trend indicated that the Octet lattice could outperform the rhombic dodecahedron at higher Reynolds number. It should be noted that the resulting porosity in [40] was 86.5% which is much lower than the present study (97%), hence the present study's configurations are associated with much lower pressure drop.

The authors in [40] considered rhombic dodecahedron unit cell topology as a representative of the commercial metal foam morphology, with an aim to additively manufacture foams which essentially results in zero thermal contact resistance compared to the assembly of commercial foams on a metal substrate. The high porosity Octet cell-based single cell thick foam configurations of this study outperforms the ones studied in [40] and hence further parametric studies on this Octet configuration is recommended for different porosity values and fiber length-to-diameter ratios. Another interesting comparison between the present study and [40] is the foam volume usage extent, where inferring from the local fiber temperature contours in [40], a large volume of the foam was under-utilized in heat dissipation, whereas present study's single cell thickness yielded in high foam volume usage (>50%, see Fig. 9a). This behavior is suggestive of the efficacy of thinner foams in terms of both, enhanced convective transport and lower pressure drop, a conclusion also presented in Singh et al. [12,23].

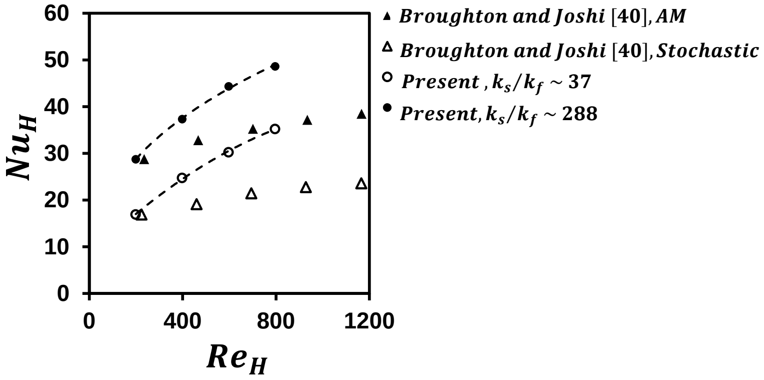

Figure 4.15 Nusselt number comparison

4.6 Conclusions

We have reported our numerical investigation on the conjugate heat transfer characteristics of single cell thick Octet lattice structure (97% porosity), for developing flow with water as working fluid. The substrate on which the Octet structures were assembled was subjected to a heat flux of 10 W/cm^2. The working fluid velocity was varied from 2 cm/s to 8 cm/s. Two different solid-to-fluid thermal conductivity ratios, k_s/k_f=37 and 288 were investigated for conjugate simulations. Further, to calculate interstitial heat transfer coefficient, simulations were performed for constant heat flux and constant temperature thermal boundary conditions. Following conclusions are drawn from this study:

- Global wall heat transfer coefficients for k_s/k_f=288 was 38% to 70% higher than that obtained from k_s/k_f=37.
- Unit cell-based heat transfer coefficient trend depicted monotonically decreasing behavior, which is typical of developing flow.
- The global heat transfer coefficient obtained through control volume-based energy balance method was ~2,900 W/m^2K for $k_s/k_f \sim 288$ and ~2,100 W/m^2K for $k_s/k_f \sim 37$, for flow velocity of 8 cm/s.

- The interfacial heat transfer coefficient obtained on fiber walls and endwall from constant heat flux boundary condition was ~8,700 W/m^2K and ~2,000 W/m^2K, respectively, for flow velocity of 8 cm/s.

NOMENCLATURE

C_F	inertial coefficient
$c_{p,f}$	specific heat capacity of water
H	height of the channel
h_c	wall heat transfer coefficient corresponding to conjugate simulations
$\mathrm{h_{sf}}$	interfacial heat transfer coefficient
$\mathrm{h_w}$	wall heat transfer coefficient corresponding to constant wall heating conditions
$\mathrm{k_f}$	thermal conductivity of water
$\mathrm{k_s}$	thermal conductivity of solid-phase
K	permeability
L	length of the test section
$\mathrm{Nu_H}$	Nusselt number based on channel height
q''	heat flux
$\mathrm{Re_H}$	Reynolds number based on channel height
s	unit cell length
t	substrate thickness
$\mathrm{T_w}$	temperature of the fiber walls
$\mathrm{T_b}$	bulk fluid temperature
u	inlet velocity of the fluid
$\Delta\mathrm{P}$	pressure drop across unit cell
$\Delta\mathrm{n_s}$	distance of the interface from the adjacent solid-phase cell
$\Delta\mathrm{n_f}$	distance of the interface from the adjacent fluid-phase cell
i	index reference to the unit cell number

Greek symbols

ρ_f	density of water
μ_f	dynamic viscosity of water

REFERENCES

[1] Chu, R.C., Simons, R.E., Ellsworth, M.J., Schmidt, R.R. and Cozzolino, V., 2004. Review of cooling technologies for computer products. IEEE Transactions on Device and materials Reliability, 4(4), pp.568-585.

[2] Yuan, W., Zhao, J., Tso, C.P., Wu, T., Liu, W. and Ming, T., 2012. Numerical simulation of the thermal hydraulic performance of a plate pin fin heat sink. Applied Thermal Engineering, 48, pp.81-88.

[3] Yu, X., Feng, J., Feng, Q. and Wang, Q., 2005. Development of a plate-pin fin heat sink and its performance comparisons with a plate fin heat sink. Applied thermal engineering, 25(2-3), pp.173-182.

[4] Kim, S.J., Kim, D.K. and Oh, H.H., 2008. Comparison of fluid flow and thermal characteristics of plate-fin and pin-fin heat sinks subject to a parallel flow. Heat Transfer Engineering, 29(2), pp.169-177.

[5] Hwang, U.P., 1984, March. Thermal design using turbulators for air-cooled electronic modules on a card package. In Proceedings of the National Electronic Packaging and Production Conference (pp. 441-449).

[6] Saini, M. and Webb, R.L., 2002, May. Heat rejection limits of air cooled plane fin heat sinks for computer cooling. In ITherm 2002. Eighth Intersociety Conference on Thermal and Thermomechanical Phenomena in Electronic Systems (Cat. No. 02CH37258) (pp. 1-8). IEEE.

[7] El-Sheikh, H.A. and Gurimella, S.V., 2000. Enhancement of air jet impingement heat transfer using pin-fin heat sinks. IEEE Transactions on Components and Packaging Technologies, 23(2), pp.300-308.

[8] Brignoni, L.A. and Garimella, S.V., 1999. Experimental optimization of confined air jet impingement on a pin fin heat sink. IEEE Transactions on Components and Packaging Technologies, 22(3), pp.399-404.

[9] Garimella, S.V. and Schroeder, V.P., 2001. Local heat transfer distributions in confined multiple air jet impingement. J. Electron. Packag., 123(3), pp.165-172.

[10] Hsieh, S.S., Tsai, H.H. and Chan, S.C., 2004. Local heat transfer in rotating square-rib-roughened and smooth channels with jet impingement. International journal of heat and mass transfer, 47(12-13), pp.2769-2784.

[11] Hansen, L.G. and Webb, B.W., 1993. Air jet impingement heat transfer from modified surfaces. International journal of heat and mass transfer, 36(4), pp.989-997.

[12] Singh, P., Zhang, M., Ahmed, S., Ramakrishnan, K.R. and Ekkad, S., 2019. Effect of micro-roughness shapes on jet impingement heat transfer and fin-effectiveness. International Journal of Heat and Mass Transfer, 132, pp.80-95.

[13] Tuckerman, D.B. and Pease, R.F.W., 1981. High-performance heat sinking for VLSI. IEEE Electron device letters, 2(5), pp.126-129.

[14] Colgan, E.G., Furman, B., Gaynes, M., Graham, W.S., LaBianca, N.C., Magerlein, J.H., Polastre, R.J., Rothwell, M.B., Bezama, R.J., Choudhary, R. and Marston, K.C., 2007. A practical implementation of silicon microchannel coolers for high power chips. IEEE Transactions on Components and Packaging Technologies, 30(2), pp.218-225.

[15] Ramos-Alvarado, B., Li, P., Liu, H. and Hernandez-Guerrero, A., 2011. CFD study of liquid-cooled heat sinks with microchannel flow field configurations for electronics, fuel cells, and concentrated solar cells. Applied Thermal Engineering, 31(14-15), pp.2494-2507.

[16] Jajja, S.A., Ali, W., Ali, H.M. and Ali, A.M., 2014. Water cooled minichannel heat sinks for microprocessor cooling: Effect of fin spacing. Applied Thermal Engineering, 64(1-2), pp.76-82.

[17] Xie, G., Chen, Z., Sunden, B. and Zhang, W., 2013. Numerical predictions of the flow and thermal performance of water-cooled single-layer and double-layer wavy microchannel heat sinks. Numerical Heat Transfer, Part A: Applications, 63(3), pp.201-225.

[18] Xie, Y., Qu, H. and Zhang, D., 2015. Numerical investigation of flow and heat transfer in rectangular channel with teardrop dimple/protrusion. International Journal of Heat and Mass Transfer, 84, pp.486-496.

[19] Zhang, R., Chen, Z., Xie, G. and Sunden, B., 2015. Numerical analysis of constructal water-cooled microchannel heat sinks with multiple bifurcations in the entrance region. Numerical Heat Transfer, Part A: Applications, 67(6), pp.632-650.

[20] Bi, C., Tang, G.H. and Tao, W.Q., 2013. Heat transfer enhancement in mini-channel heat sinks with dimples and cylindrical grooves. Applied Thermal Engineering, 55(1-2), pp.121-132.

[21] Boomsma, K., Poulikakos, D. and Zwick, F., 2003. Metal foams as compact high performance heat exchangers. Mechanics of materials, 35(12), pp.1161-1176.

[22] Zhang, H.Y., Pinjala, D., Joshi, Y.K., Wong, T.N., Toh, K.C. and Iyer, M.K., 2005. Fluid flow and heat transfer in liquid cooled foam heat sinks for electronic packages. IEEE Transactions on Components and Packaging Technologies, 28(2), pp.272-280.

[23] Singh, P., Nithyanandam, K., Zhang, M. and Mahajan, R.L., 2020. The Effect of Metal Foam Thickness on Jet Array Impingement Heat Transfer in High-Porosity Aluminum Foams. Journal of Heat Transfer, 142(5).

[24] Singh, P., Nithyanandam, K. and Mahajan, R.L., 2020. An experimental and numerical investigation of forced convection in high porosity aluminum foams subjected to jet array impingement in channel-flow. International Journal of Heat and Mass Transfer, 149, p.119107.

[25] Madhavan, S., Singh, P. and Ekkad, S., 2019. Jet Impingement Heat Transfer Enhancement by Packing High-Porosity Thin Metal Foams Between Jet Exit Plane and Target Surface. Journal of Thermal Science and Engineering Applications, 11(6).

[26] Madhavan, S., Sambamurthy, V.S., Singh, P. and Ekkad, S., 2019, November. Effect of Pore Density on Jet Impingement onto Thin Metal Foams under Intermediate Crossflow Scheme. In ASME International Mechanical Engineering Congress and Exposition (Vol. 59452, p. V008T09A034). American Society of Mechanical Engineers.

[27] Singh, P., Zhang, M. and Mahajan, R.L., 2019, November. Effect of Metal Foam Thickness and Pore Density on Array Jet Impingement Heat Transfer. In ASME International Mechanical Engineering Congress and Exposition (Vol. 59452, p. V008T09A035). American Society of Mechanical Engineers.

[28] Panse, S.S., Singh, P. and Ekkad, S.V., 2019, May. Air-Based Cooling in High Porosity, Aluminum Foams for Compact Electronics Cooling. In 2019 18th IEEE Intersociety Conference on Thermal and Thermomechanical Phenomena in Electronic Systems (ITherm) (pp. 376-383). IEEE.

[29] Singh, P., Zhang, M., Pandit, J. and Mahajan, R.L., 2018, November. Array Jet Impingement Onto High Porosity Thin Metal Foams at Zero Jet-to-Foam Spacing. In ASME International Mechanical Engineering Congress and Exposition (Vol. 52125, p. V08BT10A020). American Society of Mechanical Engineers.

[30] Agostini, B., Fabbri, M., Park, J.E., Wojtan, L., Thome, J.R. and Michel, B., 2007. State of the art of high heat flux cooling technologies. Heat Transfer Engineering, 28(4), pp.258-281.

[31] Fan, Y. and Luo, L., 2008. Recent applications of advances in microchannel heat exchangers and multi-scale design optimization. Heat Transfer Engineering, 29(5), pp.461-474.

[32] Chu, R.C., Simons, R.E., Ellsworth, M.J., Schmidt, R.R. and Cozzolino, V., 2004. Review of cooling technologies for computer products. IEEE Transactions on Device and materials Reliability, 4(4), pp.568-585.

[33] Chu, R.C., 1999, March. A review of IBM sponsored research and development projects for computer cooling. In Fifteenth Annual IEEE Semiconductor Thermal Measurement and Management Symposium (Cat. No. 99CH36306) (pp. 151-165). IEEE.

[34] Adewumi, O.O., Bello-Ochende, T. and Meyer, J.P., 2013. Constructal design of combined microchannel and micro pin fins for electronic cooling. International Journal of Heat and Mass Transfer, 66, pp.315-323.

[35] Feng, Z., Luo, X., Guo, F., Li, H. and Zhang, J., 2017. Numerical investigation on laminar flow and heat transfer in rectangular microchannel heat sink with wire coil inserts. Applied Thermal Engineering, 116, pp.597-609.

[36] Egan, P.F., Gonella, V.C., Engensperger, M., Ferguson, S.J. and Shea, K., 2017. Computationally designed lattices with tuned properties for tissue engineering using 3D printing. PloS one, 12(8), p.e0182902.

[37] Klumpp, M., Inayat, A., Schwerdtfeger, J., Körner, C., Singer, R.F., Freund, H. and Schwieger, W., 2014. Periodic open cellular structures with ideal cubic cell geometry: Effect of porosity and cell orientation on pressure drop behavior. Chemical Engineering Journal, 242, pp.364-378.

[38] Ekade, P. and Krishnan, S., 2019. Fluid flow and heat transfer characteristics of octet truss lattice geometry. International Journal of Thermal Sciences, 137, pp.253-261.

[39] Chaudhari, A., Ekade, P. and Krishnan, S., 2019. Experimental investigation of heat transfer and fluid flow in octet-truss lattice geometry. International Journal of Thermal Sciences, 143, pp.64-75.

[40] Broughton, J. and Joshi, Y.K., Comparison of single-phase convection in additive manufactured versus traditional metal foams.

[41] Bower, C., Ortega, A., Skandakumaran, P., Vaidyanathan, R. and Phillips, T., 2005. Heat transfer in water-cooled silicon carbide milli-channel heat sinks for high power electronic applications. J. Heat Transfer, 127(1), pp.59-65.

[42] Kim, T., Zhao, C.Y., Lu, T.J. and Hodson, H.P., 2004. Convective heat dissipation with lattice-frame materials. Mechanics of Materials, 36(8), pp.767-780.

[43] Kim, T., Hodson, H.P. and Lu, T.J., 2004. Fluid-flow and endwall heat-transfer characteristics of an ultralight lattice-frame material. International Journal of Heat and Mass Transfer, 47(6-7), pp.1129-1140.

[44] Kim, T., Hodson, H.P. and Lu, T.J., 2005. Contribution of vortex structures and flow separation to local and overall pressure and heat transfer characteristics in an ultralightweight lattice material. International journal of heat and mass transfer, 48(19-20), pp.4243-4264.

[45] Son, K.N., Weibel, J.A., Kumaresan, V. and Garimella, S.V., 2017. Design of multifunctional lattice-frame materials for compact heat exchangers. International Journal of Heat and Mass Transfer, 115, pp.619-629.

[46] Xu, H.J., Qu, Z.G. and Tao, W.Q., 2011. Analytical solution of forced convective heat transfer in tubes partially filled with metallic foam using the two-equation model. International Journal of Heat and Mass Transfer, 54(17-18), pp.3846-3855.

[47] Yang, C., Nakayama, A. and Liu, W., 2012. Heat transfer performance assessment for forced convection in a tube partially filled with a porous medium. International Journal of Thermal Sciences, 54, pp.98-108.

[48] Phanikumar, M.S. and Mahajan, R.L., 2002. Non-Darcy natural convection in high porosity metal foams. International Journal of Heat and Mass Transfer, 45(18), pp.3781-3793.

[49] Hunt, M.L. and Tien, C.L., 1988. Effects of thermal dispersion on forced convection in fibrous media. International Journal of Heat and Mass Transfer, 31(2), pp.301-309.

[50] Sundén, B., 1980. Conjugated heat transfer from circular cylinders in low Reynolds number flow. International Journal of Heat and Mass Transfer, 23(10), pp.1359-1367.

[51] Kopanidis, A., Theodorakakos, A., Gavaises, E. and Bouris, D., 2010. 3D numerical simulation of flow and conjugate heat transfer through a pore scale model of high porosity open cell metal foam. International Journal of Heat and Mass Transfer, 53(11-12), pp.2539-2550.

[52] Fiebig, M., Grosse-Gorgemann, A., Chen, Y. and Mitra, N.K., 1995. Conjugate heat transfer of a finned tube Part A: heat transfer behavior and occurrence of heat transfer reversal. Numerical Heat Transfer, Part A: Applications, 28(2), pp.133-146.

CHAPTER V

THERMAL-HYDRAULIC PERFORMANCE OF ADDITIVELY MANUFACTURED LATTICES FOR GAS TURBINE BLADE TRAILING EDGE COOLING[4]

Abstract

Gas turbine blade trailing edge cooling is challenging because of the stringent geometrical constraints driven by aerodynamics and thermal stresses. The blade topology becomes significantly thin towards the trailing edge which leaves a narrow room for the construction of internal cooling channels and also makes this section susceptible to failure due to thermal stresses. Conventionally, pin-fins are employed in the internal cooling channels of the trailing edge because they provide high levels of heat transfer coefficient values and also structural integrity. Much of the past studies on pin fins have focused on their relative arrangements, heights, crossflow scheme, etc., with an aim to enhance the endwall heat transfer coefficient as well as leverage the conjugate heat dissipation capabilities of these "extended surfaces". Lattices on the other hand, have been investigated to a lesser degree, and some studies can be found for blade mid-chord region, however, with their manufacturability challenges at that time, the concepts did not gain traction. Lattices are far more complex topologies with superior local heat transfer characteristics as well as high conjugate heat dissipation capabilities due to large wetted surface area. With the recent

---

[4] Kaur, I., Aider, Y., Nithyanandam, K. and Singh, P., 2022. Thermal-hydraulic performance of additively manufactured lattices for gas turbine blade trailing edge cooling. Applied Thermal Engineering, 211, p.118461.
doi: 10.1016/j.applthermaleng.2022.118461

advancements in metal additive manufacturing, complex topologies such as lattices can be revisited due to high chances of their realization now. To this end, we are presenting our study on lattices additively manufactured in 420 Stainless Steel (thermal conductivity nearly twice of Inconel 718), where four different unit cell topologies, (a) Octet, (b) Tetrakaidecahedron, (c) Face diagonal-cube, and (d) Cube, were printed using Binder Jetting technology. The aim of this study is to characterize the conjugate heat transfer capabilities of these lattices manufactured in 420 stainless steel prior to conduct similar study with Inconel 718, due to relatively simpler additive manufacturing route of Binder jetting (420 stainless steel) compared to Direct Metal Laser Sintering (Inconel 718). The intended design porosity of the samples was 0.886 and the coupons had single unit cell (edge size of 10 mm) in the thickness. The steady-state experiments were conducted to evaluate the effective thermal conductivity and forced convective heat transfer performance. For forced convection, the experiments were conducted for a wide range of Reynolds numbers with air as the working fluid. Overall heat transfer coefficient, pressure drop, Nusselt number and friction factor enhancement level and pumping power requirements of these structures are presented. The implications of the porosity variation due to manufacturing process on the interpretation of relative performance trends is discussed. The effective thermal conductivity was independent of the topology for considered porosity value. Face diagonal-cube yielded the highest heat transfer and pressure drop for the investigated Reynolds number range. However, Cube provided the best overall thermal hydraulic performance value of 1.94 to 2.78 for the investigated range of Reynolds number. At fixed pumping power conditions, Cube was capable of providing the highest heat transfer coefficient.

Keywords: Gas turbine blade; trailing edge; heat transfer; lattice; Octet.

5.1 Introduction

Advanced high-pressure stage gas-turbine blades are exposed to incoming hot gases with inlet temperatures as high as ~ 1700 °C. There has been continuous effort to develop the complementary cooling techniques for efficient heat dissipation so that blade temperature can be maintained in safe operating range.

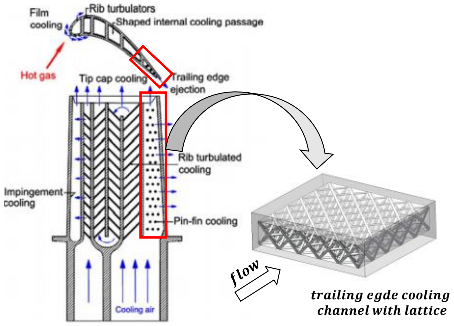

Figure 5.1 Schematic of the turbine blade [1]; also shown is the lattice structure design for the trailing edge cooling section

Considering complex contoured profile of a typical turbine blade as shown in Fig. 5.1, various types of internal and external cooling techniques have been developed over the years, depending on the local heat-load levels, space constraints, and structural integrity requirements. Designing a cooling concept for trailing edge area is challenging because the blade thickness reduces significantly in this zone allowing the fabrication of only narrow internal channels for the coolant flow. Further, it is expected from trailing edge cooling design that the blade structural integrity is not compromised. The augmentation of heat transfer from the trailing edge surface is achieved by introducing turbulence-promoting features on the internal walls of the channels.

Amongst several features, pin-fins have emerged as one of the most promising options for trailing edge because they provide high heat transfer enhancement levels. A comprehensive review on different heat transfer augmentation techniques was provided by Ligrani et al. [2].

Matrix cooling or latticework cooling is another method of augmenting heat transfer in the internal channels of the turbine blades. Relatively less attention has been given to this cooling technique as compared to pin-fin features for applications in the trailing edge cooling. Matrix cooling involves two sets of parallel ribs inclined to each other at an angle. This matrix divides the channel volume into subchannels which improves the heat transfer by enhancing the surface area, promoting crossflow interaction, changing the direction of the flow from the suction side to pressure side (vice versa), and flow impingement. Apart from providing high heat transfer augmentation, lattices lend the much-needed mechanical support to the blade structure which further establishes their suitability as cooling concepts in the trailing edge section. Bunker [3] highlighted the advantages of latticework cooling which included overall heat transfer coefficient levels comparable to the well-known turbulated serpentine channel, superior blade-strength, and robust structure realizable through investment casting manufacturing technique. Saha et al. [4] experimentally investigated the heat transfer and pressure drop characteristics of lattice structures employed in the converging channel of the trailing edge where the working fluid entered into lattices following a 90° turn. Liquid crystal thermography was used to determine local heat transfer coefficient distribution. The two-inlet lattice channel provided higher overall thermal-hydraulic performance than the pin-fin configuration for the investigated range of Reynolds number. The heat transfer augmentation provided by the two-inlet lattice was 2.1 to 3.4 times of the smooth channel. Acharya et al. [5] studied the effect of channel rotation on the heat transfer of channels featuring lattice for a wide range of Reynolds number and rotation number. The authors observed uniform heat transfer distribution for Reynolds number greater than 20,000. Rotation number and density ratio had negligible effect on heat transfer for Reynolds number greater than 20,000. Oh et al. [6] also determined the heat transfer and friction loss characteristics of rotating matrix cooling channel using naphthalene sublimation technique. For rotating configurations, the Sherwood number ratio increased with increasing rotation number on the leading surface but the effect on the trailing surface was insignificant. Tsuru et al. [7] used Magnetic Resonance Imaging (MRI) technique to visualize the flow field in a lattice channel with copper sulfate aqueous solution as the working fluid. The investigation revealed the formation of longitudinal vortex features in each subchannel, the spread of which was reported to be influenced by the rib inclination angle. Bu et al. [8] found the streamwise vortex features in subchannels because of sidewall turnings which caused high heat transfer values at the entrance of every subchannel. Du et al. [9] analyzed the effect of clearance between the two sets of inclined rib and rotation number on the heat transfer and flow structures in a latticework channel. Various flow configurations can be identified for latticework cooling depending on how the fluid enters the matrix. Luo et al. [10] numerically investigated three such configurations, viz. (a) radial flow configuration, (b) cross-flow configuration, and (c) turning flow configuration. Non-uniform flow distribution in turning flow configuration provided less uniform heat transfer in comparison to the other two configurations. For the same mass flow rate, radial flow configuration provided the highest heat transfer and flow losses. Carcasci et al. [11] investigated the effect of rib-height, rib-thickness, and number of subchannels on the overall thermal hydraulic performance of latticework channel for cooling applications in the mid-chord and trailing edge sections of the turbine blade.

Above studies demonstrate the potential of lattice structures as effective cooling concepts in the turbine blades. The studies mentioned above focused on the traditional inclined subchannels as latticework in the cooling channels. Lattice frames composed of relatively complex unit-cell topologies have been rarely investigated in the past for turbine applications. One such study was by Shen et al. [12] who numerically analyzed the thermal performance of wedge-shaped cooling channel consisting of different numbers of rows of Kagome-shaped unit cells as turbulence promoters. The performance of the Kagome-shaped lattice in trailing edge channel was then compared with the pin-fin configuration. Nusselt number of the three-array Kagome configuration was higher than two and three arrays of pin-fins. This study suggests that incorporating lattices composed of periodically organized unit cells made from well-defined unique arrangement of fibers can be very effective in augmenting heat transfer in trailing edge section. The rib latticework and Kagome-shaped cells can be traditionally cast-integrated into the channels of the turbine blade while manufacturing. However, the traditional technologies impede the realization of architecturally more complex unit-cells. Additive manufacturing technology has emerged as an alternative route to manufacture such lattices with advanced unit-cell topologies. Many recent studies have focused on analyzing the hydraulic and thermal performance of additively manufactured lattices and some prominent studies of the additively manufactured lattice coupons are discussed below. However, it should be noted that not all of these studies necessarily catered to the turbine applications.

Parbat et al. [13] performed steady-state heat transfer experiments on coupons composed of Kagome-shaped unit cells additively manufactured in Inconel 718 material for turbine blade cooling. In this single-cell thick sandwich configuration, heat transfer augmentation of ~ 4 to 5 times was observed with the corresponding increment of ~ 30 to 50 times friction factor as compared to the smooth channel. Although the reported roughness of the samples were ~ 28.45 μm, the enhancement of the samples was compared to the smooth channel data predicted by

Gnielinski correlation, thus the overall reported enhancement accounted for the manufactured rough endwalls as well. Chaudhari et al. [14] investigated Octet lattice having three different porosities ranging between ~0.70 and 0.91 printed in aluminum alloy. Corresponding effective stagnant thermal conductivity (k_{eff}), inertial coefficient, friction factor, and Nusselt number were reported by the authors. The endwall effects in sandwich configuration having Face-centered cubic (FCC) lattice with three different types of fiber designs printed in epoxy resin were visualized using Transient liquid crystal (TLC) technique by Liang et al. [15]. Elliptical fibers yielded higher Nusselt number as well as friction factor in comparison to rectangular and circular fibers.

Many studies have investigated samples which have unit-cells periodically arranged in the three-dimensions as opposed to single cell thick configurations. Broughton and Joshi [16] compared the pressure gradient and Nusselt number obtained from additively manufactured Rhombic-dodecahedron lattice with that of the stochastic metal foams having similar porosity, fiber-diameter, and cell-size. The Rhombic-dodecahedron lattice printed in aluminum alloy demonstrated 60% and 66% higher heat transfer coefficient and pressure drop, respectively, as compared to metal foams. Ho et al. [17] employed the Rhombi-octet lattice in a commercial scale heat exchanger to enhance the air-side heat transfer. Additively manufactured lattice heat exchangers yielded in better thermal performance as compared to commercial fin-and-tube heat exchanger. Octet lattice printed in aluminum alloy was subjected to pool boiling conditions by Wong and Leong [18], who observed heat transfer coefficient enhancement of about ~ 2.81 times of the plain surface.

Montazerian et al. [19], Du et al. [20], Timercan et al. [21], and Ali and Sen [22] numerically and experimentally investigated the mechanical and permeability characteristics of different lattices such as Cube, Rhombic-dodecahedron, Diamond, Octet, and tetrakaidecahedron

(TKD). Numerical analysis of heat transfer in different lattice topologies that could be printed by additive manufacturing has been conducted by several authors. Kaur and Singh [23] investigated the heat transfer coefficient and pressure drop characteristics of Octet, Face diagonal-cube (FD-cube), TKD and Cubic lattices to establish that the interfacial heat transfer coefficient of Octet was the highest amongst all the topologies. TKD is recognized as one of the topologies that bears strong resemblance to the real structure of stochastic metal foams and regular arrangement of TKD unit cells has been studied in the past [24]. Kaur and Singh [25] reported the conjugate thermal performance of Octet lattice in single-cell thick configuration with water as the working fluid for electronics cooling applications. Further, the endwall heat transfer of Octet, Octa and V-Octet lattice in a unit aspect ratio channel was reported by the group [26] using transient liquid crystal (TLC) technique and numerical simulations were performed to analyze the heat transfer mechanism for fully turbulent flows. The above studies established that near-wall flow physics significantly influence the endwall characteristics besides the conjugate thermal exchange happening at the strut-fluid interface in the regions away from the endwalls. Singh and group [27] performed experimental investigation on thick blocks of three-dimensionally reticulated Octet, FD-cube, TKD, and Cube lattices, where the streamwise development of endwall heat transfer coefficient was reported. The thermal performance of Octet, FD-cube, and TKD in the periodic heat transfer zone was similar. It was shown that with the choice of pore-scale dimensions such as pore-diameters and fiber-diameters as characteristic length-scales, the Nusselt number of all the topologies could collapse to a single trendline. To the best of author's knowledge, this was the first work to address the periodic heat transfer aspect in additively manufactured blocks of the investigated topologies. Recently, Kaur and Singh [28] conducted numerical investigation on three-dimensionally periodic unit cells of Octet, TKD, and Rhombic-dodecahedron in laminar regime with air as the working fluid. Higher heat transfer coefficient was generally encountered on the upstream faces of the fibers prone to the impingement of the incoming flow. Highest mean interfacial heat transfer coefficient was obtained for Rhombic-dodecahedron, followed by Octet and TKD. The pore diameter as characteristic length scale provided singe trendlines for interfacial Nusselt number for all the topologies.

In a recent comprehensive review on the state-of-the-art in additively manufactured heat exchange applications, Kaur and Singh [29] highlighted the role of additive manufacturing in the field of turbomachinery. Additively manufactured internal cooling channels, film cooling holes, and transpiration cooling configurations have been explored by the authors [30–32]. Kirsch and Thole [33] recently investigated additively manufactured pin-fin array and pointed out the importance of inherent surface roughness considerations in characterizing the performance of additively manufactured samples. Despite many existing studies on additively manufactured lattices, the thermal-hydraulic performance of the lattices has been reported to a lesser degree. Moreover, the roughness in lattices printed via additive manufacturing is also an important consideration in heat transfer analysis which makes the experimental investigation on them very crucial. The experimental data reveals the actual thermal-hydraulic characteristics of lattices which can have deviations from predictions on smooth CAD models.

This study investigates the thermal and hydraulic performance of four different regular lattices, namely, Octet, TKD, FD-cube, and Cube, printed in 420 Stainless Steel (infiltrated with Bronze) through Binder Jetting process. The single-cell thick lattice configuration appropriate for trailing edge cooling channel with the dimensions of 50 mm x 50 mm x 10 mm (L x W x H) were manufactured with channel aspect ratio (width-to-height) of 5:1. The lattice structure was manufactured as an integrated structure with two substrate endwalls on which constant heat flux boundary condition was imposed to obtain the thermal performance of the lattices. Two types of heating configurations were explored in the current investigation, i.e., (a) both endwalls heated, and (b) single endwall heated. The primary focus of the current investigation is to establish the suitability of lattices for turbine blade cooling applications; however, the results can be extended to electronics package cooling applications as well where single wall heating-type conditions are commonly encountered. Stainless Steel was chosen as a precursor to a follow-up study on Inconel 718 to rank the topologies based on their thermal hydraulic performance and using the findings of this paper to make design decisions, on whether or not, Laser Powder Bed Fusion based printing in Inconel 718 is required to further explore above topologies or conventional fabrication methods would suffice. The motivation behind this study is to also evaluate the performance-to-cost metric of proposed cooling designs, where additive manufacturing in its current state, is definitely more expensive and less scalable. Following sections provide details on the experimental setup, unit cell topology description, heat transfer coefficient calculation methodology, followed by results and some conclusions.

5.2 Description of the test samples

Figure 5.2 shows the investigated test samples printed in 420 Stainless steel (infiltrated with Bronze) through Binder Jetting process. The material matrix was composed of 60% Stainless steel and 40% Bronze. The surface finishing of the test samples was achieved through bead-blasting process. Figure 5.3 shows the four different unit cell topologies that were investigated, viz. Octet, TKD, FD-cube, and Cube along with the schematic of the samples with relevant dimensions. FD-cube was obtained by linearly translating single face-diagonal unit cell in a periodic fashion resulting in the formation of *‘cross of diagonal fibers’* with four small triangular opening at the mating plane of adjacent cells (Fig. 5.3a).

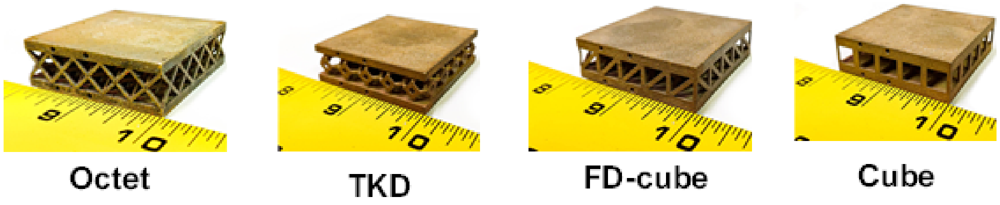

Figure 5.2 Test samples additively manufactured in 420 Stainless Steel with Bronze infiltration via Binder Jetting process

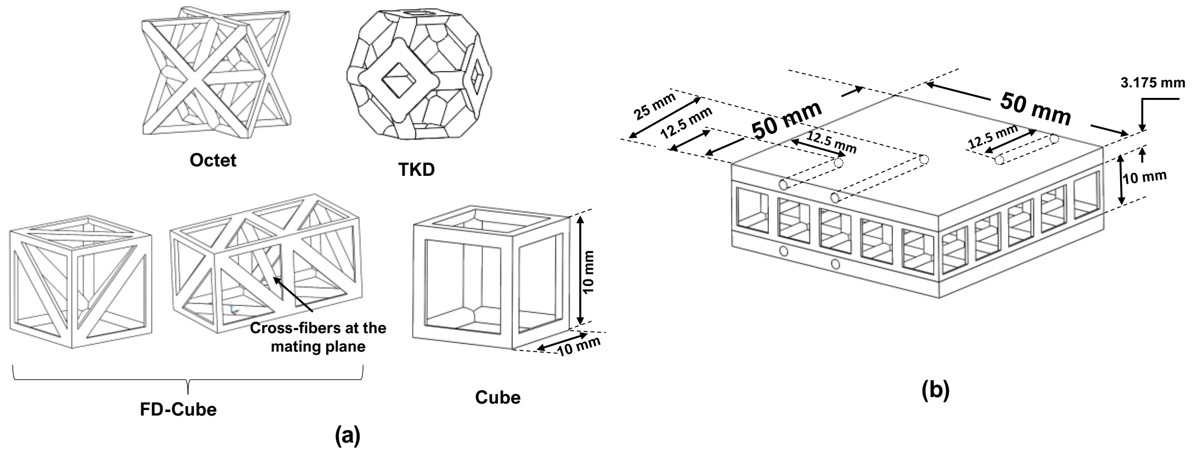

Figure 5.3 (a) Unit cell topologies of the investigated samples, (b) schematic of the samples showing important dimensions

The overall dimensions of the lattices were 50 mm x 50 mm x 10 mm. The unit-cell size was 10 mm and there were five unit-cells in streamwise and spanwise direction. The substrate wall thickness on the upper and bottom side of the lattice was ~ 3.175 mm which was provided with cylindrical slots of ~ 1.905 mm diameter for thermocouples. The designed porosity of the samples was ~ 0.886 and the corresponding intended fiber diameters are reported in Table 5.1. The table also shows the measured porosities of the as-printed samples. The measured porosities were about ~ 1% to 7.1% deviated from the intended porosity of ~ 0.886. Amongst the printed samples, Octet showed the maximum deviation of ~ 7.1% and the Cube exhibited the least deviation of ~ 1%. Cube provided the porosity value closest to the design porosity and the porosities of TKD and FD-Cube were 2.3% and 0.9% lower than the Cube topology. The thermal-hydraulic performance of TKD, FD-cube, and Cube obtained from the experiments of these three test samples could be compared fairly at similar flow conditions. However, commenting on the relative performance benefits of the Octet topology with porosity difference of 6.1% from the Cube topology was not deemed suitable. The first iteration of printing provided information on the expected percentage deviation in the morphological characteristics of the samples. Considering the occurrence of anomalies in structure while printing, another Octet CAD model was prepared for printing with porosity of ~ 0.93. Octet sample manufactured using 0.93 designed porosity had an actual porosity of ~0.888, which was similar to previously printed (1st batch) TKD, FD-cube, and Cube samples. The final experiments were therefore conducted on five different samples including two for Octet (measured porosities of 0.823 and 0.888) and one each for TKD, FD-cube, and Cube with relatively similar measured porosities as listed in Table 5.1.

Table 5.1 Fiber diameter and measured bulk porosity of the investigated samples

Topology	Fiber diameter	Measured bulk
Octet	1.00 mm	0.823
TKD	1.43 mm	0.856
FD-cube	1.54 mm	0.869
Cube	2.37 mm	0.877

X-ray Computed Tomography (CT): Additively manufactured samples often deviate from the intended CAD models. Hence it is imperative to characterize the local defects/deviations and their cumulative effect on bulk properties such as porosity. The CT data was obtained using Nikon's XTH225ST system with a 225KV rotating target. The high-resolution images were obtained using scanning voltage of 220 KV, 170 μA current, and exposure time of 708 ms. Figure 5.4 shows the CT scan images of Octet (porosity = 0.823) and TKD (porosity = 0.856) samples. The fibers by design were cylindrical in shape (Fig. 5.3), however, the CT scan images reveal that the printed fibers did not exactly retain their intended smooth configuration, and moreover, there were local defects prevalent over the entire sample with some instances of identifiable ones (missing material zone identified in Fig. 5.4a). These anomalies in the samples contribute to the deviation in transport properties predicted by computations carried out on intended CAD models.

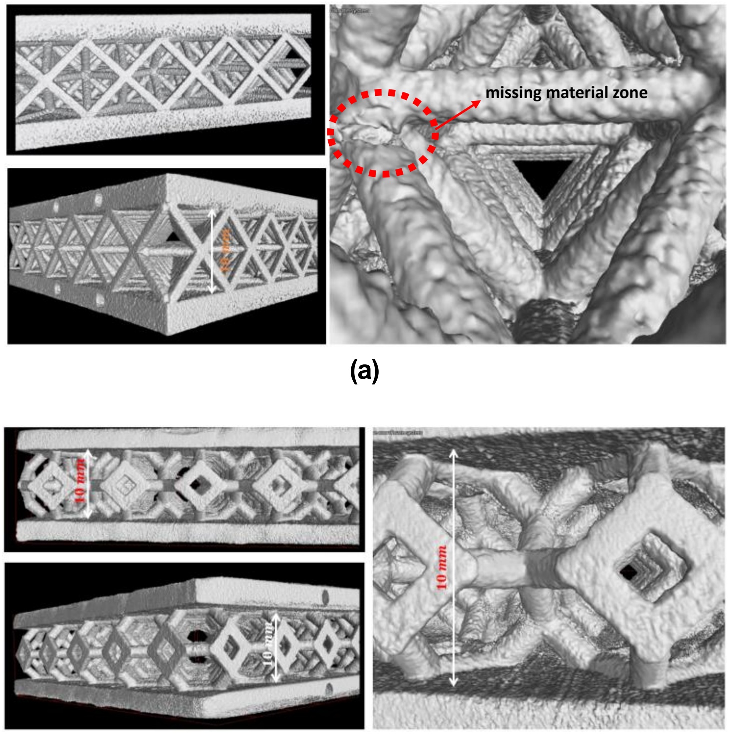

(a)

(b)

Figure 5.4 CT-scan reconstruction of (a) Octet, and (b) TKD samples

5.3 Experimental set-up

k_{eff} experiments

The effective thermal conductivity (k_{eff}) of the 420 Stainless Steel samples shown in Figs. 5.2 and 5.3 with air as the working fluid was measured through the steady-state experiments described in detail in a previous work by the authors [34]. The solid thermal conductivity (k_s) was also measured experimentally to thoroughly characterize the material properties.

Forced convection experiments

Figure 5.5a shows the 2D-schematic of the experimental facility. Air was drawn from a reservoir held at a constant pressure and connected to a compressor set to deliver air at 1 MPa. The desired air flow rate was then set using a pressure regulator installed upstream of an ASME orifice plate where flow rate was metered. The pressure differential (Dwyer 477 AV-2 (0-10 kPa)), static air-pressure (Dwyer DPG-002 (0-100 kPa)) and the temperature of the air passing through the orifice plate was recorded to determine the mass flowrate using an in-house MATLAB code. After flow-metering through the orifice-plate, the air was directed towards the test-section where the transition of the circular pipe of ~ 25.4 mm diameter to 50 mm x 10 mm cross-section of the test section was achieved with the help of a diffuser.

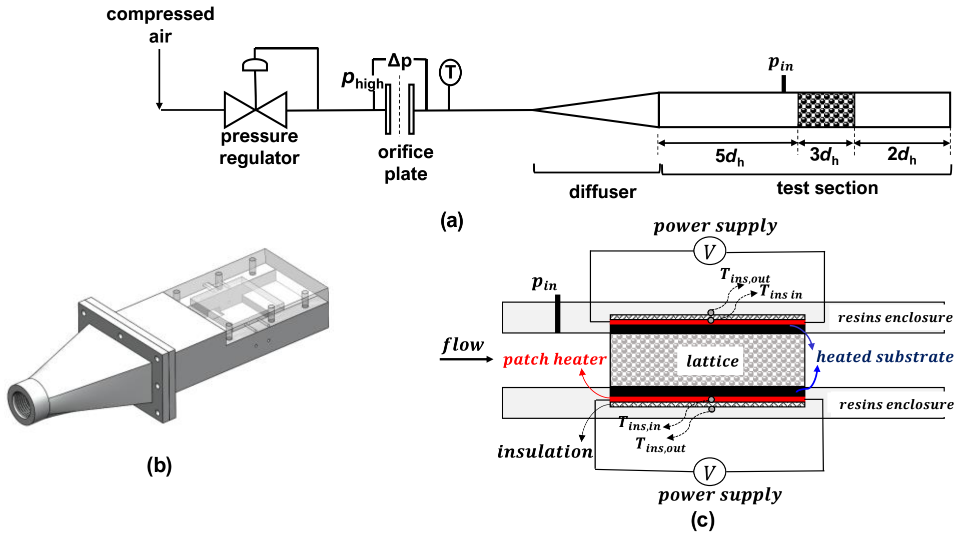

Figure 5.5 (a) Schematic of the experimental set-up, (b) test-section along with attached diffuser section for smooth flow transition, (c) schematic of the heater-lattice assembly used for the test-runs

Figure 5.5b shows the isometric view of the diffuser and test-section assembly. The components of this assembly were manufactured using resin via Stereolithography (SLA) process through a Form 3 printer. The test-section was ~ $10d_h$ long and had the cross-section of 50 mm x

10 mm. The lattice samples were placed ~ $5d_h$ downstream of the test-section inlet and ~$2d_h$ exit length was provided at the end to prevent the influence of ambient conditions on the heat transfer measurements.

The heater and test-sample assembly is presented in the Fig. 5.5c. Patch heaters were glued to the substrate walls with the help of RTV (room temperature vulcanizing) silicone to provide uniform heat flux boundary condition. For double-wall heating experiments, similar heat flux values were maintained on the upper and lower substrate walls, whereas in single wall-heating conditions, only one wall (bottom) was heated, and the other was held adiabatic by providing the insulation. The backside of the heaters was covered with Styrofoam insulation having thermal conductivity of ~0.037 W/mK to minimize the heat losses.

5.4 Experimental method and data reduction

As mentioned above, the details for the k_{eff} measurement procedure are provided in prior published work of the authors [34] and will be omitted here in the interest of brevity. The methodology adopted to evaluate the flow and forced convection thermal characteristics of the investigated lattices is discussed below.

Steady-state heat transfer experiments were conducted where required flow conditions were set first, followed by suitable heat load at the top and bottom walls. The top and bottom walls of the lattice samples were subjected to constant heat flux boundary condition, where heat was supplied through a patch heater glued perfectly with both the walls. The heaters were connected to DC power supply with high accuracy 3-decimal places current output, which was used for heat transfer coefficient calculations described later. On the back side of the two heaters, an insulation was glued to minimize the conduction losses. This heat loss was also calculated by measuring temperature difference across the insulator. Maximum heat loss observed did not exceed ~5% of the total heat supplied. Once the steady-state was reached, the temperature measurements at the sample and insulation were carried out, along with the air temperature at the inlet of the test section. The supply pressure was also measured at this time.

Overall conjugate heat transfer was measured through the control volume analysis which encompasses the effects of flow, lattice structure, working fluid, and the solid-material. The heat supplied to the system from one of the substrate walls was calculated as:

$$Q_{C.V.} = (I^2 R_{htr}) - (Q_{l,ins}) \tag{5.1}$$

where, $Q_{l,ins}$ was the heat loss through the backside insulation measured using Fourier's law. The net heat input $Q_{net,C.V.}$ into the lattice during double wall heating conditions was taken as summation of $Q_{C.V.}$ from the top and bottom substrate walls. The exit bulk-temperature was obtained from the energy-balance method as following:

$$T_{b,L} = T_{in} + \frac{Q_{net,C.V.}}{\dot{m} c_p} \tag{5.2}$$

where $\dot{m}$ and c_p were the mass flow rate and specific heat capacity of air, respectively. Linear variation of the bulk temperature ($T_{b,x}$) with respect to streamwise distance was obtained using the inlet (x = 0) and exit (x = L) temperatures. Length averaged bulk temperature defined below was taken as the reference for heat transfer coefficient:

$$T_{ref} = \frac{1}{L} \int_0^L T_{b,x} \, dx \tag{5.3}$$

The overall/global heat transfer coefficient was then determined as following:

$$h = \frac{Q"_{net,C.V.}}{\left(\tilde{T}_w - T_{ref}\right)} \tag{5.4}$$

where, $\tilde{T}_w$ was the average wall temperature and $Q"_{net,C.V.}$ was the net heat flux supplied to the system. The Nusselt number was then defined as:

$$Nu = \frac{h\, d_h}{k_f} \tag{5.5}$$

where, k_f was the air thermal conductivity.

The measurement uncertainty analysis was carried out through sequential perturbation method [35] .The typical uncertainty range for Nusselt number was between 2-5% and that for the Reynolds number was within 4%.

5.5 Results and discussion

This section presents the effective thermal conductivity (k_{eff}), forced convective heat transfer (h), pressure drop, and thermal-hydraulic performance of the investigated lattices. The pumping power requirements for each lattice are also reported.

5.5.1 k_{eff} measurements

The k_{eff} measurements were conducted at three different heat flux levels to ensure that the obtained values were only dependent on the solid material property and the lattice topology. Figure 5.6 shows the variation of $k_{\text{eff}}/k_{\text{s}}$ ratio for different heat flux conditions. In-house measurements were carried out to determine the solid material thermal conductivity (k_s) and was found to be 20.8 W/mK [34]. The measured k_{eff} values were nearly constant for respective topologies throughout different steady-state experiments. The average values of $k_{\text{eff}}/k_{\text{s}}$ were 0.079, 0.065, 0.059, and 0.055 for Octet, TKD, FD-cube, and Cube, respectively. Earlier studies found that the $k_{\text{eff}}/k_{\text{s}}$ of the metal foams is independent of cell sizes (at any given porosity) and is influenced only by the porosity variation for fixed solid material [36]. Wang et al. [34] also suggested that the k_{eff} of the regular lattices was not a strong function of topology for porosities around 0.90 and above through simulations. The difference in the relative magnitudes of k_{eff} between different configurations herein is, therefore, attributed to the difference in their respective porosities. Note that the intended porosity was same for each 3D printed configuration, however, the porosities of the actual parts had significant deviations. If one has to obtain uniform porosity for each configuration, there has to be a trial-and-error method for each configuration, since the deviations in the porosity values we observed were random in nature. In order to facilitate a direct comparison of k_{eff} values of different configurations at same porosity, we adopted a computational route instead. Steady-state heat transfer simulations were conducted in finite-volume solver FLUENT with procedure delineated by Ekade at al. [37]. Firstly, the computational model was validated with experimental data by creating unit cell topologies matching the porosities of the 3D printed parts. Table 5.2 shows a comparison between experimental and computational results.

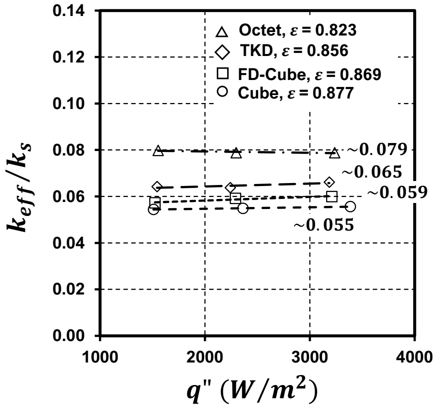

Figure 5.6 Variation of $k_{\text{eff}}/k_{\text{s}}$ with respect to the supplied heat flux

Table 5.2 Comparison of $k_{\text{eff}}/k_{\text{s}}$ obtained from experiments and computations

Topology	Porosity (ε)	Experiments	Computations	% Difference
Octet	0.823	0.079	0.080	1.26 %
TKD	0.856	0.065	0.067	3.08 %
FD-cube	0.869	0.059	0.058	1.69 %
Cube	0.877	0.055	0.055	~0%

The validated computational model was then extended to find k_{eff} values at a fixed unit cell porosity of 0.886. At fixed porosity of 0.886, the k_{eff} values yielded by each topology was same establishing that for the investigated porosity range, the k_{eff} is indeed independent of topology. The $k_{\text{eff}}/k_{\text{s}}$ values for all the topologies at porosity of 0.886 was ~ 0.049. Figure 5.7 shows the contours of solid, and fluid (occupying void space and modeled as stagnant) temperatures obtained from the simulations of unit cells for each topology at designed porosity (~0.886) for the case of $k_s = 20.8\, W/mK$ and $k_f = 0.026\, W/mK$. In these simulations, local thermal equilibrium ($T_{\text{s}} = T_{\text{f}}$) has been employed due to heat flux and temperature continuity at the interface. The direction of heat flow in Fig. 5.7 is from right to left. For all topologies, the solid-phase temperatures at the fiber junctions were similar to the fiber upstream, i.e., a smooth temperature profile was observed. This included the X-shaped fiber formation at the four side walls of Octet lattice. The temperature variation along the fibers can have a prominent role to play in high temperature applications involving thermal stresses.

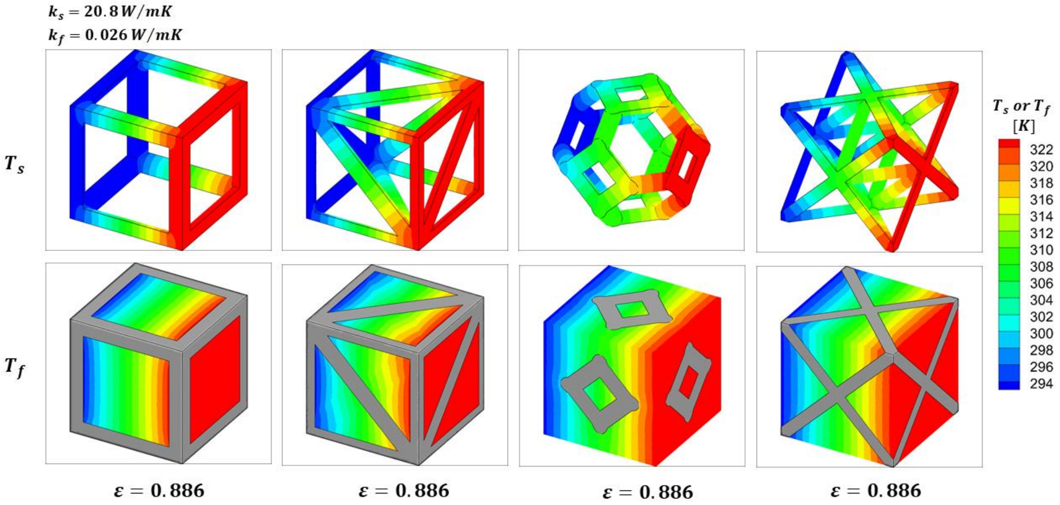

Figure 5.7 Solid and fluid temperature contours for topologies with designed porosities for (left to right)- Cube, FD-cube, TKD, and Octet

5.5.2 Heat transfer coefficient vs mean flow velocity

Figure 5.8 shows the variation of heat transfer coefficient with respect to the mean flow velocity ($\dot{m}/\rho A_c$) for all the investigated topologies for both-walls (Fig. 5.8a) and single-wall (Fig. 5.8b) heating configurations. To facilitate discussion of the samples in this section, Octet topologies will be denoted by their names followed by parenthesis containing the corresponding measured porosity value. A power law dependence was observed between h and u, which is observed in typical enhanced heat transfer studies. Octet (0.823) had the maximum heat transfer coefficient followed by FD-cube, TKD, and Cube, respectively. The relative trends of the heat transfer performance were almost consistent for both heating conditions. The topologies render unique flow characteristics on the planes parallel and normal to the mean flow direction. Kaur and Singh [23] numerically investigated the flow losses and interfacial heat transfer characteristics of the four topologies considered in the present study for a single cell thick lattice in streamwise direction and also presented the qualitative comparison of flow with the corresponding fully periodic unit cells of each topology. The simulations were conducted for laminar flow conditions. Localized flow accelerations were apparent around the Octet fibers in the normal planes whereas large recirculating fluid pockets were found downstream of the fibers in the streamwise planes. TKD in [23] was generated through sphere extraction method which resulted in triangular cross-section of fibers and also demonstrated large zones of fluid recirculation. The flow features involving wake formation are expected to be more prominent for turbulent flows and essentially dictating the flow losses and heat transfer characteristics of each topology. Upstream zones of the fibers facing directly the incoming flow have very high heat transfer coefficient values due to fluid stagnation whereas the recirculation zones result in lower levels of heat transfer coefficient. However, it should be noted that ranking of interfacial heat transfer coefficient cannot be directly translated to the ranking of topologies in conjugate scenarios, especially in single cell thick lattices because the endwall-lattice interactions become increasingly important in such configurations besides the flow phenomenon in the core volume of the lattices. In experimental and numerical study by Kaur and Singh [26], it was demonstrated that the fiber junctions with endwall for different lattices from Octahedron family have capability of inducing endwall heat-transfer coefficient signature similar to that of ribs and pin-fins.

Octet (0.823) showed significant difference between the both-wall and single-wall heating configurations as compared to the other topologies. TKD and FD-cube had very similar heat transfer coefficient values whereas Cube had the potential to outperform the TKD structure at very high mass flow rates. Cube had slightly higher porosity than TKD in the present investigation and the heat transfer coefficient is expected to increase with decreasing porosity value due to increase in effective thermal conductivity and specific surface area for thermal exchange. Therefore, at same porosity, additively manufactured simple Cube topology can perform slightly better than the TKD topology for high mass flow rate values. The thermal performance of FD-cube was comparable to TKD and FD-cube at the lower mass flow rates, but significant deviation of relative performance was obtained at the higher mass flow rate range. The porosity of FD-cube was lower than Cube, therefore, relatively higher heat transfer coefficient was expected for FD-cube. On the contrary, FD-cube had ~ 1.4% higher porosity value than TKD topology but still exhibited significantly higher heat transfer coefficient values. Since the measured porosity values have minimal deviations, the relative performance of TKD, FD-cube, and Cube obtained in the present study was expected to be a function of the topology which governs the associated flow dynamics, conjugate thermal exchange and near endwall flow physics, rather than only porosity variation.

The results obtained in the current investigation are for the thermally developing flow. Such a flow is expected in a typical gas turbine blade.

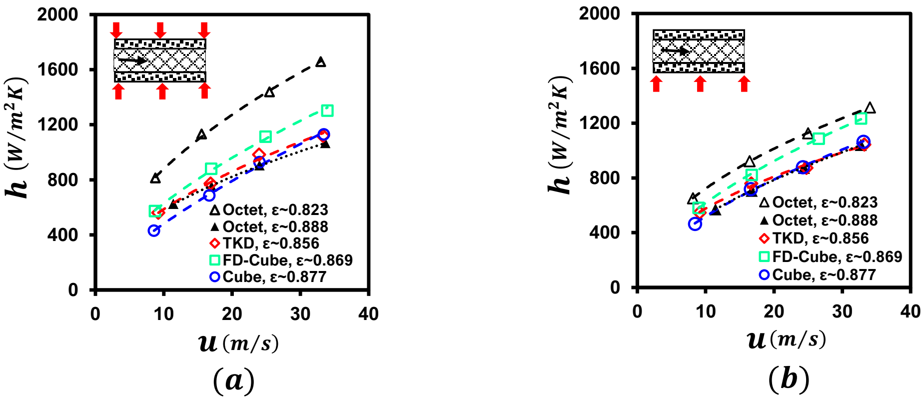

Figure 5.8 Heat transfer coefficient as a function of the mean flow velocity with heating on (a) both the walls, and (b) single wall

From the discussion presented thus far, it is concluded that amongst TKD, FD-cube and Cube topologies, FD-cube would be the most viable choice if achieving high heat transfer coefficient is the constraint of design considerations. TKD would be the least preferable choice for designing such compact heat transfer augmentation channels operating for high mass flow rates of coolant. An important aspect of the results provided in the Fig. 5.8 was that they included the effect of surface quality rendered by the additive manufacturing process. Quantification of surface roughness and its role in further enhancement in heat transfer was not in the scope of this study, however it is highly recommended.

Figure 5.8 also shows the thermal performance of Octet (0.823) and Octet (0.888), where Octet (0.823) had the best thermal performance trend because of the lowest porosity value. For both-wall heating configuration, about 30% to 59% of higher heat transfer coefficient values were obtained for Octet (0.823) as compared to Octet (0.888), whereas the increment was ~14% to 30% for single-wall heating configuration. Significant difference in heat transfer performance of Octet was observed for variation of ~ 7.9% in the porosity values. The thermal performance of Octet (0.888) was comparable to TKD (0.856), FD-cube (0.869), and Cube (0.877) which indicates that if the measured porosity was not taken into consideration, Octet could have been considered as the best thermal performance yielding configuration. Two aspects have to be considered here: (a) if one needs to rank different topologies for their thermal performance at same porosity, then iterative approach has to be followed to get similar porosities as the deviations are structure-dependent, and (b) if one prints a single batch of lattices with as-designed porosity without consideration of the manufacturing-induced deviations/defects to run experiments, then the conclusions drawn will not be an attribute of topology alone but inherent anomalies. The repeatability of such data in engineering applications is questionable as the structural anomalies will vary with different process parameters/procedure and so does the actual porosity value. Such ranking of topologies in real-world application will become inconsistent, especially when there is continuous effort to optimize currently available additive manufacturing technologies. In the current study, the former of the above two methodologies has been adopted to draw conclusions, but with an assumption that local roughness profile at investigated geometrical dimensions will induce same scale of effect on the final relative performance across different lattices.

5.5.3 Nusselt number enhancement values vs Reynolds number

Figure 5.9 shows the Nusselt number enhancement trends as a function of the channel Reynolds number for all the topologies under both types of heating configurations. The enhancement in heat transfer provided by the topologies was obtained relative to the Dittus-Boelter correlation ($Nu_0 = 0.023Re^{0.8}Pr^{0.4}$) for turbulent flows in smooth channels. All the samples exhibited decreasing trend of heat transfer enhancement levels with respect to the increasing Reynolds number, which is again typical of enhanced heat transfer studies, e.g., rib turbulators, dimples etc. Octet (0.823) provided the highest heat transfer enhancement with respect to the smooth channel data. Amongst the group of samples with similar porosity values, FD-cube provided the heat transfer enhancement of 9.47 to 12.36 times of the smooth channel for both-wall heating configuration. The other three topologies had enhancement levels from 9 to 11 times in reference to smooth channel. Single wall heating condition enhancement levels were slightly lower than that of the double wall heating. Note that these enhancement levels are obtained for solid thermal conductivity of 20.8 W/mK and the experiments were conducted such that the conjugate heat transfer effects could be included. If the experiments were to be carried out for Inconel 718 which has a thermal conductivity of ~11 W/mK, the heat transfer enhancement levels would undergo significant reduction.

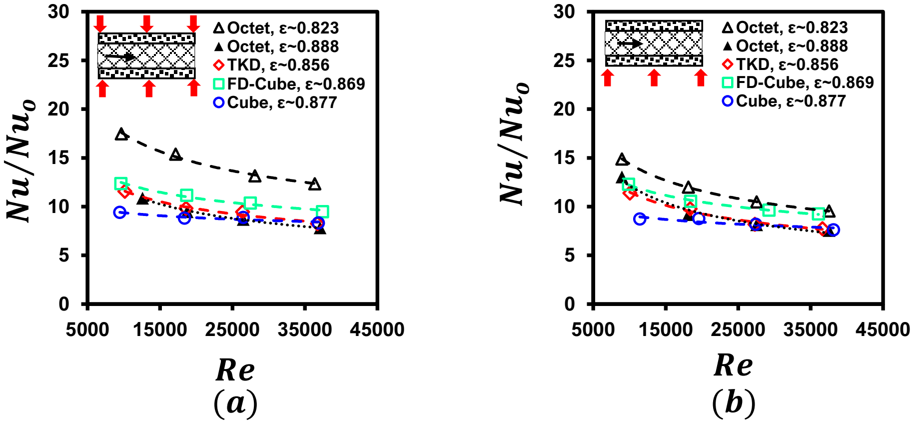

Figure 5.9 Nusselt number enhancement values for heating on (a) both the walls, and (b) single wall, with respect to thermally fully developed flow in smooth channel as predicted by Dittus-Boelter correlation

Figure 5.9 provides heat transfer augmentation levels with respect to Nusselt number values obtained using Dittus-Boelter correlation proposed for hydrodynamically and thermally fully developed turbulent flows in a smooth channel. Since the length of the samples investigated in the present study was ~ 3 d_h, the flow over this heated short streamwise length would still be in thermally developing stage. The Nusselt number values obtained from a smooth channel having length of ~ 3 d_h in the flow direction (similar to additively manufactured coupons) can serve as more appropriate baseline case for evaluating the actual thermal performance enhancement capabilities of the investigated lattices. To this end, numerical simulations were conducted on the channel configuration exactly similar to the experimental test section schematic provided in Fig. 5.5 to obtain the streamwise length-averaged Nusselt number (Nu_s) with constant heat flux boundary condition. The Nusselt number was obtained with respect to two heating configurations, i.e. (a) both walls heated, and (b) one wall heated. The numerical simulations were performed with k-ω SST turbulence model over the investigated range of Reynolds number in Ansys Fluent 2021 R1 (academic license). Figure 5.10 provides the Nusselt number enhancement of the lattices with respect to the simulated developing flows over the smooth plate in a channel. Figures 5.9 and 5.10 show that the thermal augmentation can be overestimated if comparison is drawn with respect to the Dittus-Boelter correlation. The Nusselt number enhancement of all the investigated topologies with Dittus-Boelter as baseline case (Fig. 5.9) was nearly ~ 1.4 to 1.6 times higher with respect to values that accounted for the developing flow conditions (Fig. 5.10).

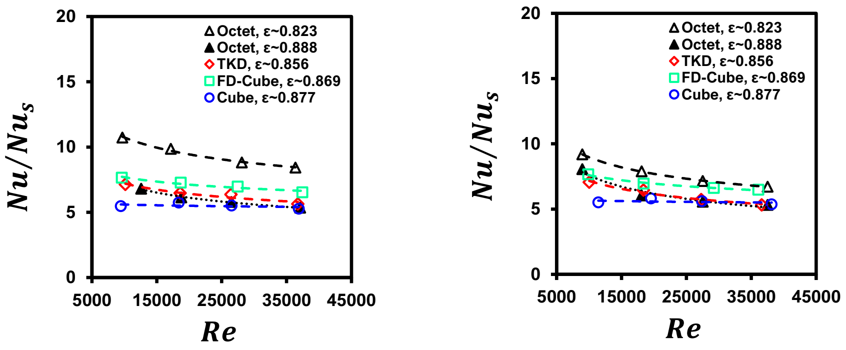

(a) (b)

Figure 5.10 Nusselt number enhancement values for heating on (a) both the walls, and (b) single wall, with respect to thermally developing flow in a smooth channel

5.5.4 Pressure drop characteristics

Lattices are expected to impose larger pressure drop for a certain flow rate when compared to other heat transfer enhancement concepts such as rib turbulators, dimples/protrusions. The basic flow mechanism in lattices is of the flow stagnation type where the fibers provide flow blockage, which in turn also increases the heat transfer, but at an expected cost in terms of increased pressure drop. In heat exchanger concept development, it is imperative to evaluate the enhancement in heat transfer with the associated pressure drop or pumping power penalty.

Figure 5.11a shows the pressure gradient variation with mean flow velocity and Fig. 5.11b shows the corresponding friction factor ($\Delta P d_h/2L\rho u^2$) variation with Reynolds number. Octet (0.823) and FD-cube had the similar pressure drop characteristics, but FD-cube had significantly higher porosity than Octet. It means that if Octet and FD-cube were to have the same measured porosity then FD-cube would incur higher flow losses. This can be affirmed from the pressure drop values of Octet (0.888) relative to FD-cube. The pressure gradient trendline corresponding to Octet (0.869) lattice having porosity equal to that of the investigated FD-cube sample should lie within the pressure gradient bracket of Octet (0.823) and Octet (0.888) shown in Fig. 5.11a, i.e. beneath the current FD-cube trendline. In a previous numerical study by the authors [23], Octet was reported to have higher pressure drop than FD-cube because configurations consisted of single cells in streamwise direction due to which the effects of fiber cross-section at mating planes of the cells could not be manifested for FD-cube in the mean flow direction.

From the above discussion, it can be concluded that for any fixed porosity value (say 0.886), the actual pressure drop trend is expected to be: the highest values for FD-cube followed by Octet, TKD, and Cube, respectively. Each topology consists of uniquely shaped pores through which the fluid flows. Cube was the most permeable to the fluid yielding minimum resistance to the fluid flow due to which the pressure gradient incurred by Cube was the lowest. TKD topology was slightly more complex than the Cube, but the square and hexagonal pore openings of the cell provided a fairly wide area to the fluid flow. Numerical investigations in [23] also revealed the pressure gradient of Octet to be higher than TKD. Octet had architecturally the most complex fiber connections within the volume of the unit cell which posed high resistance to the fluid motion. FD-cube did not have the fiber connections within the whole unit cell volume like Octet but the formation of cross-shaped fibers at the mating plane of two adjacent unit cells resulted in very small openings for the fluid flow and increased losses due to flow stagnation. Two flow parameters required to characterize the flow losses of porous media are permeability and inertial coefficient. The inertial effects become prominent at high fluid velocities due to which the pressure drop trends of lattices cannot be justified through permeability values alone. A structure having similar permeability values can still tend to yield very different inertial losses which could become increasingly dominant in dictating the pressure drop values with increasing flow velocities. The inertial coefficient factor has to be weighed-in to discuss the pressure penalty, especially at the mass flow rates being investigated herein. Therefore, both structure dependent (including the roughness) permeability and inertial coefficient are responsible for the trends shown in Fig. 5.11.

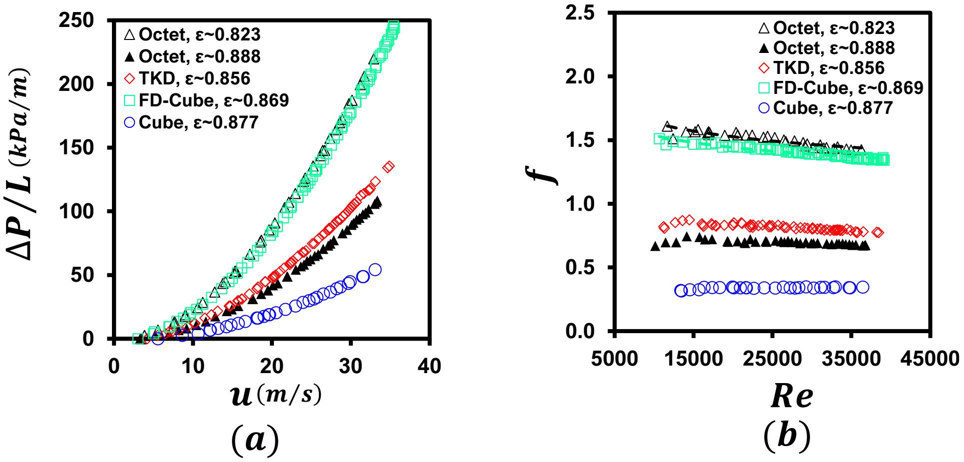

Figure 5.11 (a) Pressure gradient vs mean flow velocity, and (b) friction factor vs Reynolds number

Figure 5.11b shows the friction factor as a function of the Reynolds number. The friction factor of all the topologies were almost constant over the investigated range of flow velocities showing negligible dependence on the Reynolds number. This trend is typical of lattice configurations for fully turbulent fluid flows [38]. The mean friction factor value for Octet (0.888), TKD, FD-cube, and Cube was 0.696, 0.814, 1.402, and 0.339, respectively.

Figure 5.12 shows the friction factor augmentation for each topology with respect to the smooth channel data predicted by Blasius' equation ($f_0 = 0.079Re^{-0.25}$) for fully developed turbulent flows. The augmentation in flow losses provided by FD-cube was 208 to 238 times of the smooth channel configuration. The hydraulic performance was followed by TKD which provided about 118 to 138 times augmentation in the flow losses. Octet (0.888) provided the friction factor enhancement of 100 to 120 times. Cube provided the least friction factor enhancement of 39 to 60 times over the smooth channel.

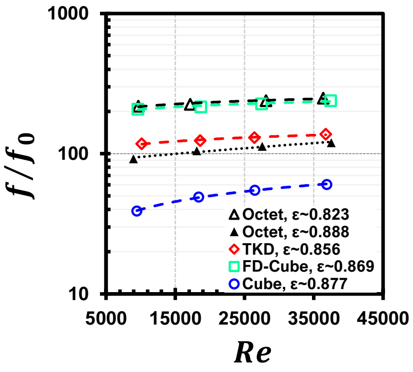

Figure 5.12 Friction factor augmentation vs Reynolds number

5.5.5 Heat transfer coefficient vs pumping power

Pumping power is an important metric from a cooling designer point of view, and in enhanced heat transfer studies it is recommended to evaluate heat transfer coefficient at the cost of pumping power (Fig. 5.13). For both-wall heating configuration, Octet (0.823) provided the highest heat transfer coefficient for the investigated pumping power range. Amongst the samples with similar porosity values, Cube yielded the highest heat transfer coefficient at any given pumping power. The Octet (0.888), TKD, and FD-cube provided very similar heat transfer coefficient values at a fixed pumping power condition. The trends were similar for the single wall heating configuration. The only difference was observed in the values of Octet (0.823) which were found to be closer to the Cube topology.

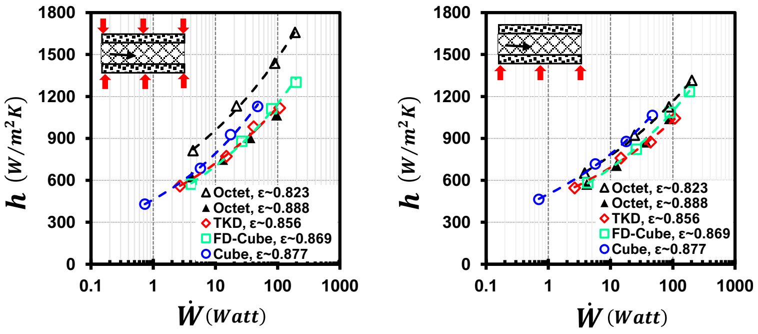

(*a*) (*b*)

Figure 5.13 Heat transfer coefficient vs pumping power requirements with heating on (a) both the walls, and (b) single wall

5.5.6 Thermal-hydraulic performance

The heat transfer augmentation in the trailing edge cooling channels is desirable at the minimal flow losses. The gain in thermal performance with respect to the increase in flow losses is generally quantified by the thermal-hydraulic performance (THP) parameter defined as:

$$THP = \frac{Nu/Nu_0}{(f/f_0)^{1/3}} \tag{5.6}$$

The THP values of all the topologies with respect to channel Reynolds number for both types of heating configurations are presented in Fig. 5.14. Although FD-cube was the most promising lattice when only heat transfer augmentation was considered, the overall THP of this structure was the weakest due to associated high flow losses. Octet (0.888) had slightly higher THP with respect to FD-cube at lower Reynolds number values, but the values approached that of the FD-cube for the higher investigated Reynolds number. At higher Reynolds number range, TKD also demonstrated similar performance to the Octet (0.888) and FD-cube for both types of heating conditions. Since Octet (0.888), TKD, and FD-cube exhibited similar THP levels, employment of

FD-cube in practical applications is recommended over the other two structures because it would yield high heat transfer values without compromising the overall thermal-hydraulic performance. However, Cube emerged as the best solution to obtain the high overall thermal performance which outperformed every other lattice topology for the investigated range of Reynolds number. The THP values provided by Cube topology were in the range of 2.12 to 2.78 and 1.9 to 2.53 for both-wall heating and single-wall heating conditions, respectively.

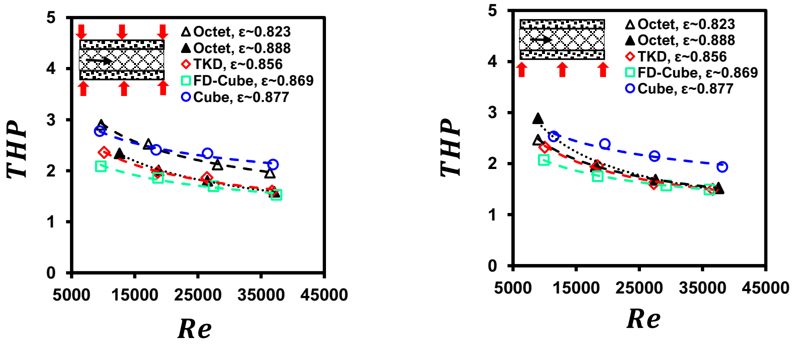

(a)

(b)

Figure 5.14 Thermal-hydraulic performance with respect to Reynolds number with heating on (a) both the walls, and (b) single wall considering fully developed flow conditions

Figure 15 shows the THP$_s$ of the investigated lattices where the heat transfer augmentation with respect to developing flows is considered such that:

$$THP_s = \frac{Nu/Nu_s}{(f/f_s)^{1/3}} = \frac{Nu/Nu_s}{(f/f_0)^{1/3}} \tag{5.7}$$

The simulations conducted over domain exactly similar flow domain to obtain Nu_s demonstrated no significant deviation in the friction factor from the values of standard Blasius' equation. The flow losses used in Eq. 5.7 were similar to those considered in Eq. 5.6. The THP$_s$ values in Fig. 5.15 were lower than THP provided in Fig. 5.14, which is expected due to reduced augmentation levels while the friction factor enhancement over smooth channel due to nearly hydrodynamically developed flow conditions was similar. Note that the Cube topology-based lattice configuration is similar to that of inline cylindrical pins arranged at uniform spacing in both streamwise and spanwise directions. Half fiber was added on the top and bottom wall in this study's Cubic configuration. It is worth pointing out that although Octet or FD-Cube topologies can yield in high cooling rates, the simplest Cubic configuration will still have the highest thermal hydraulic performance. Further, the added cost of AM to realize complex structures is another metric by which Cubic topology is more attractive as one is not limited to AM technologies to realize orthogonal pins, and that conventional manufacturing techniques can still be a viable choice for advanced heat exchanger development. However, if pumping power is constraint (Fig. 5.13), then lattices other than Cube such as Octet can be more attractive choice for enhanced mechanical load bearing capability as the thermal performance of all the investigated topologies was of similar level.

Figure 5.16 shows the comparison of THP_s obtained in the present study with that of the pin-fin and lattice configurations from prior publications. The values of the current study are presented in black markers. Nuntakulamarat et al. [39] investigated circular copper pin fins with height-to-diameter (H/D) ratio of 2.4, streamwise spacing (X/D) of 2, and spanwise spacing (S/D) of 4. Rao et al. [40] investigated stainless steel pin-fins having H/D = 1.0, X/D = S/D = 2.5. The lattices in the current investigation provide competing THP_s with respect to popular pin-fin configurations while yielding 5-10 times higher heat transfer augmentation with respect to smooth channel. The plot also shows data from Parbat et al. [13] who investigated additively manufactured Kagome lattice having unit cell height of 2.54 mm and streamwise length of 38.1 mm for turbine blade cooling applications. The THP_s of the current lattices provided better overall performance than Kagome lattice. Octet with porosities between 0.80 – 0.85 can prove to be very beneficial from thermo-mechanical point of view for turbine-blade cooling configurations. Octet with porosity 0.823 can be considered the most promising choice for obtaining the required thermo-mechanical properties amongst all the investigated topologies.

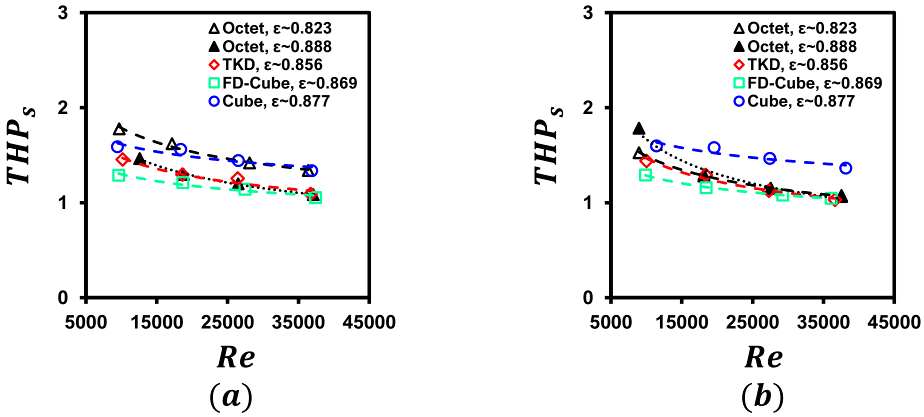

Figure 5.15 Thermal-hydraulic performance with respect to Reynolds number with heating on (a) both the walls, and (b) single wall considering developing flow conditions

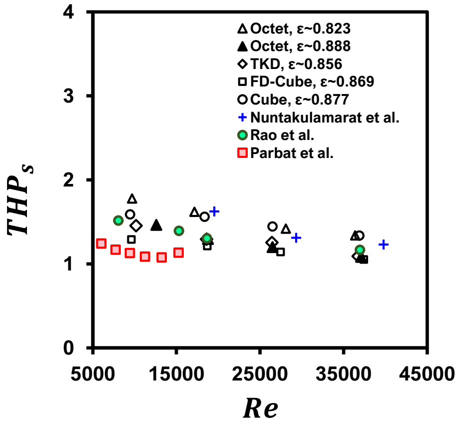

Figure 5.16 Comparison of THP$_s$ of the investigated samples with prior publications. Nuntakulamarat et al. [39], Rao et al. [40], Parbat et al. [13]

5.6 Conclusions

Experimental investigation was performed on sandwich-type single-cell thick lattices of four different unit cell topologies, viz. (a) Octet, (b) TKD, (c) FD-cube, and (d) Cube having intended design porosity of 0.886 and unit cell size of 10 mm built through Binder Jetting technology in 420 Stainless Steel infiltrated with Bronze. The thermal-hydraulic performances of these lattices were reported for a wide range of engine-representative Reynolds numbers. The thermal performance of these lattices was tested under two different heating condition: (a) when both the upper and bottom walls were heated, and (b) only bottom wall was heated, over a wide range of mass flow rates. The in-house porosity measurements showed significant deviations from the intended design, especially for Octet topology, which had to be considered to interpret the relative performance characteristics of these topologies. A trial-and-error process was followed to obtain the porosity of Octet sample closer to the remaining three topologies to allow direct comparison of their heat transfer and flow performances. The CT-scan images of the fabricated samples revealed significant roughness on the surfaces of endwalls and fibers along with zones of missing solid material on the fibers. The computations validated with in-house experiments showed that the effective thermal conductivity of the investigated samples was independent of considered topologies.

The relative trends of heat transfer coefficient, pressure gradient, Nusselt number and friction factor enhancement over the smooth channel, pumping power requirements and overall thermal-hydraulic performance were compared for the manufactured lattices having fair agreement of the porosity values. For thermal exchange, FD-cube yielded in the highest heat transfer performance, however at a larger pressure drop. Heat transfer performance of revised Octet, TKD, and Cube were comparable, especially at the higher Reynolds numbers. However, pressure gradient yielded by Octet was the second highest after FD-cube, followed by TKD and Cube, respectively. Due to significantly lower pressure drop values, the simplest topology of Cube topology had the highest heat transfer performance at any given pumping power condition. It also exhibited the highest overall thermal-hydraulic performance value of 2.78 at the lowest representative Reynolds number for both-wall heating configuration.

NOMENCLATURE

A_c	cross-section area of the duct
c_p	specific heat capacity
CT	computed tomography
D	pin-diameter
d_h	channel hydraulic diameter
f	friction factor ($\Delta P d_h / 2L\rho u^2$)
f_0	friction factor from Blasius equation ($f_0 = 0.079Re^{-0.25}$)
FCC	Face-centered cube
H	pin height
h	heat transfer coefficient
I	current flowing through the circuit
k_{eff}	effective thermal conductivity
k_f	fluid thermal conductivity
k_s	solid material thermal conductivity
L	streamwise length of the lattice
$\dot{m}$	mass flow rate
Nu	Nusselt number based on the channel hydraulic diameter (hd_h/k_f)
Nu_0	Nusselt number from Dittus-Boelter correlation in smooth channels ($Nu_0 = 0.023Re^{0.8}Pr^{0.4}$)
Nu_s	Nusselt number for thermally developing flows in smooth channels
Pr	Prandtl number
ΔP	pressure drop
$Q_{l,ins}$	loss through insulation
$Q_{net,C.V.}$	net heat input to the lattice excluding the losses
R_{htr}	resistance of the heater
Re	Reynolds number ($\rho u d_h/\mu$)
SLA	stereolithography
S/D	spanwise pitch

THP	thermal-hydraulic performance with respect to thermally developed flows
$\mathrm{THP_s}$	thermal-hydraulic performance with respect to thermally developing flows
TLC	Transient liquid crystal
$T_{b,L}$	bulk temperature at the exit
$T_{b,x}$	local bulk temperature
T_{in}	inlet temperature
T_{ref}	reference temperature
$\tilde{T}_w$	average wall temperature
ΔT	temperature difference across the insulation
u	mean flow velocity
X/D	streamwise pitch

Greek symbols

ρ	density of the fluid
μ	dynamic viscosity
ε	porosity

REFERENCES

[1] J.C. Han, A.P. Rallabandi, Turbine Blade Film Cooling Using PSP Technique, Frontiers in Heat and Mass Transfer. 1 (2010). https://doi.org/10.5098/hmt.v1.1.3001.

[2] P.M. Ligrani, M.M. Oliveira, T. Blaskovich, Comparison of heat transfer augmentation techniques, AIAA Journal. (2003). https://doi.org/10.2514/2.1964.

[3] R.S. Bunker, Innovative gas turbine cooling techniques, in: 2008: pp. 199–229. https://doi.org/10.2495/978-1-84564-062-0/07.

[4] K. Saha, S. Acharya, C. Nakamata, Heat Transfer Enhancement and Thermal Performance of Lattice Structures for Internal Cooling of Airfoil Trailing Edges, Journal of Thermal Science and Engineering Applications. (2013). https://doi.org/10.1115/1.4007277.

[5] S. Acharya, F. Zhou, J. Lagrone, G. Mahmood, R.S. Bunker, Latticework (Vortex) cooling effectiveness: Rotating channel experiments, Journal of Turbomachinery. 127 (2005) 471–478. https://doi.org/10.1115/1.1860381.

[6] I.T. Oh, K.M. Kim, D.H. Lee, J.S. Park, H.H. Cho, Local heat/mass transfer and friction loss measurement in a rotating matrix cooling channel, in: Proceedings of the ASME Turbo Expo, 2009: pp. 773–782. https://doi.org/10.1115/GT2009-59873.

[7] T. Tsuru, K. Ishida, J. Fujita, K. Takeishi, Three-dimensional visualization of flow characteristics using a magnetic resonance imaging in a lattice cooling channel, Journal of Turbomachinery. 141 (2019). https://doi.org/10.1115/1.4041908.

[8] S. Bu, L. Yang, H. Qiu, Y. Luan, H. Sun, Effect of sidewall slots and pin fins on the performance of latticework cooling channel for turbine blades, Applied Thermal Engineering. 117 (2017) 275–288. https://doi.org/10.1016/j.applthermaleng.2017.01.110.

[9] W. Du, L. Luo, S. Wang, J. Liu, B. Sunden, Heat transfer and flow structure in a detached latticework duct, Applied Thermal Engineering. 155 (2019) 24–39. https://doi.org/10.1016/j.applthermaleng.2019.03.148.

[10] J. Luo, Y. Rao, L. Yang, M. Yang, H. Su, Computational analysis of turbulent flow and heat transfer in latticework cooling structures under various flow configurations, International Journal of Thermal Sciences. 164 (2021). https://doi.org/10.1016/j.ijthermalsci.2021.106912.

[11] C. Carcasci, B. Facchini, M. Pievaroli, L. Tarchi, A. Ceccherini, L. Innocenti, Heat transfer and pressure loss measurements of matrix cooling geometries for gas turbine airfoils, in: Proceedings of the ASME Turbo Expo, 2014. https://doi.org/10.1115/GT2014-25384.

[12] B. Shen, Y. Li, H. Yan, S.K.S. Boetcher, G. Xie, Heat transfer enhancement of wedge-shaped channels by replacing pin fins with Kagome lattice structures, International Journal of Heat and Mass Transfer. 141 (2019) 88–101. https://doi.org/10.1016/j.ijheatmasstransfer.2019.06.059.

[13] S. Parbat, Z. Min, L. Yang, M. Chyu, Experimental and numerical analysis of additively manufactured inconel 718 coupons with lattice structure, Journal of Turbomachinery. (2020). https://doi.org/10.1115/1.4046527.

[14] A. Chaudhari, P. Ekade, S. Krishnan, Experimental investigation of heat transfer and fluid flow in octet-truss lattice geometry, International Journal of Thermal Sciences. (2019). https://doi.org/10.1016/j.ijthermalsci.2019.05.003.

[15] D. Liang, W. Bai, W. Chen, M.K. Chyu, Investigating the effect of element shape of the face-centered cubic lattice structure on the flow and endwall heat transfer characteristics in a rectangular channel, International Journal of Heat and Mass Transfer. (2020). https://doi.org/10.1016/j.ijheatmasstransfer.2020.119579.

[16] J. Broughton, Y.K. Joshi, Comparison of single-phase convection in additive manufactured versus traditional metal foams, Journal of Heat Transfer. (2020). https://doi.org/10.1115/1.4046972Y.

[17] J.Y. Ho, K.C. Leong, T.N. Wong, Additively-manufactured metallic porous lattice heat exchangers for air-side heat transfer enhancement, International Journal of Heat and Mass Transfer. (2020). https://doi.org/10.1016/j.ijheatmasstransfer.2019.119262.

[18] K.K. Wong, K.C. Leong, Saturated pool boiling enhancement using porous lattice structures produced by Selective Laser Melting, International Journal of Heat and Mass Transfer. (2018). https://doi.org/10.1016/j.ijheatmasstransfer.2017.12.148.

[19] H. Montazerian, M. Zhianmanesh, E. Davoodi, A.S. Milani, M. Hoorfar, Longitudinal and radial permeability analysis of additively manufactured porous scaffolds: Effect of pore shape and porosity, Materials and Design. (2017). https://doi.org/10.1016/j.matdes.2017.03.006.

[20] Y. Du, H. Liang, D. Xie, N. Mao, J. Zhao, Z. Tian, C. Wang, L. Shen, Finite element analysis of mechanical behavior, permeability of irregular porous scaffolds and lattice-based porous scaffolds, Materials Research Express. 6 (2019). https://doi.org/10.1088/2053-1591/ab3ac1.

[21] A. Timercan, V. Sheremetyev, V. Brailovski, Mechanical properties and fluid permeability of gyroid and diamond lattice structures for intervertebral devices: functional requirements and comparative analysis, Science and Technology of Advanced Materials. 22 (2021) 285–300. https://doi.org/10.1080/14686996.2021.1907222.

[22] D. Ali, S. Sen, Finite element analysis of mechanical behavior, permeability and fluid induced wall shear stress of high porosity scaffolds with gyroid and lattice-based architectures, Journal of the Mechanical Behavior of Biomedical Materials. (2017). https://doi.org/10.1016/j.jmbbm.2017.07.035.

[23] I. Kaur, P. Singh, Flow and Thermal Transport Through Unit Cell Topologies of Cubic and Octahedron Families, International Journal of Heat and Mass Transfer. 158 (2020). https://doi.org/10.1016/j.ijheatmasstransfer.2020.119784.

[24] M. Iasiello, S. Cunsolo, M. Oliviero, W.M. Harris, N. Bianco, W.K.S. Chiu, V. Naso, Numerical analysis of heat transfer and pressure drop in metal foams for different morphological models, Journal of Heat Transfer. (2014). https://doi.org/10.1115/1.4028113.

[25] I. Kaur, P. Singh, Numerical investigation on conjugate heat transfer in octet-shape-based single unit cell thick metal foam, International Communications in Heat and Mass Transfer. 121 (2021) 105090. https://doi.org/10.1016/j.icheatmasstransfer.2020.105090.

[26] I. Kaur, P. Singh, Endwall heat transfer characteristics of octahedron family lattice-frame materials, International Communications in Heat and Mass Transfer. 127 (2021) 105522. https://doi.org/10.1016/j.icheatmasstransfer.2021.105522.

[27] Y. Aider, I. Kaur, H. Cho, P. Singh, Periodic heat transfer characteristics of additively manufactured lattices, International Journal of Heat and Mass Transfer. 189 (2022) 122692. https://doi.org/10.1016/j.ijheatmasstransfer.2022.122692.

[28] I. Kaur, P. Singh, Direct Pore-Scale Simulations of Fully Periodic Unit Cells of Different Regular Lattices, Journal of Heat Transfer. 144 (2022) 022702. https://doi.org/10.1115/1.4053204.

[29] I. Kaur, P. Singh, State-of-the-art in heat exchanger additive manufacturing, International Journal of Heat and Mass Transfer. 178 (2021) 121600. https://doi.org/10.1016/j.ijheatmasstransfer.2021.121600.

[30] C.K. Stimpson, J.C. Snyder, K.A. Thole, D. Mongillo, Effectiveness measurements of additively manufactured film cooling holes, Journal of Turbomachinery. (2018). https://doi.org/10.1115/1.4038182.

[31] C.K. Stimpson, J.C. Snyder, K.A. Thole, D. Mongillo, Effects of coolant feed direction on additively manufactured film cooling holes, Journal of Turbomachinery. (2018). https://doi.org/10.1115/1.4041374.

[32] J.C. Snyder, C.K. Stimpson, K.A. Thole, D. Mongillo, Build direction effects on additively manufactured channels, Journal of Turbomachinery. 138 (2016) 1–8. https://doi.org/10.1115/1.4032168.

[33] K.L. Kirsch, K.A. Thole, Pressure loss and heat transfer performance for additively and conventionally manufactured pin fin arrays, International Journal of Heat and Mass Transfer. 108 (2017) 2502–2513. https://doi.org/10.1016/j.ijheatmasstransfer.2017.01.095.

[34] N. Wang, I. Kaur, P. Singh, L. Li, Prediction of effective thermal conductivity of porous lattice structures and validation with additively manufactured metal foams, Applied Thermal Engineering. 187 (2021) 116558. https://doi.org/10.1016/j.applthermaleng.2021.116558.

[35] R.J. Moffat, Describing the uncertainties in experimental results, Experimental Thermal and Fluid Science. 1 (1988) 3–17. https://doi.org/10.1016/0894-1777(88)90043-X.

[36] J.W. Paek, B.H. Kang, S.Y. Kim, J.M. Hyun, Effective Thermal Conductivity and Permeability of Aluminum Foam Materials1, International Journal of Thermophysics. 21 (2000) 453–464. https://doi.org/10.1023/A:1006643815323.

[37] P. Ekade, S. Krishnan, Fluid flow and heat transfer characteristics of octet truss lattice geometry, International Journal of Thermal Sciences. 137 (2019) 253–261. https://doi.org/10.1016/j.ijthermalsci.2018.11.031.

[38] H. Yan, X. Yang, T. Lu, G. Xie, Convective heat transfer in a lightweight multifunctional sandwich panel with X-type metallic lattice core, Applied Thermal Engineering. (2017). https://doi.org/10.1016/j.applthermaleng.2017.08.081.

[39] M. Nuntakulamarat, C.-C. Shiau, J.-C. Han, Heat Transfer and Pressure Drop Measurements in a High Aspect Ratio Channel With Circular Pins and Strip Fins, Journal of Thermal Science and Engineering Applications. 12 (2020) 031019. https://doi.org/10.1115/1.4045221.

[40] Y. Rao, C. Wan, S. Zang, An Experimental and Numerical Study of Flow and Heat Transfer in Channels With Pin Fin-Dimple Combined Arrays of Different Configurations, Journal of Heat Transfer. 134 (2012) 121901. https://doi.org/10.1115/1.4006943.

CHAPTER VI

MODELING ROUGHNESS EFFECTS FOR ACCURATE THERMAL PERFORMANCE PREDICTIONS

Roughness is inherently manifested on the surface walls of the lattices printed through metal additive manufacturing technologies. Several other defects such as absence of solid material locally resulting in appreciable voids in the fiber volume and irregularities in the fiber shapes can significantly impact the thermal performance of the lattices. The impact of the roughness can become severe when their sizes are large enough to interrupt the boundary layers near the walls. Roughness in lattices can have profound impact on thermal exchange in multiphase configurations such as boiling where the extended roughness features serve as nucleation sites. The numerical analysis conducted on the smooth CAD models typically tend to underpredict the thermal performance of the additively manufactured lattices as these models fail to capture the impacts of roughness features. Incorporation of roughness in computational modeling of lattices is almost non-existent in the literature because of the following concerns:

1. Roughness induced on lattices during additive manufacturing is random in nature. It depends on the process parameters, build orientation, metal material, powder-size, post processing methods, and dimensional scales of the samples. Thus the roughness signatures on the surfaces can be unique to any part depending on these parameters. Accurate and

universal prediction of roughness for a combination of these several parameters is still not available.

2. CT-scan images can be used to generate the computational domains that closely mimic the real surfaces. However, extremely fine voxel sizes are required to accurately capture the small-scale roughness features that increase the memory requirements for processing the files and making them suitable for being fed into the flow solvers.
3. The investigations rarely focus on understanding the fundamental ways in which roughness can affect heat transfer in the lattices at micro-level and solution over smooth CAD can provide time-saving analysis of the general flow and thermal exchange phenomenon. However, the predictions can be severely deviated from reality as the unit cell sizes become increasingly small (typically < 5 mm).

Since CT-scan approach can be cost- and time-intensive, alternative approaches to generate artificial random roughness having same statistical parameters as that on the manufactured surface can be generated. This approach is used in modeling the rough surfaces in the present study.

6.1 Geometrical details:

Figure 6.1 shows the three geometries generated in the current study for the analysis of roughness effects on the heat transfer. Single cell thick Tetrakaidecahedron lattice discussed in Fig. 5.2 of Chapter 5 was used for the current numerical study. Geometry A had smooth fibers and endwalls with porosity value of 0.886 which is the intended CAD model design used for printing. The roughness on fibers and endwall can have different interactions with the flow and therefore impart different influence on the heat transfer. In order to understand how each of these affect the

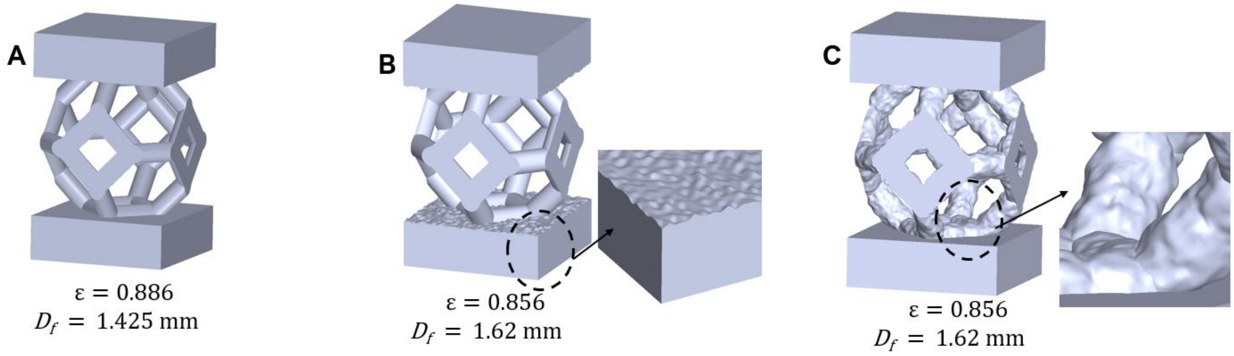

Figure 6.1 Geometries generated for roughness effect analysis: (A) smooth fiber + smooth endwall, (B) smooth fiber + rough endwall, and (C) rough fiber + smooth endwall

final thermal performance, the roughness study was divided into two parts, one is Geometry B which had the smooth fibers and rough endwalls, and the other is Geometry C which had rough fibers and smooth endwalls. Since the aim was to incorporate roughness and other structural anomalies in the computational model, Geometry B and C had the final lattice porosity of 0.856, which was similar to the measured porosity of the samples. The fiber diameter of the smooth CAD model was 1.425 mm, whereas it was 1.62 mm for 0.856 porosity at unit cell size (s) of 10 mm.

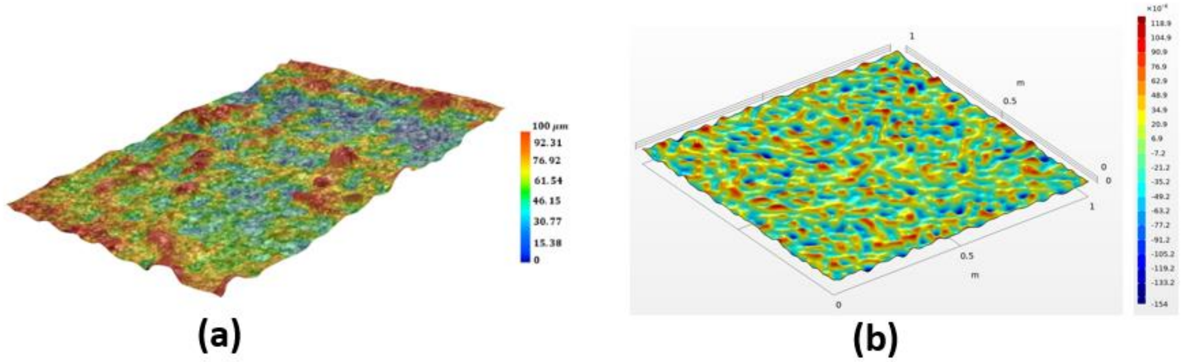

Figure 6.2 (a) Roughness of the sample measured through profilometer, and (b) roughness profile generated in COMSOL Multiphysics® (units in m - later scaled in CAD software)

Figure 6.2 shows the roughness as measured on the inner surface of the endwall of Tetrakaidecahedron lattice. The mean surface roughness (S_a) was measured to be around 25.94 µm. Surface having similar mean roughness was generated in commercial software COMSOL Multiphysics®, as shown in Fig. 6.2b, using parametric equations. Figure 6.3a shows the rough cylindrical surface generated in COMSOL Multiphysics® which was then converted into solid body in CAD software and then appropriately scaled to obtain final Tetrakaidecahedron lattice of porosity 0.856.

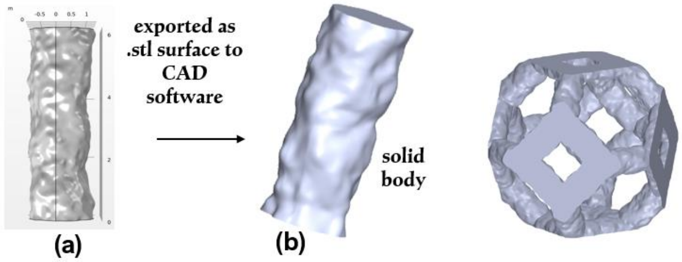

Figure 6.3 (a) Rough fiber generated in COMSOL Multiphysics®, and (b) corresponding solid body obtained in CAD software

Figure 6.4 shows the computational domain which included a single array of five unit cells in streamwise direction. The lateral planes were considered symmetry and heat flux was provided at the top and bottom endwalls. Extended inlet (76 mm) and outlet (50 mm) was provided to ensure fully developed flow and avoid reverse flow effects, respectively. The simulation was conducted at the channel Reynolds number of ~9,806 with channel inlet fluid velocity of 9.21 m/s.

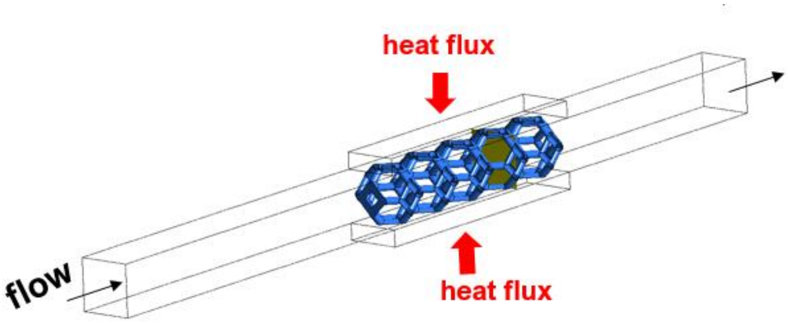

Figure 6.4 Computational domain

6.2 Results and discussion

Figure 6.5 shows the velocity contours on planes at the middle of the fourth unit-cell array (highlighted in Fig. 6.4). Higher velocity values were found in both Geometry B and C, which had higher fiber diameter than Geometry A. Larger fiber diameter decreased the flow area resulting in higher local velocities by virtue of mass continuity. The Geometry C with rough fibers had slightly higher enhancement than Geometry B.

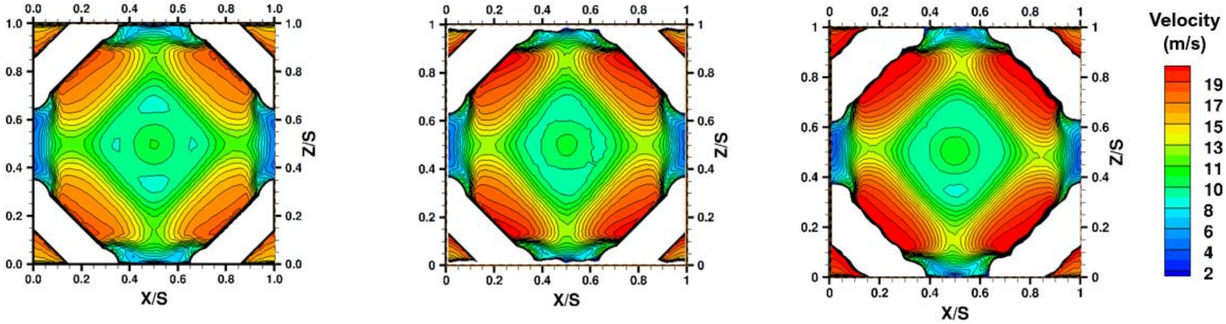

Figure 6.5 Velocity contours at the middle of the fourth unit-cell array: from left to right – Geometry A, Geometry B, and Geometry C

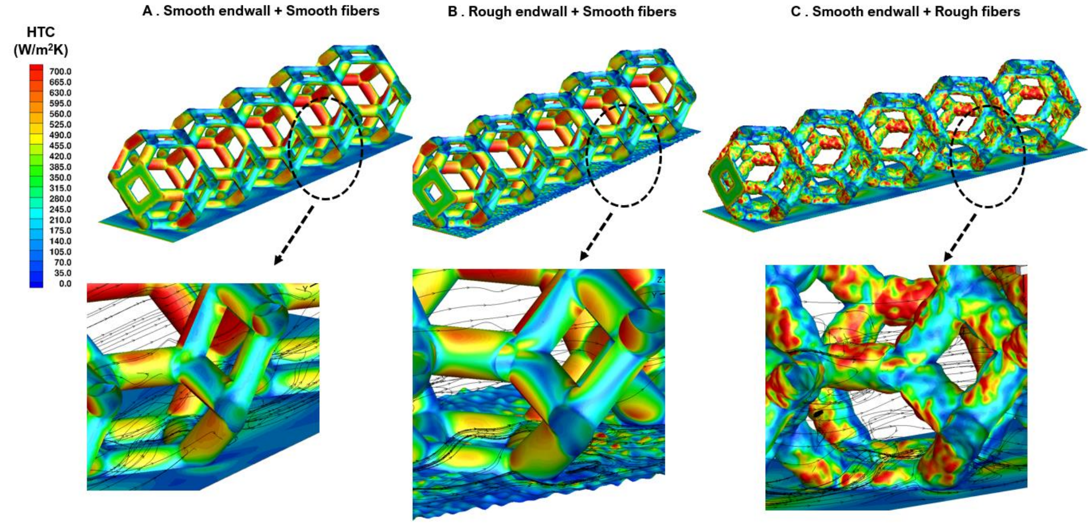

Figure 6.6 Interfacial heat transfer coefficient plotted on the fibers and endwalls of the three investigated structures: from left to right – Geometry A, Geometry B, and Geometry C

Figure 6.6 shows the heat transfer coefficient contours on the fibers and the endwalls. The profiles on the fibers of smooth CAD model of Geometry A and B were uniform in the areas of direct flow impingement whereas a very *‘smeared’* type non-uniform distribution was present on rough fibers of Geometry C. The streamlines directly hitting the protruding local roughness areas generated higher interfacial heat transfer coefficient values than adjacent low-lying areas in Geometry C. The streamlines smoothly glided through smooth endwalls and fibers of Geometry A. The interfacial heat transfer coefficient on the endwalls were locally enhanced on the roughness peaks downstream of the fibers of Geometry B. In Geometry B, the flow was re-distributed and spread by the roughness features on the endwall.

The overall conjugate heat transfer coefficient of Geometry A was ~26% lower than the experimental data reported in Chapter 5. Geometry B provided about ~18.89 % under-prediction of data, whereas Geometry C provided ~ 14% lower prediction of the heat transfer coefficient. The analysis of this study shows that roughness on endwalls and fibers are crucial in determining heat transfer performance and their incorporation in the computational domains can significantly improve the numerical predictions. Moreover, roughness analysis helps us understand the actual flow and thermal exchange process in additively manufactured surfaces.

CHAPTER VII

CONCLUSIONS AND RECOMMENDATIONS FOR FUTURE WORK

Lattices made through an orderly arrangement of unit cells having user-defined architecture are an effective medium to manage thermal as well as mechanical stresses in critical engineering applications. The prospects of their utilization in cooling avionics components, enhancing thermal performance of heat-pipes, improving thermal storage devices, and increasing peak mechanical load bearing capability is very high. Although there is a continuous pursuit to understand the performance of various types of lattice topologies and configurations both quantitatively and qualitatively, there exists significant gap in the literature which the current investigation aims to fill. Following are the key issues of lattice performance that were addressed in the present study along with the major conclusions:

1. ***Establishing the candidacy of lattices as thermal management concept*** - The current lattice literature consists of large number of lattice topologies, most of them which have been investigated only numerically in the past for their thermal performance. A thorough comparison of the thermal-hydraulic performance of different topologies when subjected to similar flow conditions to establish the superiority of one over the others is missing but important. Therefore, four unit cells, viz. (a) Octet, (b) Face-diagonal (FD) cube, (c) Tetrakaidecahedron, and (d) Cube, were chosen for thorough analysis based on the literature review.

2. ***Interfacial heat transfer coefficient in block-type configuration*** – After choosing the suitable configurations, the interfacial heat transfer coefficient was numerically determined through non-conjugate simulations on single-cell thick configuration in streamwise direction and periodic in the other two. Octet provided the highest interfacial heat transfer coefficient as well pressure drop. Cube lattice exhibited the lowest heat transfer coefficient as well as pressure drop.
3. ***Heat transfer in single-cell thick configuration*** – Octet demonstrated the best non-conjugate performance in block configuration and was therefore subjected to numerical analysis further to determine the conjugate as well as interfacial heat transfer coefficient in single-cell thick configuration at high porosity with water as the working fluid. Octet provided better thermal performance in comparison to prior published data on stochastic metal foam as well as rhombic dodecahedron lattice under similar flow conditions. The interfacial heat transfer coefficient on the fibers was higher than that on the endwall. The flow interaction with the endwall play an important role alongside the conjugate thermal exchange in the core volume of single cell thick lattices.
4. ***Manufacturing the lattices*** - After conducting numerical analysis and establishing their candidacy for improving thermal exchange on actively heated substrates, the parts were printed in 420 Stainless Steel via *Binder Jetting*. The selected topologies represented varied fiber complexity and manufacturing challenges. The manufacturing imposed serious limitations on the achievable designed porosity and unit-cell sizes, which were 0.886 (lower than simulated values) and 10 mm, respectively. The parts with endwalls were difficult to be realized through Laser-Powder Bed Fusion (LPBF) technologies in high thermal conductivity materials such as Aluminum due to inconvenience in removing the

internal support structures. At present, realization of lattices with smaller dimensional scales at higher porosity (> 0.90) in high conductivity materials at affordable prices is very challenging.

5. ***Forced convection experiments*** – Extensive experimental tests were conducted on coupons printed in single-cell thick configurations. The parts demonstrated dimensional inaccuracies and porosity deviations with respect to the designed CAD models. The X-ray CT scan images showed significant roughness incurred on the fibers and endwalls of the coupons. Steady-state experiments were performed to determine the effective thermal conductivity of the samples. All the topologies having similar porosity demonstrated similar values showing that effective thermal conductivity was independent of the topology, however, variations in porosity for the same topology can result in varied effective thermal conductivity. Overall conjugate heat transfer and pressure drop was the highest for the FD-Cube amongst all four topologies at similar porosity. The thermal-hydraulic performance was the highest for simple Cube lattice. It can be concluded that configuration demonstrating the highest interfacial heat transfer coefficient might not provide the best performance under conjugate scenarios. Moreover, the relative lattice performance can tend to vary under different physical configurations (e.g. block-type and single-cell sandwich type).
6. ***Roughness effects in computational modeling*** – Preliminary numerical tests were conducted on smooth CAD models, however, the CT-scan images of the actual printed samples showed significant roughness on the surface walls. Therefore, a methodology to incorporate those roughness effects in computational models was later explained to accurately predict the heat transfer in computational models. The numerical analysis on

rough geometries showed that the roughness and dimensional inaccuracies modeled in simulated domains can significantly improve the thermal predictions.

There is continuous effort to improve the current metal additive manufacturing technologies to realize lattices with dimensional accuracy and superior surface quality. Following key aspects still need attention for a comprehensive understanding of the flow and thermal performance of the additively manufactured lattices:

1. ***Implications of the manufacturing process*** – It is apparent that additive manufacturing technology will be the most sought after tool to print the unique architectured materials in the future. The performance of the lattices is closely knitted with the quality of the product produced by the additive manufacturing process, especially at the scales relevant to actual electronics cooling applications. In such a scenario, one cannot neglect the surface characteristics in quantitative determination of the heat transfer performance. The scalability of results for lattices printed in same material but different additive manufacturing processes rendering different surface characteristics at smaller fiber and unit cell sizes needs further investigation.
2. ***Selection of lattices for multifunctional applications*** **–** Lattices were primarily employed in mechanical load-bearing operations but later gained attention for heat transfer augmentation applications. Therefore, these lattices can be employed for multifunctional purposes where both the mechanical and thermal load-bearing capabilities are required. The coupled thermo-mechanical analysis needs to be conducted on the lattices studied herein to determine their mechanical performance in high operating temperature

environment. A lattice demonstrating the best mechanical properties might not provide the best thermal-performance.

3. ***Roughness and computational model*** – Roughness is one of the key aspects of surface quality of products fabricated through additive manufacturing and its randomness has made its replication in computational procedures very challenging. Routes such as utilization of CT-scans to obtain computational domains can be followed, but it requires large hardware memory to clean and pre-process the files before feeding them into flow solvers. Alternate methodologies to generate roughness profiles having same statistics as that of the fabricated sample need to be developed. Several investigations have reported procedures to mimic the real roughness patterns to a fair accuracy, however, most of these effects were generated on the walls of plane channels. The roughness generation in entire lattice sample to mimic the patterns of actual printed samples, both on endwall and fibers, still need further investigation.